Fakultät für Chemie
der Technischen Universität München

Max-Planck-Institut für Biochemie
Abteilung für Molekulare Strukturbiologie

Elucidation of the Molecular Mechanisms Underlying Substrate Processing by the 26S Proteasome

Markus Rainer Eisele

Vollständiger Abdruck der von der Fakultät für Chemie der Technischen Universität München zur Erlangung des akademischen Grades eines Doktors der Naturwissenschaften (Dr. rer. nat.) genehmigten Dissertation.

Vorsitzende
Prof. Dr. Sevil Weinkauf

Prüfer der Dissertation
1. Hon.-Prof. Dr. Wolfgang Baumeister
2. Prof. Dr. Johannes Buchner

Die Dissertation wurde am 25.09.2018 an der Technischen Universität München eingereicht und durch die Fakultät für Chemie am 31.01.2019 angenommen.

Summary

The 26S proteasome is a 2.5 MDa protein complex that orchestrates protein degradation in eukaryotic cells at the final stage of the ubiquitin proteasome system (UPS). In the UPS, a substrate is modified through the attachment of a polyubiquitin chain and is then recognized and degraded by the proteasome. Using single-particle cryo-electron microscopy, four major conformations of the 26S proteasome have been reported, which propose a model regarding the mechanism of substrate processing. However, the structural basis of the regulatory mechanisms of proteasome function, such as control of the core particle gate or substrate translocation by the AAA+ ATPase module, are not completely understood.

In this doctoral thesis, the conformational landscape coverage was further broadened for a deeper understanding of the 26S proteasome catalytic mechanism. A combination of three different biological approaches – provision of nucleotide analogs, directed point mutations in the AAA+ ATPase subunits or using a designed model substrate – resulted in the alteration of the conformational equilibria of the proteasome, and ultimately led to the identification of three different newly discovered proteasome states. The broadened coverage of the conformational landscape provides a deeper understanding of the 26S proteasome catalytic mechanism. A combination of high resolution structures and biochemical analysis elucidate the gate opening mechanism by docking of the C-termini of Rpt1 and Rpt6. Detailed analysis of the AAA+ ATPase revealed the formation of a Phe-cluster, which enabled me to distinguish configurations of the nucleotide binding pockets. By assignment of the nucleotide pockets of the proteasomal states as open, engaged or intermediate a reoccurring pattern could be found hypothesizing a sequential nucleotide-driven translocation. In summary, this deepened knowledge of proteasome conformational dynamics reveals the fundamental mechanisms of the regulation of gate opening and communication between the proteasome subunits.

Zusammenfassung

Das 26S Proteasome ist ein 2,5 großer MDa Proteinkomplex, der als Exekutive im Ubiquitin-Proteasom-System (UPS) zum Abbau von Proteinen in eukaryotischen Zellen verantwortlich ist. Im UPS wird ein Substrat über eine Enzymkaskade durch kovalente Verknüpfung mit dem Molekül Ubiquitin markiert und schließlich durch das 26S Proteasome erkannt und abgebaut. Mit Hilfe von Einzelpartikel-Kryo-Elektronenmikroskopie wurden in der Vergangenheit insgesamt vier Proteasomkonformationen aufgelöst, welche eine erste Hypothese zum Mechanismus der Substratprozessierung möglich machte, aber Interaktionen zwischen Untereinheiten, und damit beispielsweise verbunden den 20S Kernpartikel-Öffnungsmechanismus oder die Substrattranslokation durch das AAA+ ATPase Modul, nicht oder nur teilweise erklären konnten.

In dieser Doktorarbeit wurde die Erfassung des konformationellen Raums des 26S Proteasomes erweitert und daraus ein größeres Verständnis des katalytischen Zyklus gewonnen. Die Kombination dreier Methoden – der Einsatz von Nukleotidanalogen, direkte Punktmutationen im ATPase Modul und die Zugabe eines Modell-Substrats – wurde benutzt, um das 26S Proteasome in unterschiedliche Zustandsequilibria zu überführen. Dies führte letztendlich zu der Entdeckung von drei unbekannten Zuständen. Mit diesen Ergebnissen konnte die Komplexität des Zusammenspiels der Untereinheiten besser verstanden werden. Dazu gehört die Erklärung des Porenöffnungsmechanismus des 20S Kernpartikels mit Hilfe von hochaufgelösten Strukturen und biochemischen Analysen. In mehr Detail wurde gezeigt, dass das Docken der C-termini von Rpt1 und Rpt6 Schlüsselfunktionen im Wechsel von einem geschlossenen zu einer offenen Pore erfüllen. Die Analyse der Nukleotidtaschen der AAA+ ATPase führte zu der Entdeckung von wiederkehrenden Phenylalanin Gruppen, mit Hilfe dieser der Zustand von Nukleotidtaschen definiert werden konnte. Dadurch konnte eine wiederkehrende Abfolge von Nukleotidtaschen-Zuständen gefunden werden, die die Hypothese ermöglicht auf ein sequentiell Nukleotid-gesteuerte Substrattranslokation zu schließen. Zusammengefasst konnte mit Hilfe der zusätzlichen Zustandsequilibria ein genaueres Bild der hoch flexiblen 26S Proteasomzustandslandschaft gewonnen und damit der Porenöffnungsmechanismus und die Kommunikation zwischen Untereinheiten im ATPase-Zyklus besser verstanden werden.

Contents

Summary **III**

Zusammenfassung **IV**

Contents **V**

List of Figures **IX**

List of Tables **XI**

1 Introduction **1**

1.1 The Ubiquitin Proteasome System 1
  1.1.1 The Variety of Ubiquitin Chains 2
  1.1.2 Proteasomal Substrate 3
1.2 The 26S Proteasome 5
  1.2.1 The 20S Core Particle 5
  1.2.2 The Gate 6
  1.2.3 The 19S Regulatory Particle 7
    1.2.3.1 The Lid 8
    1.2.3.2 The Base 9
  1.2.4 The ATPase 10
  1.2.5 Structure and the Conformational States 11
1.3 3D Cryo-Electron Microscopy 14
  1.3.1 Transmission Electron Microscopes 14
  1.3.2 Sample Preparation for Cryo-Electron Microscopoy 16
1.4 Single-Particle Analysis 17
  1.4.1 3D Reconstruction in SPA 17
  1.4.2 Conformational Heterogeneity and 3D Classification 18
1.5 Objective and Aims 19

2 Materials and Methods **21**

2.1 Materials 21
  2.1.1 Chemicals and Consumables 21
  2.1.2 Buffers and Solutions 23

2.1.3 Cell Culture Media 24
2.1.4 Yeast Strains 25
2.1.5 Plasmids 27
2.1.6 Software 27
2.2 Methods 28
2.2.1 Molecular Cloning 28
2.2.1.1 Polymerase Chain Reaction (PCR) 28
2.2.1.2 Restriction Digestion 29
2.2.1.3 In-Fusion Cloning kit 29
2.2.1.4 Transformation of Competent Cells 29
2.2.1.5 Small-Scale Plasmid DNA Preparation 29
2.2.1.6 Photometric Measurement of DNA Concentration 29
2.2.1.7 DNA Sequence Analysis 30
2.2.2 Protein Purification 30
2.2.2.1 *E. coli* Cell Culture 30
2.2.2.2 DHFR Substrate Purification 30
2.2.2.3 Yeast Cell Culture 31
2.2.2.4 26S Proteasome Purification 31
2.2.3 Analytical Methods 32
2.2.3.1 Determination of Protein Concentration using Bradford . . . 32
2.2.3.2 Discontinuous SDS-Polyacrylamide Gel Electropheresis (SDS-PAGE) 32
2.2.3.3 Western Blotting 32
2.2.3.4 20S Proteasome Activity Assay 33
2.2.3.5 26S Proteasome Analytic Digest 33
2.2.4 Electron Microscopy 33
2.2.4.1 Sample Preparation 33
2.2.4.1.1 Negative Stain 33
2.2.4.1.2 Plunge Freezing 34
2.2.4.2 Data Acquisition 34
2.2.4.2.1 Negative Stain Data Acquisition 34
2.2.4.2.2 Cryo-EM Data Acquisition 34
2.2.4.3 Image Processing 34
2.2.4.4 Single particle analysis 34
2.2.4.5 Model-building and analysis 37

3 Results **39**
3.1 Biochemical preparation 39
3.1.1 Purification of the 26S Proteasome 39
3.1.2 Preparation of a Model Substrate of the 26S Proteasome 40

3.2 26S Proteasome in the Background of ATPγS 42
3.2.1 Analysis of the s5 State 43
3.3 26S Proteasome in the Background of ATPase Walker B EQ Mutants 46
3.3.1 Structural Analysis of the Walker B EQ Mutants 47
3.4 26S Proteasome in the Presence of a Model Substrate 49
3.5 The Gating of the 20S CP 52
3.5.1 The Analysis of the RP-CP Interface 52
3.5.2 The Analysis of the 20S α Ring 54
3.6 Analysis of the AAA+ ATPase 58
3.6.1 The Conserved Phe-Cluster 58

4 Conclusions and Discussion **63**
4.1 The Substrate Engaged Structure 63
4.2 Modification of the State Landscape 65
4.3 The Open Gate Mechanism 67
4.4 Sequential Nucleotide Driven Translocation 69

5 Future Perspectives **73**

A Abbreviations **75**

References **79**

Acknowledgments **91**

List of Figures

1.1 Schematic overview of the UPS system 2
1.2 Variation of ubiquitin chains 3
1.3 The 26S proteasome 5
1.4 Structure and function of the 20S core particle 6
1.5 The regulatory particle 8
1.6 The ATPase of the base subcomplex 11
1.7 The proteasome conformational state landscape 13
1.8 Schematic overview of an electron microscope 15
1.9 Projection-slice theorem 17

2.1 SPA workflow 36

3.1 Purification of 26S Proteasome 40
3.2 Design and purification of a model substrate 40
3.3 Model substrate assays 41
3.4 ATPγS concentration dependent 26S state landscape 42
3.5 Model substrate influences ATPγS purified 26S proteasomes 43
3.6 Cryo-EM reconstructions of the s3, s4 and s5 states 43
3.7 RMSD comparison of s5 with the other states 44
3.8 Subunit differences between s2 and s5 45
3.9 Generating Walker B EQ mutants 46
3.10 The Walker B EQ proteasome conformational state landscape 47
3.11 Cryo-EM density of the s6 state 47
3.12 RMSD comparison of s6 with the other states 48
3.13 Substrate and *o*PA dependent 26S proteasome state landscape 49
3.14 Cryo-EM density of the s7 state 50
3.15 RMSD comparison of s7 with the other states 50
3.16 Coaxial alignment comparison between s5 and s7 51
3.17 The interface between the RP and the CP 52
3.18 Sequence alignments of Rpt1 and Rpt6 C-termini 53
3.19 Mutagenesis analysis of the Rpt1 and Rpt6 C-termini 53
3.20 Sequence alignments of YD-P-Y motif of α subunits 54

3.21 Comparison of a closed and an open CP gate 55
3.22 Mutagenesis analysis of Phe7 in α2 56
3.23 Canoncial cluster between α6 and α7 56
3.24 N-terminal flipping and movement of α2 57
3.25 Nucleotide pocket loading in seven states 58
3.26 Distance of nucleotide pockets 59
3.27 Phe-clustering between nucleotide pockets 59
3.28 Overview of Phe-cluster and pocket distance 60
3.29 Hierarchical clustering of nucleotide binding pocket 61

4.1 Gate model 68
4.2 ATPcycle 71

List of Tables

2.1 Chemicals and consumables 21
2.2 Protein analysis buffers 23
2.3 Cell culture media. 24
2.4 Yeast strains 25
2.5 Plasmids 27
2.6 Software 27
2.7 PCR components 28
2.8 PCR program 28
2.9 SPA Overview 35

Chapter 1

Introduction

1.1 The Ubiquitin Proteasome System

Expression levels of proteins are determined by a balance between protein synthesis and protein degradation (Labbadia and Morimoto, 2015). Protein degradation prevents misfolded proteins and damaged proteins from causing cellular stress (Labbadia and Morimoto, 2015) but it is also necessary for protein signaling cascades, cell cycle regulation and for many other cellular pathways (Jung et al., 2009; Finley et al., 2012). Eukaryotes have two major protein degradation pathways to eliminate intracellular proteins: autophagy (Yang and Klionsky, 2010) and the ubiquitin proteasome system (UPS) (Finley et al., 2012). While there is a bulk-degradation of proteins during autophagy, a more selective degradation is achieved by the UPS. The UPS is responsible for the regulated degradation of proteins that reside in the nucleus and cytosol (Hershko and Ciechanover, 1998; Glickman and Ciechanover, 2002; Finley, 2009; Finley et al., 2012). The UPS fulfills a central role in the control of cellular processes such as the cell cycle, transcription, signal transduction, apoptosis and protein quality control. Hindering the UPS leads to protein aggregation and can in turn cause diseases such as Huntington's Disease (Glickman and Ciechanover, 2002) or Cystic Fibrosis (Bence et al., 2001).

The UPS specifically targets proteins for degradation through covalent modification by the 8.5 kDa protein ubiquitin. An enzymatic cascade of three enzymes, E1, E2 and E3, attaches ubiquitin to the target protein and elongates the ubiquitin chain (Fig. 1.1). First, the ubiquitin protein is activated and attached via a thioester bond in an ATP-dependent manner to the ubiquitin-activating enzyme (E1). In yeast there is only one E1 enzyme that catalyzes the first step, while in humans there are two different E1 enzymes known to date for initiating the conjugation of ubiquitin (McGrath et al., 1991; Schulman and Harper, 2009). The ubiquitin is then transferred to a ubiquitin-conjugating enzyme (E2), before being attached to the target lysine of the intended substrate through the help of ubiquitin ligases (E3) (Finley et al., 2012). While there are 11 E2 enzymes in yeast and 20-30 in human, the number of E3 enzymes is over several hundred to cope with the large variety of substrates to be ubiquitinated.

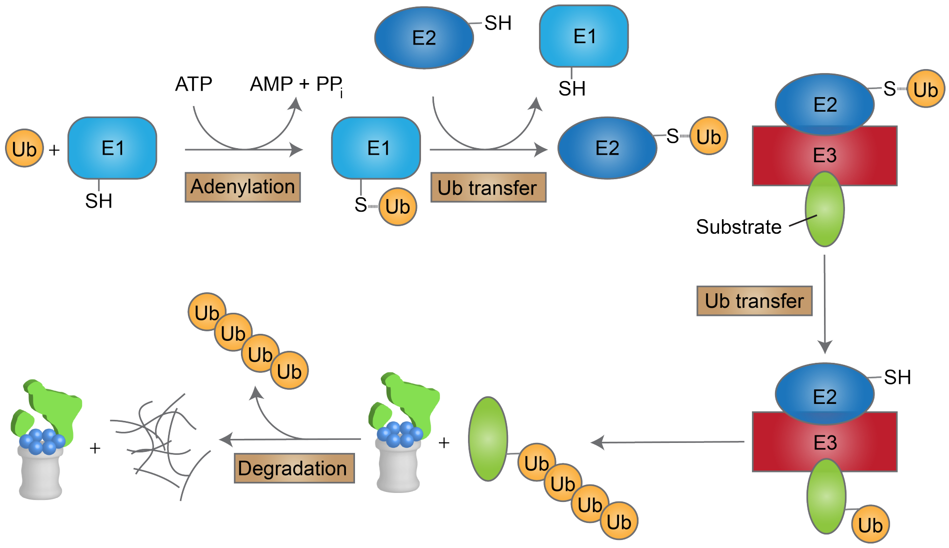

Figure 1.1: **Schematic overview of the UPS system.** An enzyme cascade of E1, E2 and E3 enzymes attach ubiquitin to a target substrate. The ubiquitinated substrate is often degraded by the 26S proteasome. Ubiquitin is hereby recycled. Figure adapted with permission from (Maupin-Furlow, 2012).

By repeating the ubiquitin conjugation reaction, another ubiquitin is attached to a lysine residue of the ubiquitin, thereby forming a poly-ubiquitin (polyUb) chain (Glickman and Ciechanover, 2002; Finley et al., 2012). Substrates carrying a polyUb chain are ultimately recognized by the 26S proteasome (explained in 1.2) and are degraded.

1.1.1 The Variety of Ubiquitin Chains

For extension of a polyUb chain, an isopeptide bond is formed between a lysine of the target protein and the C-terminal carboxyl group of ubiquitin (Gly76). Ubiquitin has seven lysine residues (K6, K11, K27, K29, K33, K48 and K63), all of which can form an isopeptide bond with a ubiquitin moiety. Although all of these chains fulfill different functions (Fig. 1.2), the most commonly used and most-well studied linkages are the K11-, K48- and K63-linked ubiquitin chains (reviewed in (Komander and Rape, 2012)). For example, the K48- and K11-linked chains are typical UPS degradation signals for the 26S proteasome (Kravtsova-Ivantsiv and Ciechanover, 2012; Finley et al., 2012). K63 chains are important for cell signaling pathways, while monoubiquitinated substrates, modified with a single ubiquitin, are important for endocytosis, protein localization and DNA repair (Haglund and Dikic, 2005; Ikeda and Dikic, 2008; Komander et al., 2009). Functions for K6, K27, K29 and K33-linked ubiquitin are not well understood. In addition to the lysine modifications, non-canonical modifications, such as conjugation via cysteine, serine or threonine residues have been identified (McDowell and Philpott, 2013; Finley et al., 2012). The complex ubiquitin code can be additionally modulated by the geometry of the chain, either linear or branched, and by the length of the chain. A substrate can also carry different types of chain linkages, which again increases the diversity of the ubiquitin code and through that the specificity of its function (Komander and Rape, 2012).

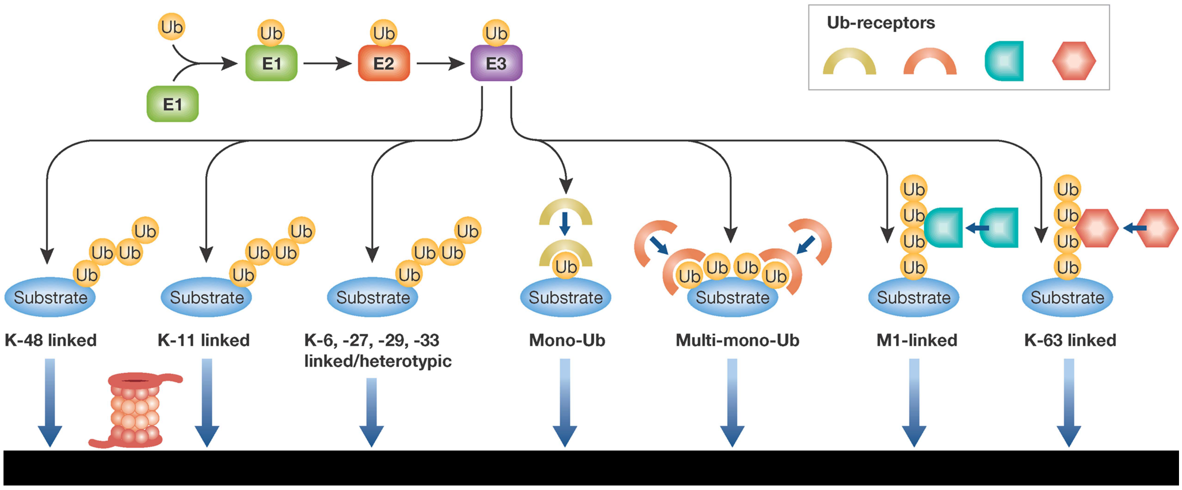

Figure 1.2: **Variation of ubiquitin chains.** The UPS system generates a high variety of ubiquitin chain types. K48 and K11 linked chains are typical signals for degradation by the proteasome. Other types of ubiquitin chains are important for functions such as endocytosis and cell signaling. Figure adapted with permission from (Fulda et al., 2012).

1.1.2 Proteasomal Substrate

The canonical 26S proteasome substrate consists of a polyUb chain with at least four ubiquitins as a targeting signal and an unstructured initiation region, which is needed for degradation initiation (Thrower et al., 2000; Takeuchi et al., 2007; Prakash et al., 2009; Inobe et al., 2011). Several studies have analyzed how each requirement, such as the length and amount of ubiquitin chains, chain position, length of initiation region, length of folded region and amino acid composition affects degradation efficiency (Takeuchi et al., 2007; Prakash et al., 2009; Inobe et al., 2011; Fishbain et al., 2015; Yu et al., 2016b; Lu et al., 2015). The unstructured region is one of the key prerequisites for degradation. If the unstructured region is too short, degradation is hindered and substrate cannot be unfolded. The minimal length requirement for the initiation region is 20-30 amino acids (Inobe et al., 2011). Additionally, it was shown that the amino acid composition of the initiation region has a large impact on the substrate degradation rate. Substrates with unstructured regions containing small side chains, like stretches of glycine or serine residues or acidic stretches of aspartate or glutamate residues, are less efficiently degraded (Yu et al., 2016b; Fishbain et al., 2015). An explanation for this is that overall low complexity sequences, and also highly acidic sequences cannot be grabbed by the pore loops of the ATPase associated with diverse cellular activities (AAA+ ATPase), thus leading to slipping and to hindered unfolding (Kraut et al., 2012; Fishbain et al., 2015). The transcription factor nuclear factor 'kappa-light-chain-enhancer' of activated B-cells (NF-κB) contains such a slippery stop signal, leading to partial degradation of the protein and to the proteasome-mediated activation of its transcription factor activity (Tian et al., 2005). For targeting substrate to the proteasome, it was shown recently that substrates are more efficiently degraded when they have more than one ubiquitin chain. For example, the substrate modified by several diubiquitin chains is more efficiently degraded than that with a tetra-ubiquitin chain (Lu et al., 2015). Although substrate degradation is regulated through the high variability of ubiquitin chains (Thrower et al., 2000; Kravtsova-Ivantsiv and Ciechanover, 2012), how ubiquitin chains exactly control substrate degradation is still not completely understood. Proteins can also be processed by the 26S proteasome through ubiquitin-independent degradation. Here proteins often have either large unfolded regions, through which they can be directly degraded by the 20S core particle (CP), are targeted by a tethering system (Takeuchi et al., 2007) or are fused to proteasome components such as regulatory particle non-ATPase (Rpn) 10 and Rad23 (Janse et al., 2004; Fishbain et al., 2011; Wilmington and Matouschek, 2016; Yu et al., 2016a).

1.2 The 26S Proteasome

The 26S proteasome is a 2.5 MDa protease that functions at the final step of the UPS to degrade targeted proteins. It consists of the barrel-shaped CP, which contains the catalytic active sites, and one or two 19S regulatory particles (RP) (Fig. 1.3). The RP forms the caps of the proteasome and contains the AAA+ ATPase machinery used for unfolding and translocating the substrate into the CP (Smith et al., 2007; Gillette et al., 2008; Tian et al., 2011). Proteasomes can exist in their singly capped or doubly capped form (Peters et al., 1993), which was shown not only *in vitro* but also *in situ*. A doubly capped proteasome measures ~48 nm in length and ~20 nm in width (Voges et al., 1999). Of all 26S proteasome particles found in cells, ~70% were present in the singly capped form and ~30% of proteasomes were found to be doubly capped (Asano et al., 2015; Albert et al., 2017). However, the distribution seems to be affected by cellular environment. Proteasomes found in neurons close to poly-Gly-Ala aggregates were present in the singly capped form in ~24% of the case, and in the doubly capped form in ~76% of the case (Guo et al., 2018).

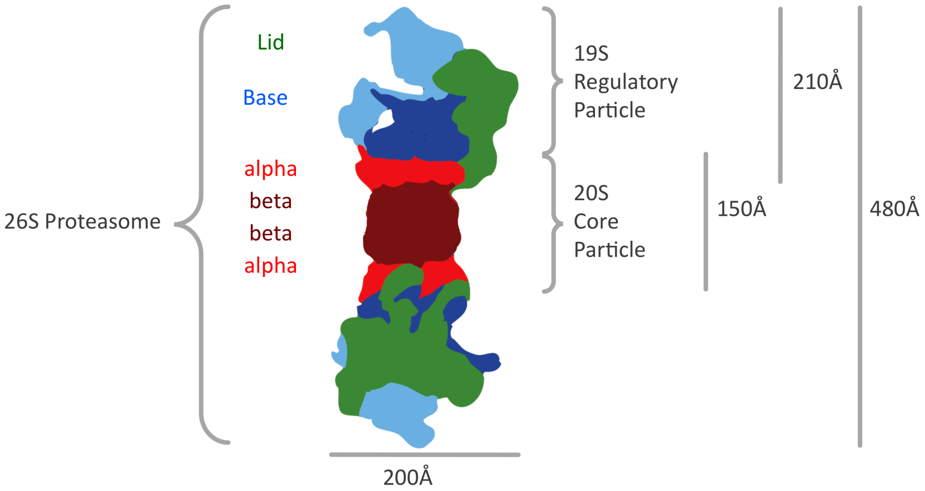

Figure 1.3: **The 26S proteasome.** The 26S proteasome consists of the CP, shown in red and the RP shown in blue and green. The RP can be split into two subcomplexes, the lid (green) and the base (shades of blue). Figure taken with permission from (Unverdorben, 2014).

1.2.1 The 20S Core Particle

The proteasome CP is present in archaea, eukaryotes and also in some bacteria (actinomycetes) (Dahlmann et al., 1989; Nagy et al., 1998). The 28 subunits are divided into two outer α-rings and two inner β-rings; each ring is composed of seven homomeric subunits in bacteria and archaea or seven heteromeric subunits in eukaryotes (Fig. 1.4A) (Lowe et al., 1995; Groll et al., 1997). The two inner rings are composed of distinct β subunits (β1-7), which belong to the class of N-terminal nucleophilic (Ntn) hydrolases (Borissenko and Groll, 2007).

The crystal structure of the CP was first solved from *T. acidophilum* by Löwe and colleagues in 1995 (Lowe et al., 1995) and then from *S. cerevisiae* by Groll and colleagues in 1997 (Groll et al., 1997). In contrast to the homomeric archaeal or bacterial β rings that contain seven catalytic sites, only three of these β subunits are catalytically active in the eukaryotic β rings (Fig. 1.4B). Three catalytic sites display distinct catalytic activities: $\beta1$ possesses caspase-like, $\beta2$ trypsin-like and $\beta5$ chymotrypsin-like activity (Borissenko and Groll, 2007; Finley, 2009; Tomko Jr. and Hochstrasser, 2013). The hydrolases digest substrate into peptides with an average length of seven to nine amino acids (Voges et al., 1999). The active sites are separated from the cellular environment within the confines of three compartments (Wenzel and Baumeister, 1995) and are a common target in drug design of many structurally diverse inhibitors used in medical treatments (Kisselev and Goldberg, 2001; Groll and Huber, 2004).

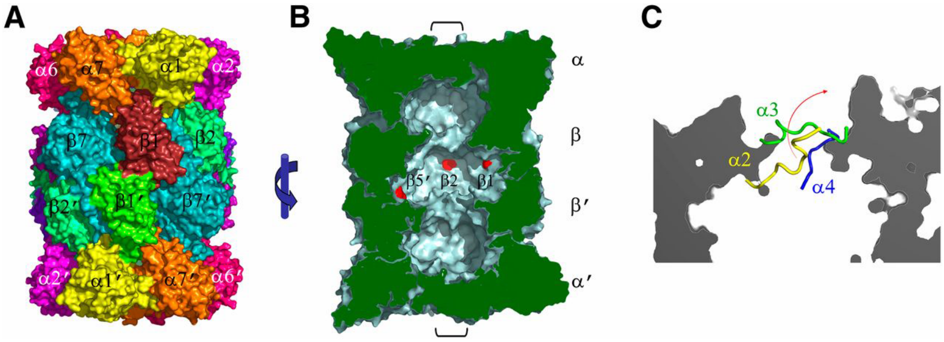

Figure 1.4: **Structure and function of the 20S core particle.** (A) The CP consists of two α rings at the outside each composed of seven different α subunits and in the inside a stack of two β rings, each composed of seven different β subunits. (B) The β rings consist of the proteolytic center and (C) the α ring, especially subunits $\alpha2$, $\alpha3$ and $\alpha4$ are important for gating of the CP. Figure taken with permission from (Finley et al., 2012).

Structural studies revealed that the access to the catalytic chamber is hindered by the N-terminal extensions of the α subunits. While archaea have a disordered CP gate formed by the extensions of the seven copies of one subunit (Lowe et al., 1995; Rabl et al., 2008), an ordered gate is found in eukaryotes. Amongst seven distinct α subunits (α1-7), the N-terminal extensions of the $\alpha2$, $\alpha3$ and $\alpha4$ lay horizontally to form a structured gate (Fig. 1.4C). By restricting the access to the catalytic sites, the proteasome regulates non-specific degradation of untargeted polypeptides (Groll et al., 1997; Finley, 2009; Finley et al., 2016).

1.2.2 The Gate

As described above, the N-terminal extensions of $\alpha2$, $\alpha3$ and $\alpha4$ subunits form a cluster at the pore of the central CP channel to occlude entry of substrates. Mutagenesis studies showed that the Asp7 of $\alpha3$ and Tyr4 and Arg6 of $\alpha4$ stabilize this cluster (Groll et al., 2000). To open the CP gate, association of proteasome activators is required. Such activators are structurally divided into two subclasses (reviewed (Stadtmueller and Hill, 2011)): ATP-dependent activators and ATP-independent activators. ATP-independent activators can be further divided into proteasome activator(PA)200/Blm10 activators, 11S activators (Stadtmueller and Hill, 2011) and a recently discovered ATP-independent activator of the bacterial proteasome, bacterial proteasome activator (Bpa)/proteasome accessory factor E (PafE) (Delley et al., 2014; Bolten et al., 2016).

Binding of proteasome activators can differentially trigger gate opening. For example, gate opening is triggered by binding of 11S activators, such as PA26, through the pushing of an activation loop of PA26 onto a proline loop in each of the α subunit N-termini (Whitby et al., 2000; Forster et al., 2003). This interaction is believed to trigger flipping of the N-terminal extensions of the α subunits (Rabl et al., 2008). Flipping of the α subunit N-terminal extensions results in the formation of an open gate cluster between the N-terminal regions of the α-subunits with two tyrosines, an aspartate and a proline (YD-P-Y motif) (Forster et al., 2005).

The ATPase activators, including the proteasome-activating nucleotidase (PAN) and the RP of the 26S proteasome, are composed of AAA+ ATPases, which form a hexameric ring structure with C-terminal hydrophobic-tyrosine-X (HbYX) motifs that dock into the interface formed between each α subunit. In a structural hybrid study with PAN and PA26/28 it was shown how each tyrosine of the HbYX motif connects to the lysine of the α-helix of the α subunit of the α-ring. It was hereby suggested that binding of all HbYX motifs leads to an overall shift in the α ring and with that leads to gate opening (Yu et al., 2010). In the 26S proteasome only three of the six AAA+ ATPase subunits have a clear conserved HbYX motif. It was confirmed that these three HbYX motifs insert into the CP as shown for other activators. However, in contrast to other activators, the gate remained closed (Unverdorben et al., 2014; Wehmer et al., 2017). Therefore it is still not known how gate opening is regulated.

1.2.3 The 19S Regulatory Particle

Whereas the overall structure of the CP could be determined by crystallization, the structural arrangement of the RP took many years to study. The complete subunit arrangement was finally identified through a combination of crystallization, crosslinking, cryo-electron microscopy (cryo-EM) analysis of the green fluorescent protein (GFP)-labeled and mutated proteasomes and homology modeling (Bohn et al., 2010; Tomko Jr. and Hochstrasser, 2011; Sakata et al., 2012; Beck et al., 2012; Lander et al., 2012; Lasker et al., 2012). The 19S regulatory particle of *S. cerevisiae* consists of 19 stoichiometric subunits which can be further divided into six regulatory particle AAA+ ATPase (Rpt) subunits (Rpt1-6) and 13 Rpn subunits (Rpn1-3, 5-13, 15) (Fig. 1.5) (Glickman et al., 1998b,a; Voges et al., 1999). The RP is further split into two sub-complexes, termed the 'base' and the 'lid' (Saeki and Tanaka, 2012). The base contains the six ATPase subunits, the ubiquitin-receptors Rpn10 and Rpn13 and Rpn1, and a scaffold protein Rpn2. The lid contains the remaining subunits Rpn3, Rpn6-9, 11-12 and Sem1/Rpn15. Only Rpn11 possesses an enzymatic activity as a deubiquitinating enzyme (reviewed in (Forster et al., 2010; Tomko Jr. and Hochstrasser, 2013)).

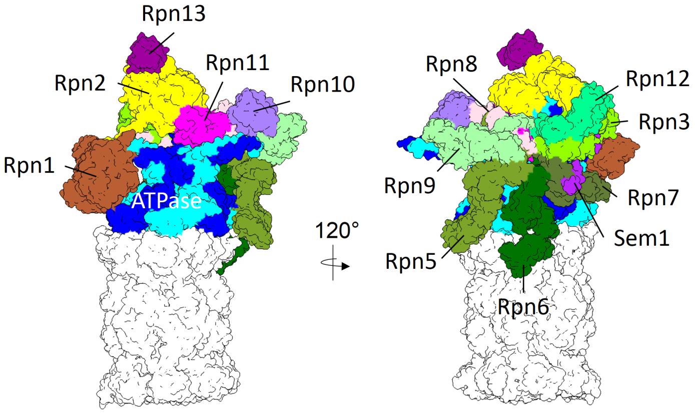

Figure 1.5: **The Regulatory Particle.** The RP is shown with each subunit colored differently: Rpt1,6,4 (blue), Rpt2,3,5 (cyan), marked as ATPase, Rpn1 (brown), Rpn2 (yellow), Rpn3, Rpn5, Rpn6, Rpn7, Rpn9, Rpn12 (shades of green), Rpn8, Rpn10, Rpn11, Rpn13, Sem1 (shades of purple). Figure taken with permission from (Wehmer, 2017).

1.2.3.1 The Lid

The lid of the proteasome acts as the scaffold of the 26S proteasome. The lid consists of nine subunits Rpn3, Rpn5, Rpn6, Rpn7, Rpn8, Rpn9, Rpn11, Rpn12 and Sem1. Rpn3, 5, 6, 7, 9 and 12 share the proteasome-COP9-initiation factor (PCI)-domain. All six are arranged as a horseshoe through interactions with their PCI-domains, and are located on the side of the base subunits reaching across the full width of the RP (Lasker et al., 2012; Lander et al., 2012). The N-termini of Rpn3 and Rpn12 interact with Rpn2 whereas the N-termini of Rpn5 and Rpn6 contact the ATPase as well as the CP. The Mpr1/Pad1 N-terminal (MPN)-domain subunits Rpn8 and Rpn11 are located at the center of the RP. Although both Rpn8 and Rpn11 belong to the deubiquitinating enzyme (DUB) family with a Zn^{2+} dependent JAB1/MPN/Mov34 metalloenzyme (JAMM) domain, only Rpn11 is catalytically active and Rpn8 has a pseudo catalytic site (Verma et al., 2002; Yao and Cohen, 2002; Pathare et al., 2014; Worden et al., 2014; de Poot et al., 2017). The Rpn8/Rpn11 heterodimer resides at the interface on the inside of the PCI horseshoe, at the entrance of the ATPase ring and between the ubiquitin receptors Rpn10 and Rpn13. A common structural motif in proteins of the MPN family are the two insertion loops, Ins-1 and Ins-2, which are important for regulation of deubiquitination (Worden et al., 2017). The catalytic activity of Rpn11 is inhibited in an isolated lid subcomplex through an interaction with Rpn5 which occludes the active site of

Rpn11. As soon as the lid is incorporated into the holocomplex, subunits in the lid undergo conformational changes, most notable being that the Rpn11/Rpn8 dimer undergoes a 90° rotation through which Rpn11 is no longer occluded by Rpn5. Still the active center of Rpn11 is blocked by an inactive, closed state of Ins-1 loop (Lander et al., 2012). Activity of Rpn11 is coupled to substrate translocation and requires ATP hydrolysis (Worden et al., 2014; Dambacher et al., 2016). In detail, during substrate engagement the active site of Rpn11 moves above the entrance of the central pore. Further the inactive closed conformation of the Rpn11 Ins-1 loop undergoes a conformational change through ubiquitin binding leading to an active, open β-hairpin state of Ins-1 (Worden et al., 2017). Finally substrate can be deubiquitinated. Importantly the substrate should not be deubiquitnated before it is translocated but deubiquitination should also not occur too late to prevent co-degradation of ubiquitin or stalling of the substrate.

1.2.3.2 The Base

The base of the RP is composed of the AAA-ATPase (discussed in 1.2.4), three ubiquitin receptors (Rpn13, Rpn10 and Rpn1) and the binding platforms Rpn1 and Rpn2. Rpn10 and Rpn13 are located at the periphery of the RP and recognize the ubiquitin chain attached to the target substrate (van Nocker et al., 1996; Schreiner et al., 2008; Husnjak et al., 2008). Rpn13 binds to Rpn2 and Rpn10 binds to Rpn8 and Rpn9 (Chen et al., 2010; Beck et al., 2012; Lander et al., 2013). Rpn10 consist of an N-terminal von Willebrand A (VWA) domain and a C-terminal ubiquitin interacting motif (UIM) domain. It recognizes ubiquitin through binding to its UIM (Deveraux et al., 1994; Riedinger et al., 2010). The Rpn10 UIMs form helices, which are very flexibly connected to the VWA domain. The Rpn10 subunit from different organisms has a variable amount of UIMs (reviewed in (Tomko Jr. and Hochstrasser, 2013)). Rpn13 uses a pleckstrin-like receptor for ubiquitin (PRU) domain to recognize and bind ubiquitin. This domain cannot only interact with ubiquitin but it also binds to Rpn2 (Husnjak et al., 2008). Because Rpn10 and Rpn13 are not essential in *S. cerevisiae*, it is likely that more ubiquitin receptors or additionally shuttling factors also participate in recognizing polyUb substrates (Sakata et al., 2012; Husnjak et al., 2008).

Rpn1 and Rpn2 are the largest subunits in the RP. Both subunits are highly similar in structure with a toroid built from 11 proteasome/cyclosome (PC)-motifs (He et al., 2012). Both are connected to one another through a loop of Rpn2 and to the ATPase ring via the coiled-coil of Rpt1-Rpt2 for Rpn1 and Rpt6-Rpt3 for Rpn2 (Wehmer et al., 2017; Schweitzer et al., 2016). Rpn1 and Rpn2 are additionally connected to many different integral subunits of the 26S proteasome. Rpn1 is a docking platform for both the substrate and ubiquitin and it was also shown to be a hub for proteasome interacting protein (PIP) binding (Gomez et al., 2011; Aufderheide et al., 2015; Shi et al., 2016). Rpn1 recognizes ubiquitin-like (UBL) domains of substrate shuttling factors using its T1 site, which is also important for ubiquitin-binding. It has a second UBL-binding site (T2) where the deubiquitinating enzyme Ubp6 binds. The high flexibility of Rpn1 makes it difficult to resolve all functions of this central hub (Wehmer et al., 2017; Schweitzer et al., 2016).

1.2.4 The ATPase

The six AAA+ ATPase subunits Rpt1-6 assemble into the AAA-ATPase ring, which sits directly on top of the CP (Fig. 1.6B). The N-terminus of each Rpt subunit forms a coiled-coil with the neighboring subunit (Rpt1-Rpt2, Rpt6-Rpt3, Rpt4-Rpt5) (Tomko Jr. et al., 2010; Tomko Jr. and Hochstrasser, 2011). These coiled-coils are distorted as a result of the repeating of every seven residues, normally the number of residues per α-turn is 3.6 (Lupas and Gruber, 2005). The coiled-coil region of Rpt1-Rpt2 interacts with Rpn1 (and Rpn2) and the coiled-coil of Rpt6-Rpt3 with Rpn2, while the one of Rpt4-Rpt5 is isolated and has no interaction with the other subunits. The Rpt N-terminus connects to the oligosaccharide-binding (OB) domain, which is important for the structural stability of the hexamer which is followed by the AAA+ domain with a large subdomain in the middle and a small subdomain at the C-terminus (Fig. 1.6A, C) (Forster et al., 2009; Tomko Jr. et al., 2010; Bard et al., 2018).

At the interface of the large and small domain of an ATPase subunit and the large domain of the neighboring subunit, a nucleotide pocket is formed which can bind ATP, then hydrolyze ATP to form ADP+Pi (Fig. 1.6D). As with other AAA-ATPase members, the nucleotide pocket is highly conserved, containing a Walker A, Walker B motif, sensor 1 and sensor 2 motif. Hydrolysis of ATP is assisted by two conserved arginine fingers from the neighboring Rpt subunit (Fig. 1.6A). These arginine fingers reach towards the Walker A motif and polarize the gamma-phosphate (reviewed in (Wendler et al., 2009)). The highly conserved glutamate of the Walker B motif, often located at the end of an adjacent β-strand, polarizes a water molecule for attack of the γ-phosphate. ATP is finally hydrolyzed and energy is generated, which leads to movement of the ATPase subunits. For the substrate translocation, conserved aromatic-hydrophobic (Ar-θ) pore loops at the large domain are important. They face the inner channel of the ATPase and interact with an incoming substrate and pull it towards the CP in an ATP-dependent manner (Lander et al., 2012, 2013; Iosefson et al., 2015).

The coordination of the whole ATPase cycle is still unclear. In higher activated 26S proteasome states (discussed below) a rigid body can be found between Rpt subunits formed by the small AAA+ subdomain and the large AAA+ subdomain of the clockwise neighboring subunit (Matyskiela et al., 2013; Sledz et al., 2013; Unverdorben et al., 2014; Wehmer et al., 2017; Bard et al., 2018). Such rigid bodies have been reported in other AAA+ motors, for example in PAN or the translocase ATP-dependent caseinolytic protease X (ClpX) and structures of

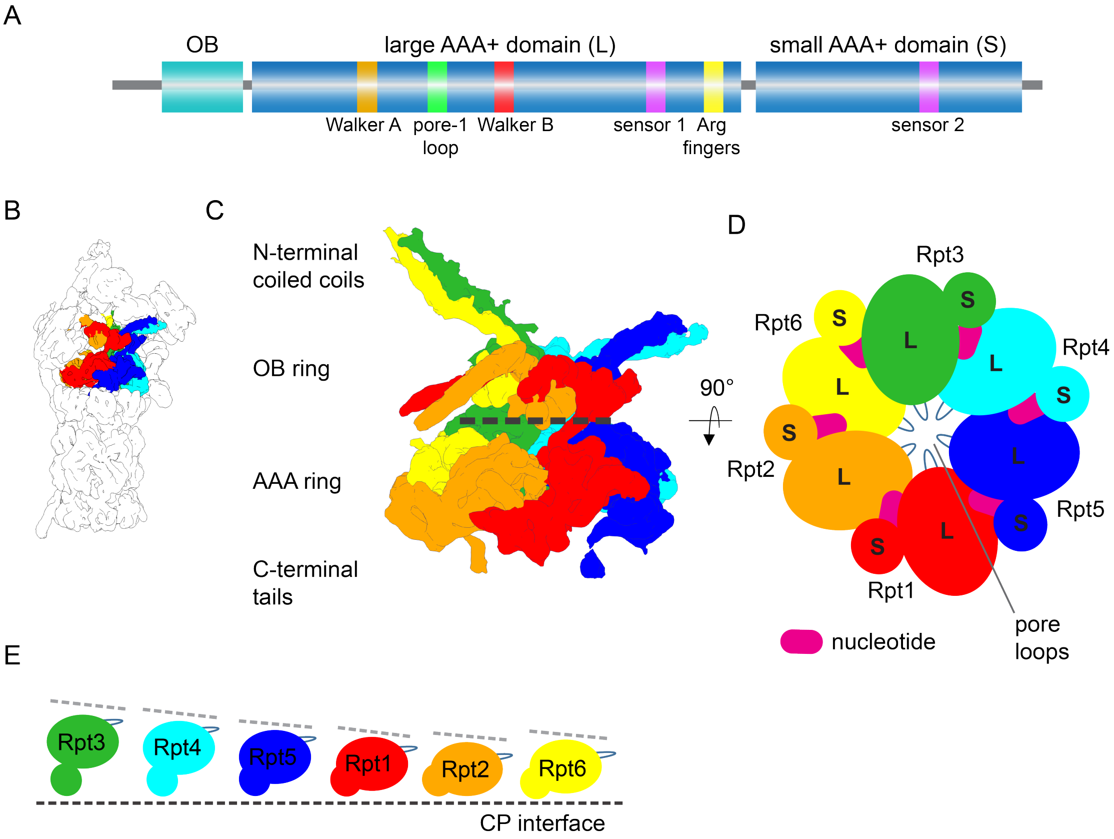
A
OB
large AAA+ domain (L)
small AAA+ domain (S)
Walker A
pore-1 loop
Walker B
sensor 1
Arg fingers
sensor 2
B
C
N-terminal coiled coils
OB ring
AAA ring
C-terminal tails
90°
D
Rpt3
Rpt6
Rpt4
Rpt2
Rpt5
Rpt1
S
L
nucleotide
pore loops
E
Rpt3
Rpt4
Rpt5
Rpt1
Rpt2
Rpt6
CP interface

Figure 1.6: **The ATPase of the base subcomplex.** (A) Schematic overview of an Rpt subunit. (B) Position of the ATPase with the six Rpt subunits colored in the following colors: Rpt1 (red), Rpt2 (orange), Rpt3 (green), Rpt4 (cyan), Rpt5 (blue), Rpt6 (yellow) (C) Side view of the ATPase. The line splits the OB ring from the AAA-ring. (D) Top view of the ATPase ring with its six subunits. Shown in pink is the location of the nucleotides. (E) Cartoon of the lock washer conformation of each subunit split into the small and large AAA+ domains. This lock washer conformation can be seen especially in the s1 and s2 states.

AAA+ motors processing substrate (Zhang et al., 2009; Glynn et al., 2009, 2012; Monroe et al., 2017; Puchades et al., 2017). Additionally, whether a clockwise burst mechanism or a hand-over model with a counter-clockwise direction is more likely is not clear.

1.2.5 Structure and the Conformational States

In recent years, cryo-EM single-particle analysis (SPA) (described in 1.3) was used to capture the proteasome in different processing states. The purified 26S proteasome complexes are subjected to cryo-EM SPA and the obtained 26S proteasome densities are computationally classified into different conformational states (Fig. 1.7). These previous studies revealed that the 26S proteasome undergoes large movements during substrate proteolysis. In the presence of ATP, where the proteasomes actively hydrolyze ATP, the two structural states s1

(Bohn et al., 2010; Lander et al., 2012; Lasker et al., 2012; Beck et al., 2012; Unverdorben et al., 2014) and s2 were identified (Unverdorben et al., 2014). An additional state, s3, was resolved by adding the nucleotide analog ATPγS (Sledz et al., 2013). ATPγS hinders hydrolysis by the ATPases and may play an activating role for the 26S proteasome. The s3 state was also achieved by adding a synthetically designed substrate, thus supporting the hypothesis that s3 is an activated proteasome state (Matyskiela et al., 2013).

When these states are compared to one another, s1 represents the ground state in which the OB ring, AAA+ ATPase ring and the CP are not aligned (Fig. 1.7B). The ATPase is arranged in a lock washer conformation with the split site between Rpt6 and Rpt3 (Unverdorben et al., 2014; Wehmer et al., 2017), with Rpt3 being the highest subunit (Fig. 1.6E). From the s1 to the s2 state the arrangement of the ATPase does not change, but rather the whole ATPase shifts, thereby better aligning the ATPase channel with the CP channel (Fig. 1.7B). At the same time, the lid subunits and Rpn2 undergo a 25° rotation, through which the distance between the N-terminus of Rpn5 and Rpn6 increases and Rpn11 moves above the entrance to the pore of the ATPase, important for facilitating the DUB activity (Fig. 1.7A, C). From s2 to s3 Rpn2 shifts by another ∼24 Å and the co-axial alignment of OB ring, AAA+ ATPase ring and CP increases further. Also from s2 to s3 the lock washer of the ATPase arrangement becomes more planar, moving the split site to Rpt1-Rpt5 (Unverdorben et al., 2014; Wehmer et al., 2017).

A fourth state, s4, could be stabilized in a low percentage using the nucleotide analog BeF_x (Wehmer et al., 2017). s4, similar to s3, has a well aligned ATPase and CP channel. On first sight s3 and s4 are similar but three important differences can be found. First, the ATPase of s4 is similar to s3, both are more planar, but the split site is located at Rpt4-Rpt3. Second, the N-terminus of Rpn1 points away from the ATPase in the s3 state, while in s4 the Rpn1 N-terminus is fixed towards the ATPase. And third, s4 is the first 26S proteasome state that has an open CP gate. In contrast the s1, s2 and s3 states have a closed gate (Fig. 1.7B). The lower resolution of roughly 8 Å of the s4 state left questions remaining regarding the gate opening mechanisms.

Human *in vitro* studies have shown four comparable states S_A, S_B, S_C and S_D (Chen et al., 2016), suggesting that the proteasome state landscape is likely conserved between yeast and human. Recent technological advancements made it possible to use cryo tomography to view inside a cell, that was plunge frozen to maintain the native cellular state. Such in situ studies were used to analyze proteasome abundance and proteasome localization. These studies even allowed for differentiation between different 26S proteasome states. Ground state proteasomes, s1 and activated states s3 and s4 were resolved (Asano et al., 2015; Albert et al., 2017; Guo et al., 2018). The activated states could be shown in a higher abundance when proteasomes close to protein aggregates in neurons were analyzed (Guo et al., 2018).

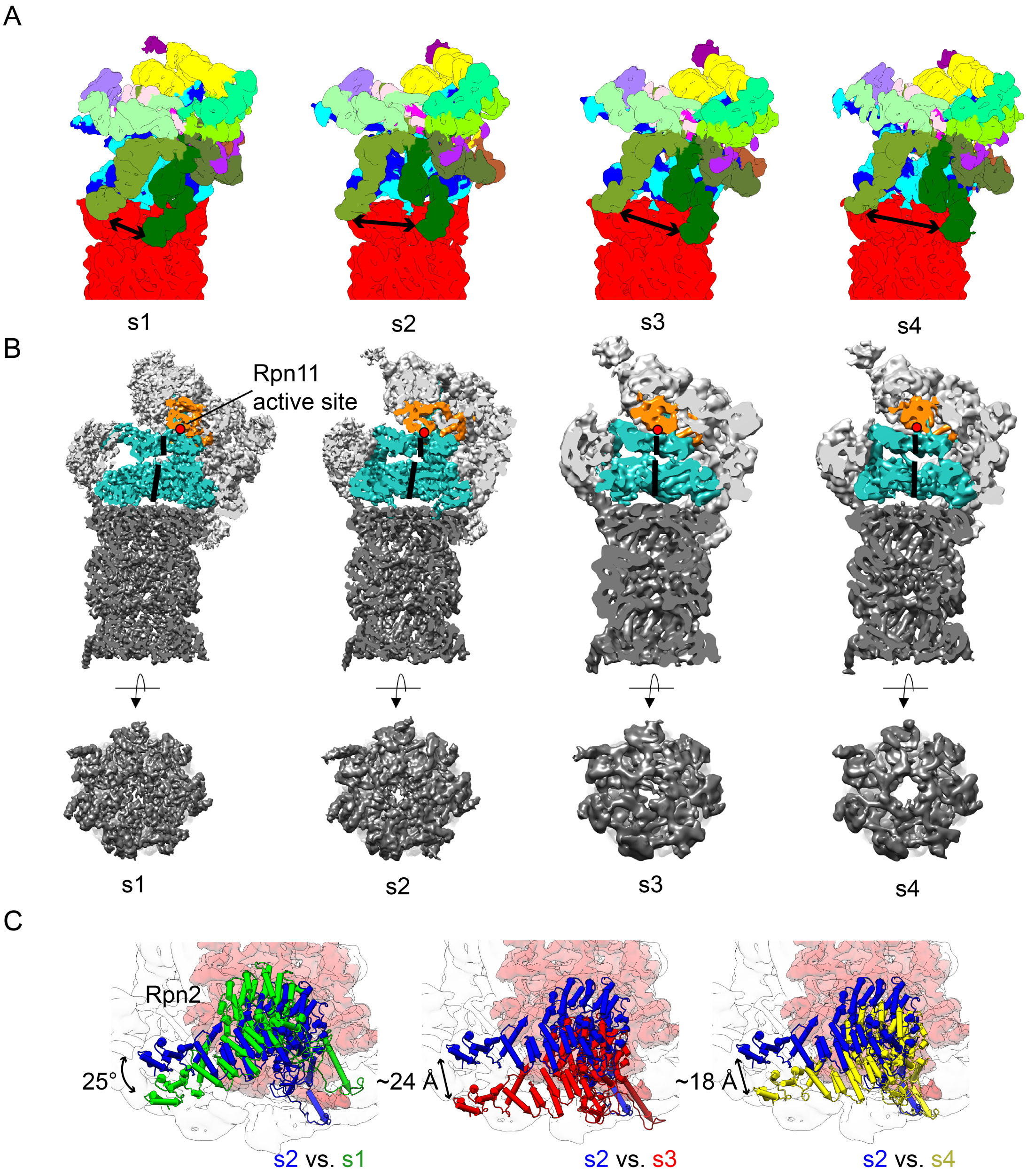
A
s1
s2
s3
s4
B
Rpn11
active site
s1
s2
s3
s4
C
Rpn2
25°
~24 Å
~18 Å
s2 vs. s1
s2 vs. s3
s2 vs. s4

Figure 1.7: **The proteasome conformational state landscape.** (A) cryo-EM densities of the four published proteasome states. The distance between Rpn5 (olive green) and Rpn6 (dark green) is shown as an arrow. (B) A side view of the cryo-EM densities cut in the middle shows the position of the active site of Rpn11 and the alignment of the OB ring, the AAA+ ATPase ring and the CP in each state. An additional top view of the CP shows the state of the gate. (C) Top view of Rpn2 overlaid between two states and compared by position and orientation.

1.3 3D Cryo-Electron Microscopy

The primary goal of structural biology is to better understand the functions and interactions of macromolecules and to use this information for rational drug design in combating human disease. Several techniques are available for determining the three dimensional structure of a macromolecule, including X-ray crystallography, nuclear magnetic resonance (NMR) and cryo-EM. One of the restricting factors of high-resolution structure determination using microscopes is the wavelength of visible light (Förster et al., 2012; Engelhardt, 2018). The advantage of an electron microscope is that it uses high-energy electrons with a much smaller wavelength than visible light, thus making it more suitable for high-resolution structural work. In this doctoral thesis, I applied cryo-EM to address the conformational equilibrium of the 26S proteasome. In cryo-EM, biological samples are rapidly frozen (described in 1.3.2) to capture the sample in its hydrated state in non-crystalline ice with a transmission electron microscope (TEM) under cryogenic condition. For high-resolution structure determinations of biological macromolecules, three methods were developed using cryo-EM: electron crystallography, cryo-electron tomography (CET) and SPA (Baumeister and Steven, 2000; Lučić et al., 2008; Engelhardt, 2018). In electron crystallography the structure of proteins, for example membrane proteins embedded in a lipid layer, is determined, which preferably form two-dimensional (2D) crystals by a periodical arrangement (Baumeister and Steven, 2000). In CET, micrographs of biological samples are acquired at multiple tilt angles from which a three-dimensional (3D) volume can be reconstructed. It is combined with in situ structural analysis, providing a macromolecular structure close to the native condition (Lučić et al., 2008; Förster et al., 2012). SPA is one of the methods which allows the determination of the 3D structure of macromolecules at high-resolution. A purified protein sample is rapidly frozen and then recorded on a TEM without tilting. All projections of the macromolecules with different orientations are combined together and reconstructed to a 3D structure (Frank, 2006), which can be further classified into possible subconformations (Spahn and Penczek, 2009; Bai et al., 2015).

1.3.1 Transmission Electron Microscopes

In the TEM, highly accelerated electrons are "shot" onto a sample of interest and scattered electrons are detected by a detector after passing through the sample. The assembly and composition of a TEM is quite similar to that of a light microscope (Fig. 1.8). In short, the electron source sits at the top of the microscope in the form of a field emission gun (FEG). Through a strong electrical field, generated by voltages of up to 300 V, electrons are extracted and accelerated to form a beam of highly coherent electrons. The microscope is steadily kept under high vacuum conditions (usually 10^{-10} bar) to prevent any noisy interactions of electrons with gas atoms (Williams and Carter, 2009). Electromagnetic condenser lenses and corresponding apertures (e.g. C1, C2 and C3 in the Titan Krios (FEI)) control the electron beam by focusing and parallelizing it onto the grid stage.

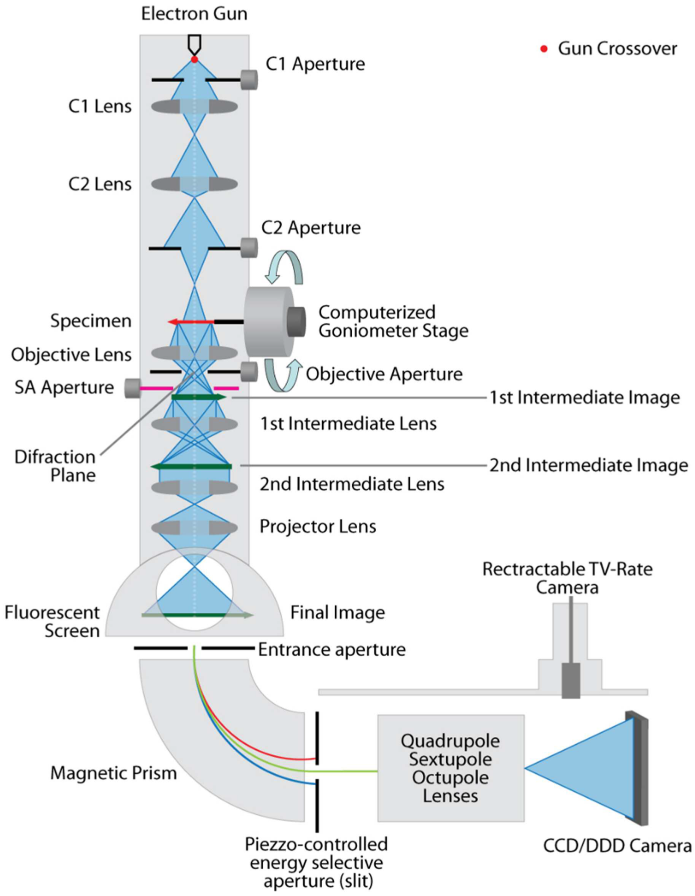
Electron Gun
Gun Crossover
C1 Aperture
C1 Lens
C2 Lens
C2 Aperture
Computerized Goniometer Stage
Specimen
Objective Lens
Objective Aperture
SA Aperture
1st Intermediate Image
1st Intermediate Lens
Diffraction Plane
2nd Intermediate Image
2nd Intermediate Lens
Projector Lens
Rectractable TV-Rate Camera
Fluorescent Screen
Final Image
Entrance aperture
Magnetic Prism
Quadrupole Sextupole Octupole Lenses
CCD/DDD Camera
Piezzo-controlled energy selective aperture (slit)

Figure 1.8: **Schematic overview of an electron microscope.** Schematic overview of an electron microscope used for single particle analysis in this work. Figure taken with permission from (Asano, 2015).

High-energy electrons will hit the sample on the grid stage and are either scattered by the sample or traverse the sample unscattered. A first projection image is then created by electrons passing the objective lens. The objective aperture is important for filtering electrons scattered at high angles. The projector lens enlarges the projection to generate a final image (Reimer and Kohl, 2008; Williams and Carter, 2009). In the early years of cryo-EM acquisition, the image was recorded on photographic film, and in later years digital recorders became more common (reviewed in (Booth and Mooney, 2013)). These digital recorders were charge coupled device (CCD)-based or complementary metal oxide semiconductor (CMOS) cameras which convert the incoming electrons into photons and further into an electronic signal for readout. Recent advances in single particle analysis cryo-EM were largely provided by technical innovation of direct electron detection devices (DDD). The DDD measures electrons directly through a semiconductor membrane (Booth and Mooney, 2013). Direct detectors come with many advantages, for example they have an improved detection quantum efficiency (DQE) for high spatial frequencies (high-resolution information) thus resulting in an improved signal-to-noise ratio (SNR) (Ruskin et al., 2013; McMullan et al., 2014). Direct detectors can additionally record subframes for each acquired image. Frame alignment during image processing can correct for drift and weighing the frames, for example discarding the last frames, helps to reduce the effects of beam damage to the sample (Bai et al., 2015). All data in this thesis was acquired with the help of the Gatan K2 detector. The counting mode of the K2 detector can additionally localize incoming electrons more precisely and suppress electronic noise (Booth and Mooney, 2013). A total dose of high-energy electrons per area has to be controlled because an electron beam can damage the sample. Acquiring images with too few electrons also limits the signal-to-noise ratio (SNR) and thereby the resolution. Each acquired micrograph is influenced by several factors as determined by the microscope setup. The frequencies of the image are modulated by the CTF. During processing the acquired images can be corrected for the CTF by estimating defocus and accounting for the microscope parameters such as the spherical-aberration coefficient (Engelhardt, 2018).

1.3.2 Sample Preparation for Cryo-Electron Microscopoy

As described above, rapid freezing of the biological sample is needed to keep the biological sample in its hydrated state (Engelhardt, 2018). In more detail, the purified sample is pipetted as a small volume onto a grid designed for cryo-EM. These grids are often made of copper, and are covered by a carbon film with a regular or a random distribution of holes. The grid can influence the orientation of the macromolecule and can even affect the amount of sample that is embedded in ice. For a successful high-resolution structure determination, an equal distribution of orientations and a high amount of particles that are not aggregated in ice is preferred. Before sample application the hydrophobic carbon-coated grids are made temporarily hydrophilic with ionized gas molecules in a plasma cleaner (Engelhardt, 2018). After applying the sample onto the carbon-coated grid, the grid is plunge frozen into a cryogen, such as liquid ethane, which is cooled to -180 °C through liquid nitrogen. The water molecules are transformed into a vitreous ice state before forming crystalline ice because of the high cooling rate of 100,000 Cs^{-1}. Vitreous ice does not affect the density of the macromolecule or the interactions between the biological sample. Importantly, vitreous ice keeps the sample very translucent making it the perfect sample for cryo-EM data acquisition (Engelhardt, 2018). The plunge frozen sample needs to remain at -180 °C during the entire cryo-EM data acquisition to stay fixed onto the grid.

1.4 Single-Particle Analysis

As mentioned in the summary above, in SPA a protein or often a protein complex is purified, applied to a microscope grid and plunge frozen. The frozen sample is then subjected to TEM, as described above. The principle of SPA is averaging multiple views (referred to also as a projection) of many copies of your protein of interest which are embedded in ice. From the acquired micrographs, the particles are picked and used to reconstruct the 3D structure (reviewed in (Frank, 2009; Orlova and Saibil, 2011; Förster et al., 2012; Nogales and Scheres, 2015)). Because individual particles have a very low SNR through the restriction of beam damage, projections of a large number of single particles are required to construct a 3D structure with a high resolution. Typically, the micrographs contain dozens to hundreds of the projections. The whole data set consists of several thousand micrographs. The amount of particles required to achieve a desired resolution is dependent on many different factors, including preferred orientations, ice thickness and flexibility of the protein of interest.

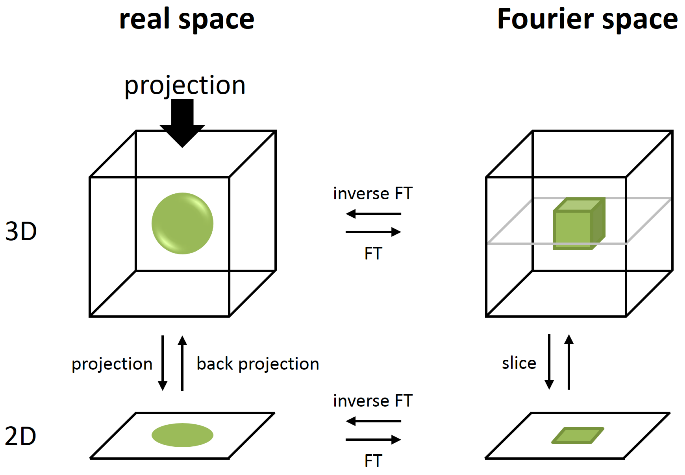

Figure 1.9: **Projection-slice theorem.** The projection-slice theorem shown as cartoon scheme. The projection of a 3D object transformed into Fourier space is equal to a slice of the same 3D object transformed into Fourier space. FT = Fourier transformation. Figure taken with permission from (Wehmer, 2017).

1.4.1 3D Reconstruction in SPA

3D reconstruction in SPA is based on the projection-slice theorem. This means that the projection of a 3D volume in real space is identical to a central slice in the corresponding direction in Fourier space (Fig. 1.9) (reviewed in (Förster et al., 2012; van Heel et al., 2000)). To reconstruct a 3D volume, position and projection directions of each particle need to be determined so that the slices in the Fourier space can be used for a 3D volume reconstruction. 'Projection matching' is most commonly used to obtain the required parameters. Projection matching is done iteratively over two steps. In the first step, a priori knowledge of a volume is used as a reference and the reference is compared with each experimental projection to find maximum cross correlation values or the maximum likelihood or maximum a posteriori function. Using the determined parameters, a 3D volume is reconstructed in the second step. There are several different real-space and Fourier-space reconstruction algorithms. In all methods, projections assigned to the same angular class are averaged to give one average for each angular view. Each class average conceptually fills up the 3D Fourier space and a back-transformation leads to a 3D volume. These two steps are iteratively repeated using the 3D volume of the previous step as the next reference volume until the optimization converges (Frank, 2006; Förster et al., 2012).

1.4.2 Conformational Heterogeneity and 3D Classification

As described earlier, many particles from the same protein sample are combined and used to reconstruct a 3D volume. However, proteins, especially protein complexes, adopt different conformations to fulfill different functions. Algorithms can help to group particles *in silico* into conformationally distinct classes (reviewed in (Spahn and Penczek, 2009; Bai et al., 2015)). Classification of acquired particles can be carried out on the 2D image level and also on the 3D image level. 2D classification most often cannot differentiate between conformations or different angular views. This method is still often used for an initial sorting of particles. Thereby, the 3D classification method is commonly used to sort conformational heterogeneity of the proteins of interest. Two methods of 3D classification are widely used; multi-reference alignment and 3D principle component analysis (PCA). Multi-reference alignment, which was used in this thesis, uses projection matching to compare particle subsets to subsequent reconstructions.

1.5 Objective and Aims

Over the past several years, the understanding of the molecular details of the 26S proteasome has reached a very high level. Enhancements in microscope and camera technology have resulted in high-resolution structures of the 26S proteasome and have made it possible to begin to understand the mechanics of protein degradation by the 26S proteasome. Presently, the understanding of 26S proteasomal degradation is hypothesized as cycling through four different states of the 26S proteasome. However, it was not known exactly how the 26S proteasome changes its conformation upon ATP hydrolysis and how substrate degradation is regulated by CP gating. This thesis will focus on stabilizing low-abundance states, identifying new states through modification of the 26S proteasome state landscape and investigating the functional consequences of such modifications.

In the first part of the thesis, I used three different methods to modify the 26S proteasome state landscape. (I) The nucleotide analogs BeF_x or ATPγS were used in the past to modify the 26S proteasome. An exact analysis of the influence of nucleotide analog concentration on the 26S proteasome was not carried out before. Here I purified the 26S proteasome in the presence of different ATPγS concentrations and analyzed the results at the structural level. (II) Nucleotide analogs should act as inhibitors of the AAA+ ATPase. In a more controlled fashion, AAA+ ATPase point mutations were used to modify the AAA+ ATPase. The resultant mutant proteasomes were then analyzed for their structural configuration and state distribution. (III) Finally, I designed a model substrate and used it for structural work with the aim of analyzing the influence of the substrate on the 26S proteasome degradation machinery.

In the second part of the thesis, I analyzed all states in detail to answer questions regarding the still unknown gate opening mechanism and the AAA+ ATPase cycle. Analysis of new states should hereby fill the understanding of the degradation cycle and bring us closer to understanding the 26S proteasome.

Chapter 2

Materials and Methods

2.1 Materials

2.1.1 Chemicals and Consumables

Table 2.1: Chemicals and consumables

chemical	source
Adenine	Sigma
Agarose, low EEO	Sigma
Adenosine 5'-(3-thiotriphosphate) (ATPγS)	Roche
Adenosine triphosphate (ATP)	Sigma
Anti-FLAG® M2 Affinity Gel	Sigma
Anti-FLAG® M2 Magnetic Beads	Sigma
Bio-Rad protein assay dye	Bio-Rad
Bovine serum albumin (BSA)	Sigma
Bacto™ Agar	BD
Bacto™ Tryptone	BD
Bacto™ Peptone	BD
Bacto™ Yeast Extract	BD
BL21-STAR (DE3)	EMD Millipore
Creatine phosphate (CPh)	Sigma
Creatine phosphate kinase (CPK)	Sigma
1 kb DNA Ladder	NEB
Deoxynucleotide solution	NEB
DH5α competent cells	ThermoFisher
Dithiothreitol (DTT)	Merck
ECL™ Western Blotting Reagents	Merck
Ethane/Propane (37% ethane/63% propane)	Linde

chemical	source
Ethylenediaminetetraacetic acid (EDTA)	Merck
FastDigest Enyzmes	ThermoFisher
3xFLAG peptide (DYKDHDGDYKDHDIDYKDDDDK)	MPI core facility
α-D(+) Glucose monohydrate	Roth
Glycerol 86-88%	Roth
Hydrochloric acid (HCl)	Merck
N-2-Hydroxyethylpiperazine-N'-2-ethanesulfonic acid (HEPES)	Biomol
Imidazole	SERVA
In-Fusion® HD Cloning Kit	Clontech
Immobilon-P Membrane	Serva
Isopropyl β-D-1-thiogalactopyranoside (IPTG)	Sigma
Kanamycin	Sigma
Magnesium chloride ($MgCl_2$)	Merck
Methanol	Sigma
MG132	Sigma
3-(N-Morpholino)propanesulfonic acid (MOPS) running buffer	ThermoFisher
NuPAGE® 4-12% Bis-Tris Protein Gels	ThermoFisher
NuPAGE® LDS Sample Buffer	ThermoFisher
One Shot™ TOP10	ThermoFisher
1,10-phenantrholine (*o*PA)	Sigma
Phusion® High-Fidelity DNA Polymerase	NEB
Poly-L-lysine solution	Merck
Potassium dihydrogen phosphate	Roth
QIAquick Gel Extraction Kit	QIAGEN
QIAprep Spin Miniprep Kit	QIAGEN
SeeBlue® Plus2 Pre-stained Protein Standard	invitrogen
Skim milk powder	Sigma
Sodium chloride (NaCl)	Merck
Sodium dodecyl sulfate (SDS)	Roth
Suc-LLVY-AMC	bio-techne
Sucrose	Merck
Super Optimal broth with Catabolite repression (SOC) medium	Sigma
SYBR™ Safe DNA Gel Stain	ThermoFisher
50X Tris-acetate-EDTA (TAE)	ThermoFisher
Tris Base	Sigma
Ubiquitin Antibody HRP	Santa Cruz
Uranyl acetate (UA)	Merck

2.1.2 Buffers and Solutions

All buffers and solutions were produced using deionized water from a Milli-Q Plus Ultrapure Water (dH_2O) Purifier.

Table 2.2: Protein analysis buffers

buffer	ingredients
Buffer A	50 mM Tris-HCl pH 7.4, 100 mM NaCl, 10 mM $MgCl_2$, 4 mM ATP, 25 mM CPh, 10 U/ml CPK, 10% (vol/vol) glycerol
Buffer A - EQ mutants	100 mM Tris-HCl pH 7.4, 100 mM NaCl, 4 mM $MgCl_2$, 4 mM ATP, 10% (vol/vol) glycerol
Sucrose buffer, 4 mM ATP (15%)	20 mM HEPES pH 7.4, 40 mM NaCl, 5 mM DTT, 10 mM $MgCl_2$, 4 mM ATP, 25 mM CPh, 10 U/ml CPK, 15% (wt/vol) sucrose
Sucrose buffer, 4 mM ATP (45%)	20 mM HEPES pH 7.4, 40 mM NaCl, 5 mM DTT, 10 mM $MgCl_2$, 4 mM ATP, 25 mM CPh, 10 U/ml CPK, 45% (wt/vol) sucrose
Sucrose buffer, 2 mM ATPγS (15%)	20 mM HEPES pH 7.4, 40 mM NaCl, 5 mM DTT, 10 mM $MgCl_2$, 2 mM ATPγS, 15% (wt/vol) sucrose
Sucrose buffer, 2 mM ATPγS (45%)	20 mM HEPES pH 7.4, 40 mM NaCl, 5 mM DTT, 10 mM $MgCl_2$, 2 mM ATPγS, 45% (wt/vol) sucrose
Sucrose buffer, 4 mM ATPγS (15%)	20 mM HEPES pH 7.4, 40 mM NaCl, 5 mM DTT, 10 mM $MgCl_2$, 4 mM ATPγS, 15% (wt/vol) sucrose
Sucrose buffer, 4 mM ATPγS (45%)	20 mM HEPES pH 7.4, 40 mM NaCl, 5 mM DTT, 10 mM $MgCl_2$, 4 mM ATPγS, 45% (wt/vol) sucrose
Sucrose buffer, EQ mutants (15%)	20 mM HEPES pH 7.4, 40 mM NaCl, 4 mM DTT, 4 mM $MgCl_2$, 4 mM ATP, 15% (wt/vol) sucrose
Sucrose buffer, EQ mutants (30%)	20 mM HEPES pH 7.4, 40 mM NaCl, 4 mM DTT, 4 mM $MgCl_2$, 4 mM ATP, 30% (wt/vol) sucrose
20S activity assay solution	20 mM HEPES pH 7.4, 100micM Suc-LLVY-AMC, 4 mM ATP, 10 mM $MgCl_2$, 10% (vol/vol) glycerol

buffer	ingredients
Substrate assay solution	20 mM HEPES pH 7.4, 4 mM ATP, 10 mM $MgCl_2$, 10% (vol/vol) glycerol
Lysis buffer, substrate	100 mM NaCl, 50 mM Tris-HCl pH 7.4
Washing buffer, substrate	100 mM NaCl, 50 mM Tris-HCl pH 7.4, 0.05 M Imidazole
Elution buffer, substrate	20 mM HEPES pH 7.4, 40 mM NaCl, 10 mM $MgCl_2$, 0.3 M Imidazole
Gel filtration buffer,substrate	20 mM HEPES pH 7.4, 40 mM NaCl, 10 mM $MgCl_2$
MOPS running buffer	50 mM MOPS, 50 mM Tris Base, 0.1% (wt/vol) SDS, 1 mM EDTA, pH 7.7
TAE electrophoresis buffer	40 mM Tris Base, 20 mM acetic acid, 1 mM EDTA
Transfer buffer	25 mM Tris Base, 200 mM glycine, 20% (vol/vol) methanol

2.1.3 Cell Culture Media

Table 2.3: Cell culture media.

media	ingredients
YPD medium (liquid)	10 g Bacto yeast extract, 20 g Bacto peptone, 2 ml 1% (wt/vol) Adenine, 40% (wt/vol) glucose, 950 ml dH_2O
YPD medium (solid)	10 g Bacto yeast extract, 20 g Bacto peptone, 20 g Bacto agar, 2 ml 1% (wt/vol) adenine, 40% (wt/vol) glucose, 950 ml dH_2O
LB medium (liquid)	5 g Bacto yeast extract, 10 g Bacto tryptone, 5 g NaCl, 1000 ml dH_2O
LB medium (solid)	5 g Bacto yeast extract, 10 g Bacto tryptone, 5 g NaCl, 20 g Bacto agar, 1000 ml dH_2O
SOC medium (liquid)	20 g Tryptone, 5 g yeast extract, 4.8 g magnesium sulfate ($MgSO_4$), 3.603 g dextrose, 0.5 g NaCl, 0.186 g potassium chloride (KCl), 1000 ml

2.1.4 Yeast Strains

Table 2.4: Yeast strains

name	genotype
YYS40	*MATa ade2-1, ura3-1, his3-11, trp1-1, leu2-3,112, can1-100, rpn11::RPN11-3xFLAG-CYC1term-HIS3*
RTY1	*MATa his3-δ200 leu2-3,112 ura3-52 lys2-801 trp1-1 (alias MHY500)*
RTY432	*MATa his3-δ200 leu2-3,112 ura3-52 lys2-801 trp1-1 RPN5-6xGly-3xFLAG:hphMX4 rpt3δ::HIS3 [YCplac33-RPT3]*
RTY1168	*MATa his3-δ200 leu2-3,112 ura3-52 lys2-801 trp1-1 rpt1δ::HIS3 [pFL44-RPT1]*
RTY1171	*MATa his3-δ200 leu2-3,112 ura3-52 lys2-801 trp1-1 rpt4δ::HIS3 [YCplac33-RPT4]*
RTY1173	*MATa his3-δ200 leu2-3,112 ura3-52 lys2-801 trp1-1 rpt6δ::HIS3 [YCplac33-RPT6]*
RTY1179	*MATα his3-δ200 leu2-3,112 ura3-52 lys2-801 trp1-1 rpt6-δ1:natMX4*
RTY1301	*MATα his3-δ200 leu2-3,112 ura3-52 lys2-801 trp1-1 rpn6δ::natMX4 rpt6δ::HIS3 [pRS316-RPN6; YCplac33-RPT6]*
RTY1321	*MATa his3-δ200 leu2-3,112 ura3-52 lys2-801 trp1-1 rpt2δ::HIS3 [pRS316-RPT2]*
RTY1372	*MATa his3-δ200 leu2-3,112 ura3-52 lys2-801 trp1-1 rpn7δ::natMX4 rpt2δ::HIS3 [pRS316-RPN7; pRS316-RPT2]*
RTY1504	*MATa his3-δ200 leu2-3,112 ura3-52 lys2-801 trp1-1 rpt3δ::HIS3 [YCplac33-RPT3]*
RTY1506	*MATa his3-δ200 leu2-3,112 ura3-52 lys2-801 trp1-1 rpt5δ::HIS3 [YCplac33-RPT5]*
RTY1664	*MATa his3-δ200 leu2-3,112 ura3-52 lys2-801 trp1-1 rpt1-δ1:kanMX6*
RTY2013	*MATa his3-δ200 leu2-3,112 ura3-52 lys2-801 trp1-1 RPN5-6xGly-3xFLAG:hphMX4 rpt6δ::HIS3 [YCplac33-RPT6]*
RTY2033	*MATa his3-δ200 leu2-3,112 ura3-52 lys2-801 trp1-1 RPN5-6xGly-3xFLAG:hphMX4 rpt2δ::HIS3 [pRS316-RPT2]*
RTY2091	*MATα his3-δ200 leu2-3,112 ura3-52 lys2-801 trp1-1 RPN7(D123C)-6xGly-V5:kanMX6*

name	genotype
RTY2099	*MATa his3-δ200 leu2-3,112 ura3-52 lys2-801 trp1-1 RPT2(R407C):natMX4*
RTY2112	*MATa his3-δ200 leu2-3,112 ura3-52 lys2-801 trp1-1 RPN7(D123C)-6xGly-V5:kanMX6 RPT2(R407C):natMX4*
RTY2123	*MATa his3-δ200 leu2-3,112 ura3-52 lys2-801 trp1-1 rpt1-δ1:kanMX6 rpt6-δ1:natMX4*
RTY2166	*MATa his3-δ200 leu2-3,112 ura3-52 lys2-801 trp1-1 pre8δ::HIS3 pre9δ::natMX4 [pRS316-PRE8]*
RTY2135	*MATa his3-δ200 leu2-3,112 ura3-52 lys2-801 trp1-1 RPN7(D123C)-6xGly-V5:kanMX6 RPT2(R407C):natMX4 rpt3δ::HIS3 [YCplac33-RPT3]*
RTY2137	*MATa his3-δ200 leu2-3,112 ura3-52 lys2-801 trp1-1 RPN7(D123C)-6xGly-V5:kanMX6 RPT2(R407C):natMX4 rpt6δ::HIS3 [YCplac33-RPT6]*

2.1.5 Plasmids

Table 2.5: Plasmids

name	genotype
pRT357	pRS314-RPT1
pRT364	YCplac111-RPT3
pRT702	YCplac111-RPT2
pRT1122	pET42b-6His-Cys-rpn12(C23S,D265A)
pRT1408	pRS315-RPT5
pRT1409	pRS314-rpt1(E310Q)
pRT1410	YCplac111-rpt2(E283Q)
pRT1411	YCplac111-rpt3(E273Q)
pRT1413	pRS315-rpt5(E282Q)
pRT1425	pRS314-HA-RPN6
pRT1496	YCplac111-RPT6
pRT1497	YCplac111-rpt6(E249Q)
pRT1528	YCplac111-RPT4
pRT1529	YCplac111-rpt4(E283Q)
pRT1780	pRS314-HA-RPN6(T203C)
pRT1783	YCplac111-RPT2(R407C)
pRT1784	YCplac111-RPT6(G387C)
pRT1834	YCplac111-rpt2(E283Q, R407C)
pES1	pET28a-5Ub-DHFR-UR-His

2.1.6 Software

Table 2.6: Software

software	source
Adobe Illustrator CS6	Adobe
Latitude S Software	Gatan
MATLAB	MathWorks
NAMD	(Phillips et al., 2005)
QwikMD	(Ribeiro et al., 2016)
RELION	(Scheres, 2012)
SeqBuilder	DNASTAR
SerialEM	(Mastronarde, 2005)
TOM toolbox	(Nickell et al., 2005)

software	source
UCSF CHIMERA	(Pettersen et al., 2004)
VMD	(Humphrey et al., 1996)

2.2 Methods

2.2.1 Molecular Cloning

2.2.1.1 Polymerase Chain Reaction (PCR)

Components for deoxyribonucleic acid (DNA) amplification as listed below were mixed and used for DNA amplification in a Bio-Rad thermal cycler.

Table 2.7: PCR components

component	amount
up to 50 μl	Nuclease-free water
10 μl	5X Phusion HF Buffer
variable	template DNA (approximately 1 µg DNA)
2.5 μl	10 µM deoxynucleotides
2.5 μl	10 µM upstream primer
2.5 μl	10 µM downstream primer
0.5 μl	Phusion DNA Polymerase

The general Polymerase Chain Reaction (PCR) program as described was used (Table 2.8). The DNA was resolved using a 1% (w/v) agarose gel in 1X TAE buffer and SYBR™ Safe DNA gel stain with a 1 kb DNA marker. Gel extraction, washing and elution steps were followed according to the QIAGEN Gel extraction kit.

Table 2.8: PCR program

step	temperature	time
initial denaturation	98°	0:30 min
35 cycles	98°	0:30 min
	55°	0:30 min
	72°	0:30 min per kb
final extension	72°	5:00 min
hold	10°	forever

2.2.1.2 Restriction Digestion

Restriction digests were performed using FastDigest restrictions enzymes from Thermo Fisher Scientific. The reaction mixture was set up and incubated at 37 °C for five minutes. The DNA was then directly resolved using a 1% (wt/vol) agarose gel in 1X TAE buffer. Gel extraction, washing and elution steps were followed according to the QIAGEN Gel extraction kit.

2.2.1.3 In-Fusion Cloning kit

The calculated amount of linearized vector and purified PCR fragment were mixed according to recommendations calculated with the In-Fusion online tool. The reaction with the In-Fusion HD enzyme premix was then incubated for 15 minutes at 50 °C and placed on ice after the reaction.

2.2.1.4 Transformation of Competent Cells

1 μl of the previously described ligation reaction was added to 10 μl competent *E. coli* cells, which were stored at -80 °C and thawed on ice. After incubation for 15 minutes on ice, the *E. coli* cells were heat shocked at 42 °C for 15 seconds. After heat shock, 100 μl of SOC medium was added to the cells and the cells were incubated in the shaker at 37 °C for 60 minutes. The entire volume was then plated on LB plates with the correct antibiotic and incubated overnight at 37 °C. In general DH5α and Top10 cells were used for plasmid amplification. BL21 cells were used for protein expression and purification.

2.2.1.5 Small-Scale Plasmid DNA Preparation

Overnight *E. coli* cultures were transferred to 1.5 ml Eppendorf tubes and spun down at >8200 rpm for 10 minutes at 4 °C. The supernatant was removed and the pellet was resuspended with buffer from the QIAprep Spin Miniprep Kit. Lysis, washing and elution steps were followed according to the QIAGEN Miniprep kit.

2.2.1.6 Photometric Measurement of DNA Concentration

An Implen NanoPhotometer was used to measure DNA concentration. The optical absorption was measured at 260 nm and the DNA concentration of the sample was calculated.

2.2.1.7 DNA Sequence Analysis

The DNA was sent out for sequencing to the DNA Analysis Facility at the Max Planck Institute of Biochemistry. The resulting sequence data was compared with the desired DNA construct using the DNA SeqBuilder sequence analysis program.

2.2.2 Protein Purification

2.2.2.1 *E. coli* Cell Culture

The required antibiotic, stored as a 1000X aliquot, was added to a sterile culture tube filled with lysogeny broth (LB) medium. Bacterial colonies were picked off of LB-agar plates and placed in the culture tube. The pET28a vector expressing the gene of the desired protein was grown in LB media containing 25 μg/ml of kanamycin. For proteasome substrate expression, inoculated BL21 cell cultures containing the desired plasmid were grown at 37 °C in 5 ml LB media overnight and in the morning diluted into one liter cultures. The cells were further grown for roughly three hours. When the optical density (OD) of cells reached 0.6, the cells were induced with 0.3 mM IPTG. The induced cells were then grown overnight (18-20 hours) at room temperature. The cells were harvested at 4250 x g for 15 minutes and directly frozen in liquid nitrogen.

2.2.2.2 DHFR Substrate Purification

The frozen *E. coli* cell pellet was thawed and dissolved in lysis buffer. 5 ml of lysis buffer per gram of wet cell pellet was used. Accordingly, protease inhibitor cocktail was added and the resuspended cells were sonicated using a Branson Ultrasonics™ Sonifier S-250A. The disrupted cells were centrifuged at 15000 rpm with a SS36 rotor in a Beckman centrifuge. The supernatant was transferred to a falcon tube and was then applied onto nickel-nitrilotriacetic acid (Ni-NTA) fast flow beads and incubated for 2 hours at 4 °C. The Ni-NTA column was then washed with 4 column volumes of lysis buffer and then with two column volumes of washing buffer. The targeted protein was eluted with elution buffer. The eluted protein was concentrated to a volume of 1 ml using an Amicon MWCO 30,000 concentrator. The concentrated substrate was further purified using a NGC™ Chromatography system from Bio-Rad. A Superdex 75 10/300 GL column equilibrated with gel filtration buffer was used. All buffers were degassed prior use with the NGC™ machine.

2.2.2.3 Yeast Cell Culture

S. cerevisiae strains were struck out onto yeast extract peptone dextrose (YPD) plates and grown for approximately 48 hours at 30 °C. For 26S proteasome purification, a strain with a 3xFLAG-tagged Rpn11 was used. One single colony was picked and inoculated in 5 ml of YPD. The culture was grown overnight at 30 °C in a shaker and the next day the cell culture was diluted into a 100 ml YPD culture and grown at 30 °C with shaking at 150 rpm for 8 hours. After 8 hours of growth, 25 ml of culture were distributed into 1000 ml YPD cultures in a baffled Erlenmeyer flask. The cells were then incubated for a total of 60 hours on a horizontal shaker at 140 rpm at 30 °C. The cells were harvested using a Sorvall centrifuge equipped with a JA-10 rotor at 1,000 x g. After washing the cells with distilled water the cells were stored at -80 °C until further use.

2.2.2.4 26S Proteasome Purification

The frozen yeast pellet was resuspended in Buffer A at a ratio 1 g of cells to 1 ml of buffer. Cell disruption was carried out either with glass bead milling (Vibrogen-Zellmuehle Vi4; Edmund Buehler, Tuebingen) (a) or using a cell mill (b). (a) For glass bead milling, Zirkonia glass beads with diameter of 1.5 mm were mixed with the resuspended yeast pellet so that a viscous mixture of glass beads and yeast pellet was reached. The cells were then disrupted in two cycles of four minutes at 4 °C. After lysis, the resulting cell lysate was separated from the beads by centrifugation using an in house-made filter unit. (b) Alternatively the cells were lysed using a microfluidizer (Emulsiflex-C3; AVESTIN, Ottawa) at 4 °C. To separate the cell debris, the crude extract was centrifuged at 43,000 x g for 30 min at 4 °C. The pH of the crude extract was adjusted to pH 7.4 using Tris base and the cleared lysate was then incubated with anti-Flag M2 resin (Sigma) for 90 minutes at 4 °C. After the 90 minute incubation, the beads were washed with a total of 30 bead volume buffer. The bound protein was ultimately eluted using 200 μg/ml of 3xFLAG Peptide in Buffer A. The eluate was concentrated by centrifugation in Amicon spin columns (100 kDa molecular weight cutoff). To further purify the doubly capped proteasomes, the concentrated eluate was applied to a sucrose gradient, made using a Gradient Station ip (Biocomp), and centrifuged for 17 hours at 209,000 x g at 4 °C in a Beckman SW41 rotor. The sucrose gradient was fractionated into 300 μl fractions using the Gradient Station ip (Biocomp). All samples were stored at -80 °C after snap freezing in liquid nitrogen.

2.2.3 Analytical Methods

2.2.3.1 Determination of Protein Concentration using Bradford

For protein samples without SDS, a Bradford assay was performed using the Protein Assay reagent from Bio-Rad to determine the total protein concentration. The reaction was carried out in 1 ml of Bradford solution with 2 μl of sample protein. Bio-Rad bovine serum albumin (BSA) was used in four different dilutions – 2 μg/ml, 4 μg/ml, 6 μg/ml and 15 μg/ml - to establish a standard curve. The protein concentration of the samples was determined by measuring absorption at 595 nm with an Eppendorf BioPhotometer and then calculating the protein concentration from the standard curve.

2.2.3.2 Discontinuous SDS-Polyacrylamide Gel Electropheresis (SDS-PAGE)

10 μl of each sucrose gradient fraction were boiled in 3.33 μl NuPAGE LDS Sample Buffer (4X) at 95 °C for 5 min and loaded onto a precast 4-12% Bis-Tris SDS gel. Precision Plus Dual Color Protein Standard from Bio-Rad was used as a protein size marker. The gel was run for roughly 45 min at 200 V in 1X Tris/glycine electrophoresis buffer until the sample band reached the lower end of the gel. The gel was then washed for 10 minutes with water before it was stained using InstantBlue™ protein staining solution. After one hour of incubation the gel was washed again with water overnight and digitalized the next day.

2.2.3.3 Western Blotting

Proteins were transferred from the SDS-PAGE gel to a polyvinylidenfluoride (PVDF) membrane (Bio-Rad) by electroblotting. The PVDF membrane was incubated for approximately one minute in methanol and one minute in transfer buffer. Filter papers were soaked with transfer buffer before the transfer. The transfer sandwich was set up between the two metal plates of a BioRad semi-dry transfer apparatus and consisted of filter paper, PAGE gel, membrane, and filter paper. Each transfer was performed with a maximum voltage of 30 V at a constant amperage of 250 mA for 30 minutes. Then the membrane was blocked with a solution of 4% nonfat milk in TBS-T for one hour or overnight at 4 °C. After blocking, the membrane was incubated with ubiquitin antibody (Santa Cruz) for one hour, followed by three washing steps with TBS-T each for 10 minutes. Finally, the membrane was developed using the ECL™ western blotting reagent (Merck), which was applied to the membrane according to the manufacturer instructions.

2.2.3.4 20S Proteasome Activity Assay

The 20S proteolytic activity of each fraction from the sucrose gradient was screened using the substrate Suc-LLVY-AMC. The proteasome cleaves after the Tyr residue of the substrate and releases the AMC from the peptide, which is excited at a wavelength of 360 nm. The emission signal of the released AMC is used to quantify proteolytic cleavage. 10 μl of sample were mixed with 90 μl of 20S activity assay solution in a 96-well plate and the change in fluorescence (FU) was monitored for 60 min using the FLUOstar Optima (BMG Labtech). The slope (FU/sec), which corresponds to 20S activity, was calculated within the linear part of the progress curve.

2.2.3.5 26S Proteasome Analytic Digest

200 pmol of substrate and 1 pmol of 26S proteasome purified in ATP or ATPγS background was mixed in a total volume of 20 μl substrate assay buffer. If 26S proteasome purified in ATPγS was used no ATP was added to the substrate assay buffer. Depending on the experimental setup a specific inhibitor – MG132 or 1,10-phenantrholine (*o*PA) - was additionally added to the buffer. 26S proteasome was incubated for five minutes in buffer at room temperature before adding substrate. At specific time points, the sample was heat shocked for one minute. The analytic digest was followed by SDS-PAGE and western blotting with an antibody against ubiquitin (Santa Cruz).

2.2.4 Electron Microscopy

2.2.4.1 Sample Preparation

2.2.4.1.1 Negative Stain 5 μl of sample with a final concentration of approximately 100 μg/ml was prepared and pipetted onto a 30 seconds glow-discharged carbon coated copper-rhodium grid from Pyser, 400 x 400 mesh. After one minute, the solution was removed and the grid was washed twice with 5 μl dH$_2$O before it was stained for one minute with 5 μl uranylacetate (2 % in dH$_2$O wt/vol). As the final step, the stain was removed and the grid was dried at room temperature.

For data set acquisition the 30 seconds glow-discharged grids were pre-treated to overcome preferred orientation of the 26S particles. Therefore 5 μl of 0.1% poly-L-lysine hydrobromide was added to a grid and the grid was washed after 60 seconds two times with 5 μl of dH$_2$O. The grids were then dried for 10 minutes at room temperature before sample was applied and negatively stained as described above.

2.2.4.1.2 Plunge Freezing Carbon coated copper grids (Lacey grids) were glow discharged for 15 seconds. 4 μl sample was pipetted onto the grids and incubated for 30 seconds. The excess sample solution was blotted using a filter paper. To remove sucrose in the sample, the grid was washed with 5 μl of H2O and then rapidly plunge-frozen into liquid ethane/propane cooled by liquid nitrogen using a manual plunger. All grids were stored in liquid nitrogen until further processing.

2.2.4.2 Data Acquisition

2.2.4.2.1 Negative Stain Data Acquisition A Philips CM200/FEG electron microscope was used for acquisition of micrographs of negatively stained grids. Acquisition was carried out at 160 kV acceleration voltage with a TVIPS CCD camera (4096 x 4096 pixel) at a pixel size of 2.16 Å at specimen level. The nominal defocus varied from 2.5 to 3 μm.

2.2.4.2.2 Cryo-EM Data Acquisition Data acquisition was performed with an FEI Titan Krios electron microscope at an acceleration voltage of 300 kV. Data sets were collected with a K2 camera using the program Latitude software (Gatan, Inc.). Movies were acquired at a pixel size of 1.38 Å at specimen level. A total dose of roughly 35 electrons was distributed over 33 frames. The nominal defocus range of the acquisition varied from 1.8 to 3 μm.

2.2.4.3 Image Processing

All movie frames were aligned translationally and summed with MotionCor2 (Zheng et al., 2017). During frame alignment, recorded movies were subjected to motion correction. The CTF was estimated using CTFFIND3 (Rohou and Grigorieff, 2015) and micrographs with a CTF fit score below 0.05 and a defocus outside the range of 0.8 to 3.5 μm were discarded. Additionally because of the high number of micrographs from the 2 mM ATPγS and 4 mM ATPγS samples, micrographs with an estimated resolution over 4.5 Å were also discarded.

2.2.4.4 Single particle analysis

Single particle processing was performed following the procedure described by (Aufderheide et al., 2015; Schweitzer et al., 2016) (Fig. 2.1). In the first step, 26S proteasomes were picked automatically using the TOM toolbox (Beck et al., 2012). Hereby 26S proteasome particles are found by cross-correlation analysis of template projections. False positive hits were then removed by iterative 2D classification. Further proteasome particles were extracted using a box size of 384 x 384 pixel using the RELION software package (Scheres, 2012, 2016), which is the software package used for all further single particle analysis steps. For higher purity the extracted particles were iteratively reference-free 2D classified. Only 2D classes containing particles with a complete 26S were retained.

Table 2.9: SPA Overview

data set	mrc stacks	s1	s2	s3	s4	s5	s6	s7
ATP 4 mM	4668	41741	28911					
substrate	5875	8330	40311					
*o*PA	7343	56871	14699					86826
*o*PA, substrate	7452							51400
ATPγS 0.5 mM	11679	52560		130175	79136			
ATPγS 2 mM	21738	58149		67441	351984	146519		
ATPγS 4 mM	43128			224838	158902			
Rpt2 EQ	14892	338640			90848	47919		
Rpt3 EQ	15810	460457					184988	
Rpt6 EQ	16549	157941			65980	27361		

The amount of analyzed mrc stacks per data set and classified pseudo-sc26S are listed

The final star files containing all 26S particles were subjected to 3D reconstruction and classification. Each data set was reconstructed using a down-filtered 3D reference of the 26S proteasome.

Pseudo singly capped 26S particles (pseudo-sc26S) were generated using the resulting angles of the reconstruction as described in (Unverdorben et al., 2014). All pseudo-sc26S of one data set were then classified using a soft-edged mask focused on the RP. All previously assigned angles were kept constant during classification. Using the University of California at San Francisco (UCSF) chimera fit-in map (Pettersen et al., 2004) the previously identified proteasome states s1, s2, s3 and s4 were compared to the 3D class averages (Table 2.9) (Unverdorben et al., 2014; Wehmer et al., 2017).

Classified particles were combined into each state and refined using a soft-edged mask containing the RP, alpha-ring and beta-ring with a local angular search around the initial angles from the refinement of the polished particles. The resulting density was subjected to post-processing in RELION for resolution determination and B-factor sharpening. The resolution of the resulting final reconstruction was assessed by Fourier Shell Correlation (FSC 0.143) using the gold-standard method as described in (Chen et al., 2013).

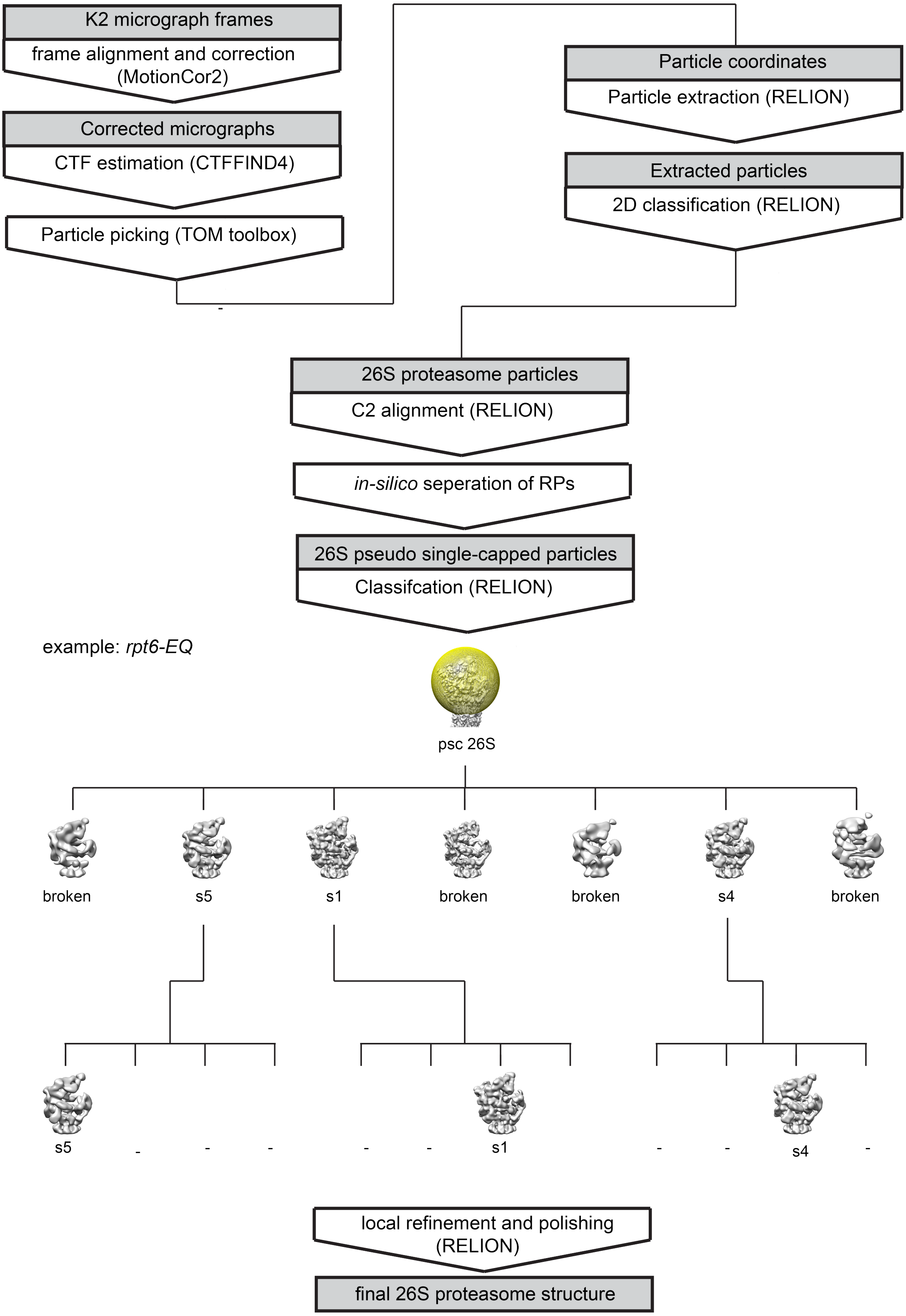
K2 micrograph frames
frame alignment and correction (MotionCor2)
Corrected micrographs
CTF estimation (CTFFIND4)
Particle picking (TOM toolbox)
-
Particle coordinates
Particle extraction (RELION)
Extracted particles
2D classification (RELION)
26S proteasome particles
C2 alignment (RELION)
in-silico seperation of RPs
26S pseudo single-capped particles
Classifcation (RELION)
example: *rpt6-EQ*
psc 26S
broken
s5
s1
broken
broken
s4
broken
s5
-
-
-
-
-
s1
-
-
s4
-
local refinement and polishing (RELION)
final 26S proteasome structure

Figure 2.1: **SPA workflow.** The typical SPA workflow for a 26S proteasome data set. As example the 3D classification rounds of the *rpt6-EQ* data set are shown. Figure adapted with permission from (Eisele et al., 2018).

2.2.4.5 Model-building and analysis

Atomic models were generated by employing an optimized integrative modeling approach based on the workflow used to obtain the previous structural model of the human (Schweitzer et al., 2016), yeast (Wehmer et al., 2017), and rat (Guo et al., 2018) proteasome. The utilized modeling approach combines molecular dynamics flexible fitting (MDFF) (Trabuco et al., 2009) with monte carlo backbone and sidechain rotamere search algorithm following the strategy described by Goh and colleagues (Goh et al., 2016). MDFF simulations were prepared using QwikMD (Ribeiro et al., 2016), analyzed with VMD (Humphrey et al., 1996), and carried out with NAMD (Phillips et al., 2005). The higher resolution densities of s3 and s4 were used to furniture missing unresolved segments of the previous models of s3 and s4 (Wehmer et al., 2017) and to further refine the model to reflect the higher resolution of the densities. The s5 model was created based on a previous s2 model and the s6 model based on the refined s3 model.

Chapter 3

Results

In this thesis, I address the impact of nucleotide binding, nucleotide hydrolysis and substrate binding on the structure of the proteasome using nucleotide analogs, ATPase mutants and a model substrate. I report not-yet identified conformational states and determined activated proteasome structures at high resolution, leading us to understand the gate opening mechanism and the ATPase cycle in more detail. A portion of the results were published in a peer-reviewed article (Eisele et al., 2018) and are used as the basis for the next chapters. The publication was an interdisciplinary effort with contributions of co-authors as stated in the article. In particular, the atomic model building was mainly carried out by Till Rudack and the biochemical experiments regarding the Rpt and gate mutants were done by Randi Reed and Robert J. Tomko.

3.1 Biochemical preparation

3.1.1 Purification of the 26S Proteasome

The 26S proteasome was purified from *S. cerevisiae* by affinity purification via a 3xFLAG-tagged Rpn11, followed by a sucrose gradient purification (described in 2.2.2.4). The sucrose gradient was eluted in 300 μl fractions and each fraction was checked for its concentration, activity and protein composition, as resolved by SDS-PAGE. The wild type 26S proteasome sample purified under 4 mM ATP condition had the highest concentration and activity between fractions 21-26 with a range of concentration range between 1.1 mg/ml for fraction 26 to 1.4 mg/ml for fraction 22. SDS-PAGE analysis showed the presence of the 26S proteasome holocomplex with the largest subunits Rpn1 (109.49 kDA), Rpn2 (104.23 kDA), the complete RP followed by subunits of the CP (Fig. 3.1A). The sample was further checked by negative stain in which doubly capped, singly capped and some some CP were visible (Fig. 3.1B).

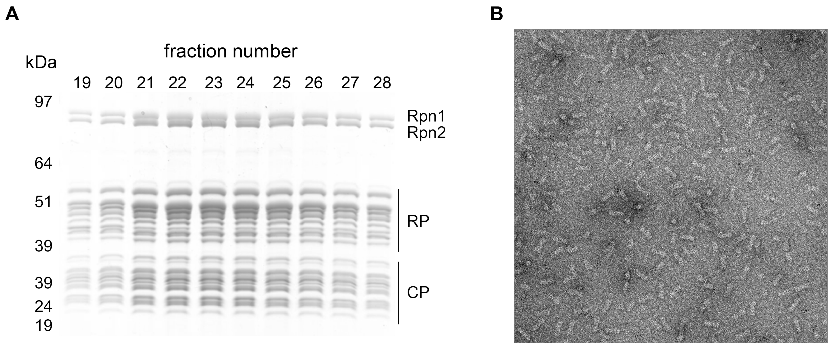

Figure 3.1: **Purification of 26S Proteasome.** (A) SDS gel of fractions of FLAG-tag affinity and sucrose gradient purified proteasome. (B) Negative stain image of a 26S proteasome sample with a high amount of doubly capped, and some singly capped proteasomes, along with some CP.

3.1.2 Preparation of a Model Substrate of the 26S Proteasome

Substrates of the proteasome are usually modified by a polyUb chain (Finley et al., 2012). Biochemical analysis revealed that the substrate must also contain an unstructured region that can serve as an initiation region for protein unfolding (Takeuchi et al., 2007; Prakash et al., 2009; Inobe et al., 2011). To gain additional insight into the mechanism of substrate recognition by the proteasome and the influence of substrate binding and processing on the state landscape, I designed a model substrate, further cloned and purified for structural studies.

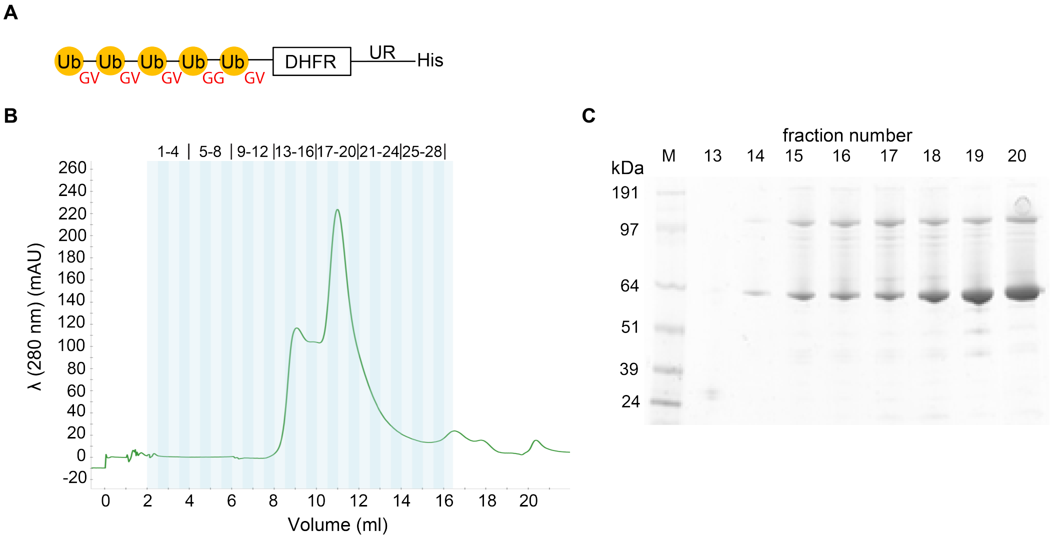

Figure 3.2: **Design and purification of a model substrate.** (A) Schematic over view of the designed model substrate. The substrate contains a linear penta-ubiquitin chain at the N-terminus, a folded DHFR domain and an unstructured region with a 6xHis tag at the C-terminus. (B) Gel filtration profile of the purified model substrate (C) with an SDS gel of fractions 13-20.

Following the research of the Matouschek group and others (Takeuchi et al., 2007; Prakash et al., 2009; Inobe et al., 2011), the substrate was constructed to consist of a ubiquitin chain with five linear ubiquitins, a structured protein domain of dihydrofolate reductase (DHFR) and an unstructured region of 30 amino acids. Several steps of cloning were taken to produce a model substrate with a linear ubiquitin chain (Fig. 3.2A). Using a ubiquitin template and a starting construct of monoubiquitinated DHFR, four further ubiquitin sequences were integrated to form a linear penta-ubiquitin chain. As the inherent Gly-Gly C-terminal sequence of ubiquitin is cleaved by deubiquitinating enzymes, the Gly-Gly sequence was substituted to Gly-Val to stabilize the linkers between the ubiquitins. Only the fourth ubiquitin consisted of a Gly-Gly linker, making it available for cleavage by deubiquitinating enzymes at this site. Moreover, an unstructured region of 30 amino acids was integrated downstream of DHFR (Fig. 3.2A). The model substrate was then expressed and purified through a C-terminal 6xHis tag, followed by gel filtration (Fig. 3.2B, C). Degradation assays of the substrate with purified 26S proteasome showed substrate processing by the proteasome. The band of around 35 kDa corresponds to either monoubiquitinated DHFR (~33 kDa) or to a tetra ubiquitin chain (~34 kDa), indicating that the substrate is clearly deubiquitinated but may not be degraded (Fig. 3.3A).

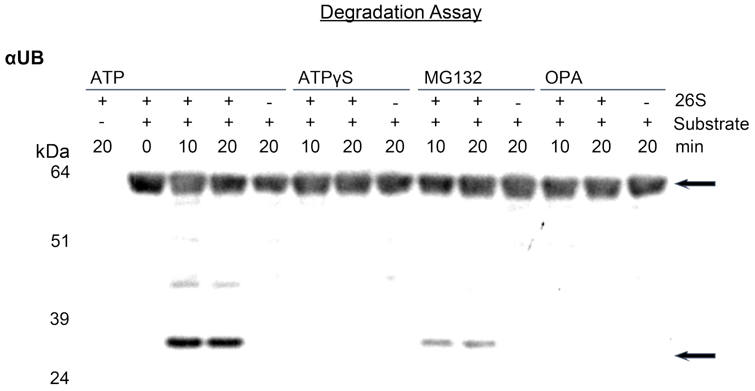
Degradation Assay
αUB
ATP
ATPγS
MG132
OPA
+ + + + - + + - + + - + + - 26S
- + + + + + + + + + + + + + Substrate
kDa 20 0 10 20 20 10 20 20 10 20 20 10 20 20 min
64
51
39
24

Figure 3.3: **Model substrate assays.** Degradation assay with DHFR model substrate and 26S proteasome. The degradation was carried out with either proteasome purified with 4 mM ATP or 2 mM ATPγS. The proteasome inhibitor MG132 or the Rpn11 inhibitor *o*PA were additionally added in the two indicated reactions to 26S proteasome purified with 4 mM ATP.

Deubiquitination of the substrate can additionally be confirmed by addition of an Rpn11 inhibitor, the chelator *o*PA (Verma et al., 2002). This resulted in no processing of the substrate. Substrate processing can also be inhibited by using already activated proteasome, which was purified in the background of the nucleotide analog ATPγS. Addition of MG132 had a small inhibitory effect on the results of the degradation assay. Overall this result indicates that Rpn11 deubiquitinates the linear ubiquitin chain of the model substrate and maybe releases the substrate from the 26S holocomplex. Substrate might be hereby not degraded but rather quickly deubiquitinated.

3.2 26S Proteasome in the Background of ATPγS

Previous studies showed that different nucleotides and nucleotide analogs influence the conformational states of the proteasome (Wehmer et al., 2017). PAN has two high and two low affinity sites for ATP (Kd ~0.5 μM and ~113 μM, respectively) (Smith et al., 2011). Because of its close homology to the 26S proteasome a similar biphasic nucleotide binding could also be suggested for the ATPase of the *S. cerevisiae* proteasome (Smith et al., 2011). Increasing the nucleotide concentration therefore might have an impact on the conformational state of the eukaryotic proteasome and is thus interesting to investigate. 26S proteasome was purified with increasing concentrations of ATPγS. ATPγS resembles most closely ATP, but is hydrolyzed more slowly, which may prevent conformational shifting. During the sucrose gradient, ATP was substituted by different concentrations of ATPγS: 0.5 mM ATPγS, 2 mM ATPγS or 4 mM ATPγS. EM datasets of each ATPγS sample were acquired at a pixel size of 1.34 Å with a K2 camera at 300 kV on a Titan Krios. Micrographs were sorted, particles were picked and finally classified. The single particle analysis revealed a specific class distribution for each sample (Fig. 3.4A).

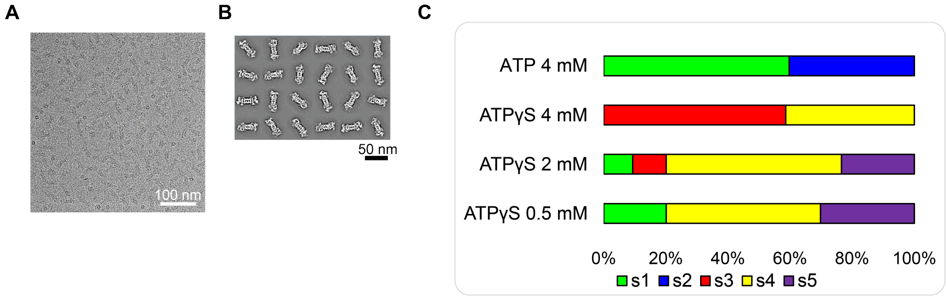

Figure 3.4: **ATPγS concentration dependent 26S state landscape.** (A) A typical micrograph, which resulted from aligning and dose weighting of the acquired 33 frames. (B) 26S proteasome particles were 2D classified into 2D classes containing mostly 26S proteasome particles. (C) 26S proteasome was purified with different concentrations of ATPγS, acquired by cryoEM and finally classified to different states. The control data set was purified with 4 mM ATP. Figure adapted with permission from (Eisele et al., 2018).

In the 4 mM ATPγS sample only two states, ~59% s3 state and ~41% s4 state were observed, while the s1 ground state was not observed. In the 2mM ATPγS sample, the two most abundant states were ~56% of s4 state and ~23% of a yet unassigned state, s5. The two least abundant states were s1 and s3, with ~9% and ~11%, respectively. The population of s1 state in the 0.5 mM ATPγS was ~20% and the s5 state and the s4 state were ~7% and 50%, respectively. Overall, an increase in ATPγS concentration decreased the amount of ground state proteasome and instead increased the amount of activated proteasome states (s3, s4).

Part of the data was acquired in the presence of a model substrate, as discussed above. The substrate was on the one hand not visible in the density, hinting at a very flexible or weak binding but it also did not further advance the state distribution, likely due to the strong influence of ATPγS on proteasome conformation (Fig. 3.5).

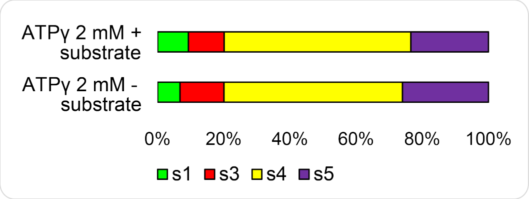

Figure 3.5: **Model substrate influences ATPγS purified 26S proteasomes.** The model substrate was added to the ATPγS purified sample and additionally acquired by cryoEM. All particles were classified to different states. Figure adapted with permission from (Eisele et al., 2018).

3.2.1 Analysis of the s5 State

The nucleotide analog results not only confirmed that the concentration of ATPγS can influence the equilibrium of the state landscape, but it was also possible to stabilize the s4 state in a higher abundance, and resolve the yet unassigned s5 state. In the final step of analyzing the EM data, particles of each state were combined, refined and B-factor polished.

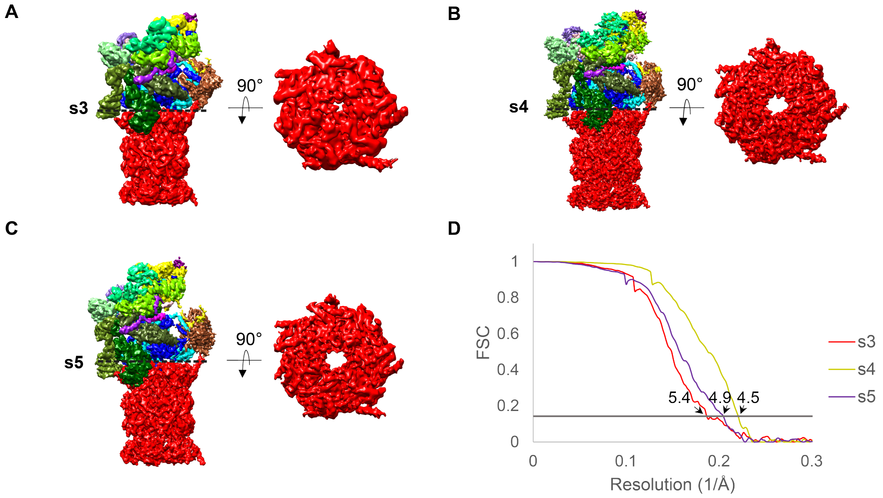

Figure 3.6: **Cryo-EM reconstructions of the s3, s4 and s5 states.** Reconstruction of particles of the s3 state (A), s4 (B) and s5 state (C). (D) FSC curves of each state, which were reconstructed, refined and then polished. Figure adapted with permission from (Eisele et al., 2018).

EM maps of the s3, s4 and s5 states achieved global resolutions of 5.4 Å, 4.5 Å and 4.9 Å, respectively (Fig. 3.6). The analysis of the new state, s5, started by looking for key features in the density maps of known states. This helped to define the starting models for atomic modeling, with which analysis of elements, such as the 20S gate and the AAA+ ATPase, would be more accurate. This analysis of the EM map of the new s5 state revealed a very close resemblance to s2. For example the distance between the N-termini of Rpn5 and Rpn6 in the s5 state is similar to the s2 state and the small AAA+ ATPase domain of Rpt4 is found to contact the $\alpha 7$ subunit of the CP, as seen in the s1 and s2 states. The close resemblance of s2 and s5 could be confirmed by using the fit in function of Chimera using the recently published PDB model of the s2 state (Wehmer et al., 2017).

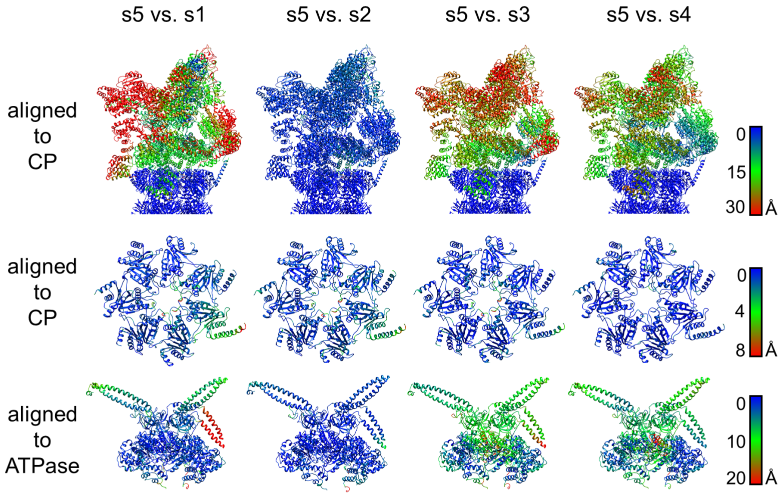

Figure 3.7: **RMSD comparison of s5 with the other states.** (A) RMSD comparison of the model of the s5 state with the other four states (s1-s4). The range goes from blue, to green to red, where blue represents the smallest differences and red the largest differences between both models of the specific residue. Figure adapted with permission from (Eisele et al., 2018).

For a better comparison and analysis opportunities atomic models were created using a combined Rosetta and molecular dynamics flexible fitting approach (Lindert and McCammon, 2015). The s5 atomic model was generated using s2 (PDB: 5mpa and 5mpe) as a starting model. The atomic models of s3 and s4 were refined using the better resolved s3 and s4 maps and the published s3 (PDB: 5mpb) and s4 models (PDB: 5mpc) as a starting point.

To show the high resemblance of s5 to s2 at the model level, RMSD calculations of s5 compared to the other states were carried out (Fig. 3.7). For the RMSD calculations either the complete 26S was compared after alignment of the CP or the ATPases were compared after alignment of the ATPases. The RMSD comparison of the s5 structure confirmed the strong similarity to s2 (Fig. 3.7). The RMSD value when comparing the 26S structures between s2 and s5 is 4.02 Å, which is significantly lower than the RMSD values in the comparison with the other conformations, for example compared to the next highest value of 16.36 Å between s4 and s5.

Only several subunits exhibit a shift of more than 3 Å when comparing s5 to s2. For example, Rpn2 is shifted by ∼4 Å (Fig. 3.8) and Rpt6 shows the most significant difference, with a shift of ∼6 Å in the direction of the CP. This brings Rpt6 closer to the CP causing the C-terminus

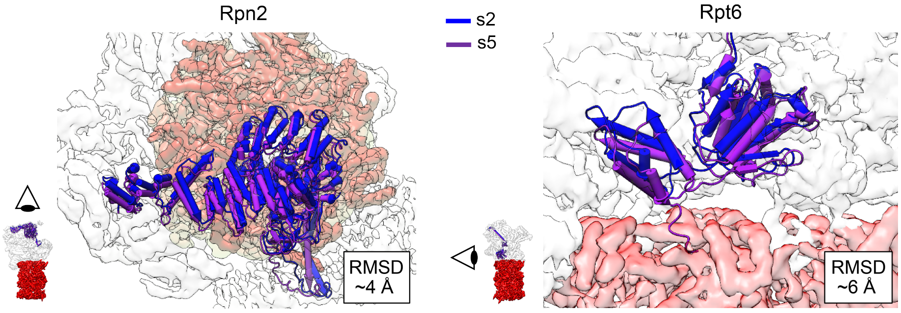

Figure 3.8: **Subunit differences between s2 and s5.** An overlay of the subunit Rpn2 in the s2 and s5 state in the left panel, and the right panel shows how the Rpn2 and Rpt6 subunits shift between both states. The s2 state is shown in blue, s5 in purple. Rpn2 is seen from a top view, Rpt6 from a side view. Figure adapted with permission from (Eisele et al., 2018).

of Rpt6 to contact the α subunits. Moreover, a missing density within the CP gate indicates that s5 is an open gate state. An insertion of the Rpt6 C-terminus was already reported in the 8 Å s4 structure and indeed might be connected to a gate opening mechanism.

3.3 26S Proteasome in the Background of ATPase Walker B EQ Mutants

The resolution of the proteasome EM reconstructions did not allow us to determine the nucleotide states of the ATPases in s2 and s5 thus making it difficult to understand if a different nucleotide occupation might be the trigger for the down shift of Rpt6. To assess the impact of individual ATP-binding events on proteasome conformational distribution, a genetic mutagenesis approach was used. Here the conserved glutamate of the Walker B motif was substituted to a glutamine in each ATPase subunit in yeast (*rpt-EQ*). The EQ mutation is a common mutation that prevents ATP hydrolysis by that particular Rpt subunit. The ATP-bound state is thereby enriched. The EQ mutations were systematically introduced into each ATPase subunit in yeast by the plasmid shuffle method. Each *rpt-EQ* mutant was then tested for its viability upon eviction of the plasmid bearing the wildtype *RPT* allele on 5-fluoroorotic acid (5-FOA) media (Fig. 3.9).

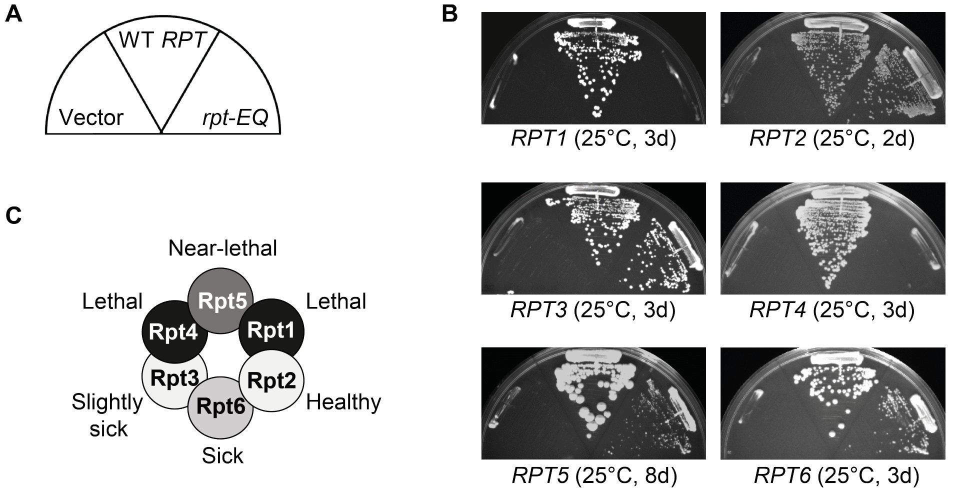

Figure 3.9: **Generating Walker B EQ mutants.** (A) Growth assay overview. Three vectors are compared for each Walker B EQ mutation. (B) A growth assay for each *rpt-EQ* was carried out to check the mutated cells for their viability. (C) Schematic overview of the ATPase ring and the viability of the inserted *rpt-EQ* mutant. The experiments were carried out by a collaborating lab. Figure adapted with permission from (Eisele et al., 2018).

Only four of the six *rpt-EQ* mutants were viable in yeast. The *rpt2-EQ* mutant grew best, followed by *rpt3-EQ* then *rpt6-EQ* and lastly the *rpt5-EQ* mutant, which had the largest growth defect. Because the cells did not grow in the *rpt1-EQ* and *rpt4-EQ* mutants and *rpt5-EQ* could not be cultured reliably, only *rpt2-EQ*, *rpt3-EQ* and *rpt6-EQ* were used in further studies.

3.3.1 Structural Analysis of the Walker B EQ Mutants

The three mutant proteasomes *rpt2-EQ*, *rpt3-EQ* and *rpt6-EQ* were purified in the presence of 4 mM ATP. Each sample was acquired by cryo-EM, the 26S proteasome particles were picked and finally classified to achieve a state distribution as described before (Fig. 3.10).

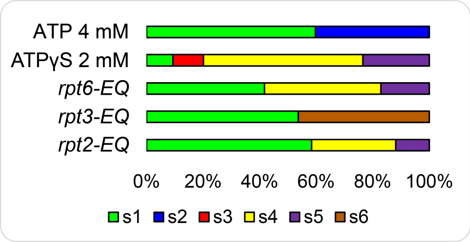

Figure 3.10: **The Walker B EQ proteasome conformational state landscape.** All three EQ mutants were purified and structurally analyzed with cryoEM. The resulting states are reported in the diagram. Figure adapted with permission from (Eisele et al., 2018).

Each EQ mutant resulted in a different distribution of 26S proteasome conformation. Similar to the ATPγS dataset, the s2 state, which accounts for ~40% of proteasomes purified in the ATP background, was absent in these three datasets. Instead, in the *rpt2-EQ* mutant, ~58% s1, ~30% s4 and ~12% s5 were found. The same conformational states with a different distribution were found in the *rpt6-EQ* mutant, with ~42% s1, ~41% s4 and ~17% s5, making it overall more a highly activated distribution with ~19% less s1 than in control samples.

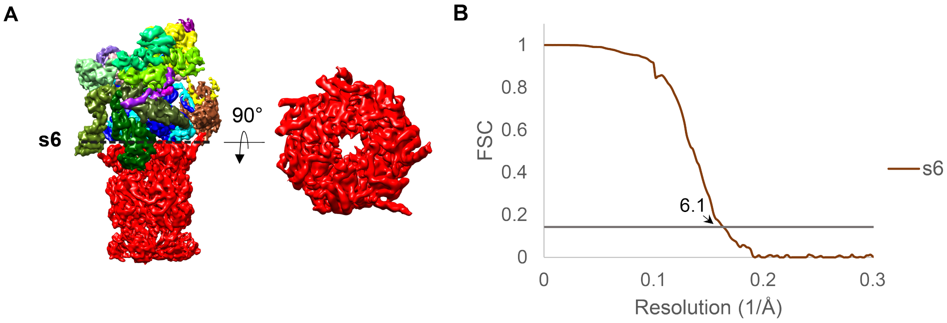

Figure 3.11: **Cryo-EM density of the s6 state.** (A) The particles of the newly found s6 state were refined and lead to a density with a resolution of 6.1 Å. (B) FSC curves of the s6 state reconstruction. Figure adapted with permission from (Eisele et al., 2018).

The *rpt3-EQ* decreased the amount of ground state (s1) 26S proteasome by ~6% to ~54%. The entire non-s1 population (~46%) was made up of a previously unidentified conformational state, which was termed s6. The particles of the s6 state were combined, and again refined and B-factor polished, resulting in an EM reconstruction at a resolution of 6.1 Å (Fig. 3.11). Overall, the RP of the s6 state resembles the s3 state most closely, which could be identified by the overall similar conformation and fitting of already identified atomic models of states s1-s5. For atomic modeling, as performed before, a combination of MDFF, monte carlo backbone and sidechain rotamere search algorithm was used to create an atomic model of s6 with the s3 model used as a starting model.

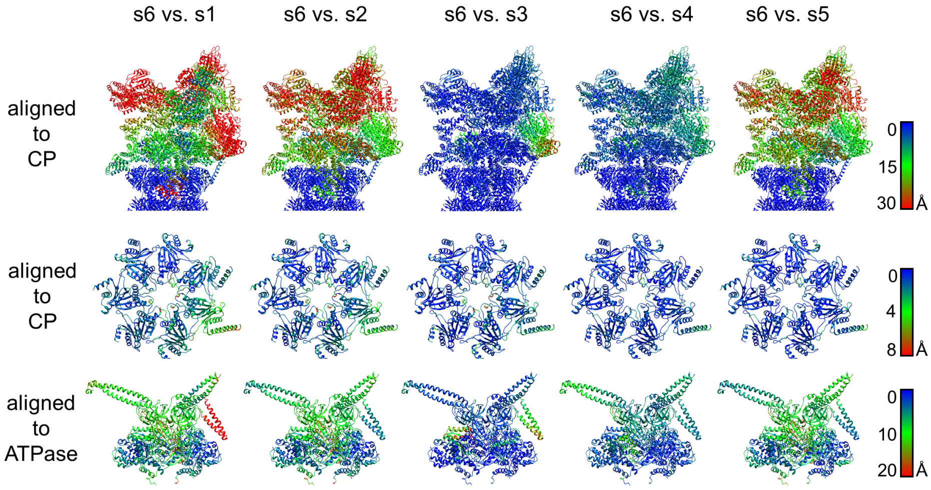

Figure 3.12: **RMSD comparison of s6 with the other states.** RMSD comparison of the model of the s6 state with the other five states (s1-s5). For comparison either the CP or the ATPase of the two models being compared was aligned. The range goes from blue, to green to red, where blue represents the smallest differences and red the largest differences between both models of the specific residue. Figure adapted with permission from (Eisele et al., 2018).

This model was further used for RMSD calculations (Fig. 3.12). Again the complete RP or gate was compared after aligning the CP of both particles, or the ATPase after aligning the ATPase. Several differences between s3 and s6 could be observed: As seen in s4, s5 and not in s3, the s6 state has no clear density within the central pore of the CP, indicating an open gate. Compared to the s3 state, the N-terminus of Rpn1 is stably docked on Rpt6 and Rpt2, as it can be observed in the s4 and s5 states. Differences can also be found between s3 and s6 in the ATPase with the largest differences appearing in Rpt4. In any event, the results of the Walker B mutant proteasomes together suggest that ATP binding by proteasomal ATPases disfavors the s2 state, and promotes the open-gate s4, s5, and s6 states.

3.4 26S Proteasome in the Presence of a Model Substrate

To gain insight into how the model substrate influences the 26S proteasome conformational landscape, SPA experiments with the model substrate were performed. First, purified 26S proteasome was incubated with the substrate on ice and then subsequently prepared for cryo-EM and finally acquired with a K2 camera using a 300 kV Titan Krios. Second, the 26S proteasome was incubated with the Rpn11 chelator *o*PA before adding the model substrate. And as a control, 26S proteasome was incubated with *o*PA alone and acquired by cryo-EM. All 26S proteasome particles were picked separately, and classified to the conformational states (Fig. 3.13).

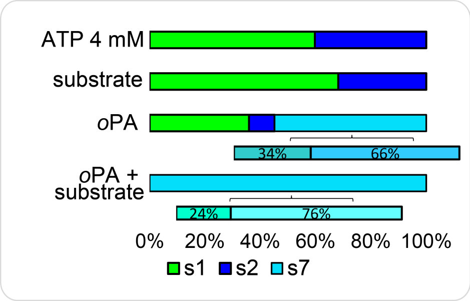

Figure 3.13: **Substrate and *o*PA dependent 26S proteasome state landscape.** 26S proteasome mixed with substrate, substrate and *o*PA was acquired by cryoEM and finally classified to different states.

However, the same distribution of classes as compared to the control proteasome, where the conformational distribution is ∼60% s1 and ∼40% s2, was also observed in the presence of model substrate. Conversely, *o*PA alone did influence the conformational landscape of the proteasome. Only ∼36% s1 and ∼9% s2 were observed with *o*PA alone and the remaining ∼55% of proteasomes could be allocated to particles of a yet unassigned state, which is termed s7. The particles in the s7 state contain structural heterogeneities and consist of at least of two different conformational states. However, these two classes were nearly identical and could not be clearly differentiated at the current resolution. Neither s1 nor s2 particles were observed in the dataset of the proteasome in the presence of both the substrate and *o*PA. Instead, the aforementioned s7 state was dominant in the dataset. Similar to the *o*PA alone dataset, the particles in the s7 state are heterogeneous, consisting of two sub-classes. These two classes may be slightly different from those identified in the *o*PA-dataset but further and more cryo-EM analysis is required to distinguish these states. For the sake of simplification, all particles are redirected into one new state, the s7 state. In earlier structural work (Matyskiela et al., 2013) the activated s3 state was reported using a combination of a different model substrate and 26S proteasome with an Rpn11 activity mutant. The s3 state seen in this previous study could not be observed in any of the data sets acquired with the DHFR model substrate.

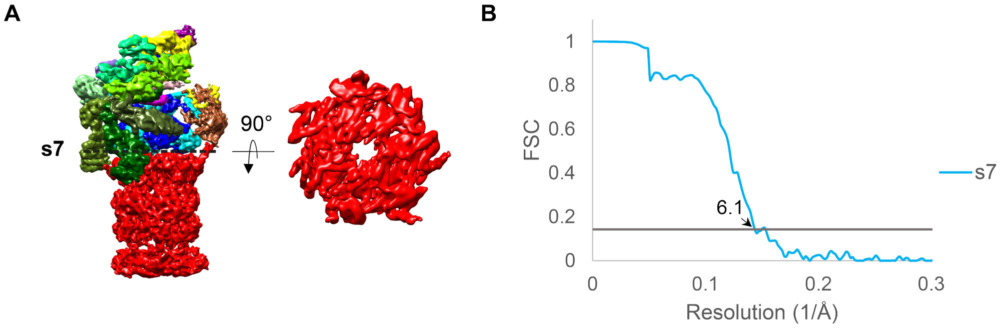

Figure 3.14: **Cryo-EM density of the s7 state.** (A) Reconstruction of particles of the s7 state. (B) The reconstruction achieved a resolution of 6.1 Å shown in the FSC diagram.

The analysis of each class in the substrate only sample did not show a clear substrate density. Such a clear substrate density is also not visible in the newly discovered state, yet lowering the threshold does show some extra fuzzy densities around Rpn1. The most clear density is located at the T1 binding site of Rpn1 possibly bridging towards Rpn13. A density in the middle of the OB-ring or ATPase ring was not visible. Also with focused classification using TOM foc analysis one defined density could not be classified, most likely hinting at a more flexible binding of the substrate to Rpn1.

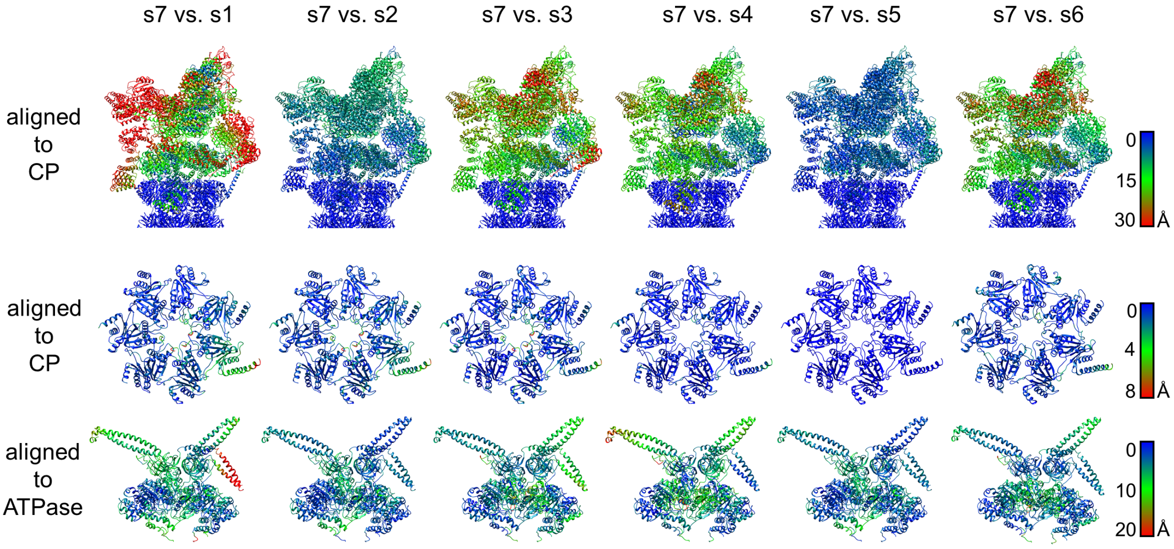

Figure 3.15: **RMSD comparison of s7 with the other states.** RMSD comparison of the model of the s6 state with the other six states (s1-s6). For comparison either the CP or the ATPase of the two models being compared was aligned. The range goes from blue, to green to red, where blue represents the smallest differences and red the largest differences between both models of the specific residue.

Particles of the s7 state were further refined and processed to achieve a resolution of 6.1 Å (Fig. 3.14). The s7 state was similar to the s5 state. Indeed, the distance between the N-terminal regions of Rpn5 and Rpn6, and the position of Rpn2 with respect to the CP are similar to those of s5. An atomic model for the substrate state s7 was generated using s5 as a starting model. To show the high resemblance at the model level of s5 to s2, and also the close resemblance of s7 to s5 RMSD calculations of s5 and s7 compared to the other states were carried out (Fig. 3.15).

The most prominent structural feature of the s7 state is its refined coaxial alignment of the OB-ring, the AAA+ ATPase ring, and the CP (Fig. 3.16A). Compared with the s5 state, the entire RP shifts by 5 Å, leading to the better coaxial alignment (Fig. 3.16B). The AAA+ ATPase subunits adopt a different conformation in s7 compared to s5. For example the Rpt4 small domain of the ATPase subunit in the s7 state is moved away from $\alpha7$ in the CP, which is similar to the distance observed in s3, s4 and s6. The height of Rpt6 with respect to the CP is as in s5 and a density for an inserted Rpt6 C-terminus can also be observed in s7. Further no clear density within the central pore in the EM map of the s7 state can be observed, suggesting the opening of the CP gate.

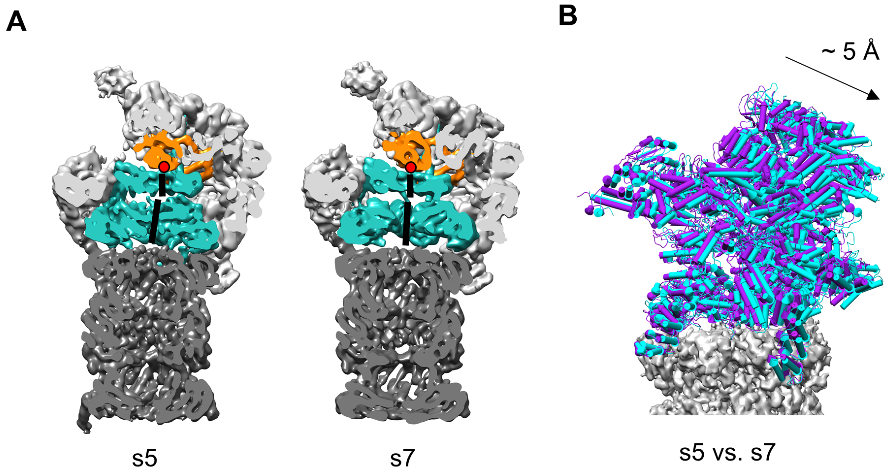

Figure 3.16: **Coaxial alignment comparison between s5 and s7.** (A) A side view of the EM densities cut in the middle shows the position of the active site of Rpn11 and the alignment of the OB-ring, the AAA+ ATPase ring and the CP in each state. (B) Superimposition of the models of the RP of the s5 (purple) and s7 (cyan) state. The models were prior aligned to the CP.

Overall, three different methods were utilized to modify the proteasomal state equilibria. The results all lead to the stabilization of activated states with an open CP gate. The results also have in common the stabilization of states with a higher co-axial alignment of RP and CP. An in-depth analysis and comparison of the closed and open gate states can now better explain how gate opening is triggered by the RP. And additional analysis of the different AAA+ ATPase conformations place the newly found states into a larger perspective within the scope of the degradation cycle.

3.5 The Gating of the 20S CP

3.5.1 The Analysis of the RP-CP Interface

Structures of the open gate CP have been reported with a variety of CP activators, including PAN, PA26, and a chimera PA26/28 protein containing the HbYX motifs of PAN (Groll et al., 2000; Whitby et al., 2000; Forster et al., 2005; Rabl et al., 2008). Recently, cryo-EM reconstructions of the 26S proteasome with the open gate CP were reported. Those studies revealed an involvement of at least one additional C-terminus (Rpt6) in triggering gate opening in *S. cerevisiae* and two C-termini (Rpt1 and Rpt6) for gate opening in humans. However, the fundamental mechanism of gate opening by the proteasome remains unclear due to the insufficient resolution (Chen et al., 2016; Wehmer et al., 2017).

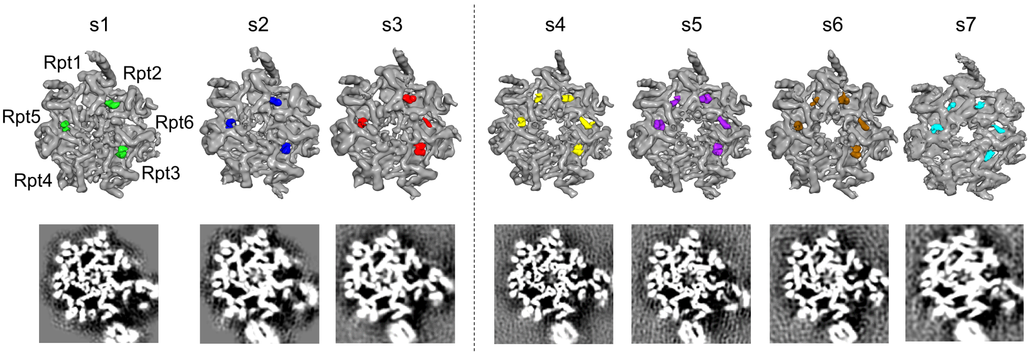

Figure 3.17: **The interface between the RP and the CP.** In the top view of the 20S the densities of the C-termini are shown colored in the same colors used in the state overview diagrams (s1 = green, s2 = blue, s3 = red, s4 = yellow, s5 = purple and s6 = brown, s7 = cyan). Additionally underneath a cut through the raw data shows the densities of each C-terminus. Figure adapted with permission from (Eisele et al., 2018).

The interface between the CP and the RP of the refined EM densities of the proteasome states were analyzed. Only three of the six Rpt C-termini contain a conserved HbYX motif. Originally it was proposed that the HbYX motifs of Rpt2, Rpt3, and Rpt5 trigger CP gate opening, based on biochemical studies with HbYX peptides of PAN, the archaeal proteasome (Rabl et al., 2008). The three HbYX motifs of Rpt2, 3 and 5 are stably docked into the α ring in the three closed gate states (s1, s2 and s3). In the remaining conformational states with an open gate (s4, s5, s6 and s7), the insertions of these HbYX motifs are observed. In addition to the HbYX motifs, two additional densities corresponding to the C-termini of Rpt6 and Rpt1 can be found docked into the α ring (Fig. 3.17). Although the Rpt1 and Rpt6 C-termini do not contain a HbYX motif, both C-terminal sequences are highly conserved (Fig. 3.18). In the s4 state solved with BeF$_x$, only the Rpt6 C-terminus was observed. This is probably due to the insufficient resolution and the overall weak density for the inserted Rpt1 C-terminus. In the s3 state, a minimal Rpt6 density can be found docked into the α ring. Because the gate is still occluded, it can be implied that the Rpt6 tail is either not sufficient to open the gate or it is not firmly docked and engaged in the s3 state.

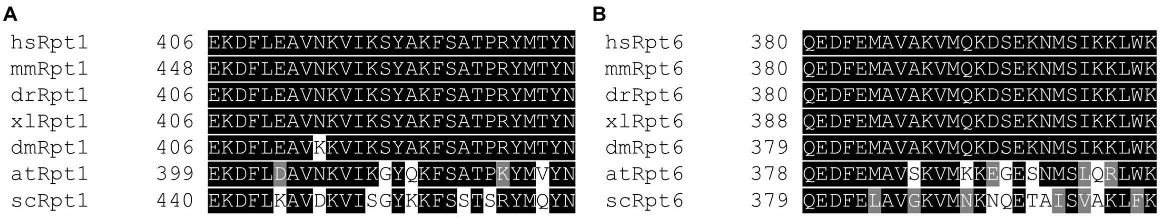
A
hsRpt1 406 EKDFLEAVNKVIKSYAKFSATPRYMTYN
mmRpt1 448 EKDFLEAVNKVIKSYAKFSATPRYMTYN
drRpt1 406 EKDFLEAVNKVIKSYAKFSATPRYMTYN
xlRpt1 406 EKDFLEAVNKVIKSYAKFSATPRYMTYN
dmRpt1 406 EKDFLEAVKKVIKSYAKFSATPRYMTYN
atRpt1 399 EKDFLDAVNKVIKGYQKFSATPKYMVYN
scRpt1 440 EKDFLKAVDKVISGYKKFSSTSRYMQYN
B
hsRpt6 380 QEDFEMAVAKVMQKDSEKNMSIKKLWK
mmRpt6 380 QEDFEMAVAKVMQKDSEKNMSIKKLWK
drRpt6 380 QEDFEMAVAKVMQKDSEKNMSIKKLWK
xlRpt6 388 QEDFEMAVAKVMQKDSEKNMSIKKLWK
dmRpt6 379 QEDFEMAVAKVMQKDSEKNMSIKKLWK
atRpt6 378 QEDFEMAVSKVMKKEGESNMSLQRLWK
scRpt6 379 QEDFELAVGKVMNKNQETAISVAKLFK

Figure 3.18: **Sequence alignments of Rpt1 and Rpt6 C-termini.** Boxshade alignments of the C-termini of Rpt1 (A) and Rpt6 (B) demonstrate high conservation of C-terminal amino acids. hs= *H. sapiens*; mm= *M. musculus*; dr= *D. rerio*; xl= *X. Laevis*; dm= *D. melanogaster*; at= *A. thaliana*; sc= *S. cerevisiae.* Figure adapted with permission from (Eisele et al., 2018).

To confirm the cooperative role of the Rpt1 and Rpt6 tails in gating the CP, yeast mutants lacking the most C-terminal amino acid of Rpt1 or Rpt6 were implemented. Truncated Rpt tails impaired efficient docking into the α pockets (Park et al., 2011, 2009). The effects of these truncations on RP-dependent gating of the CP were addressed via an in-gel peptidase assay using the fluorogenic substrate suc-LLCY-AMC. Taking into account a mild assembly defect in *rpt6-Δ1* cells, the peptidase activity was normalized to the total proteasome abundance in immunoblots of the same extract.

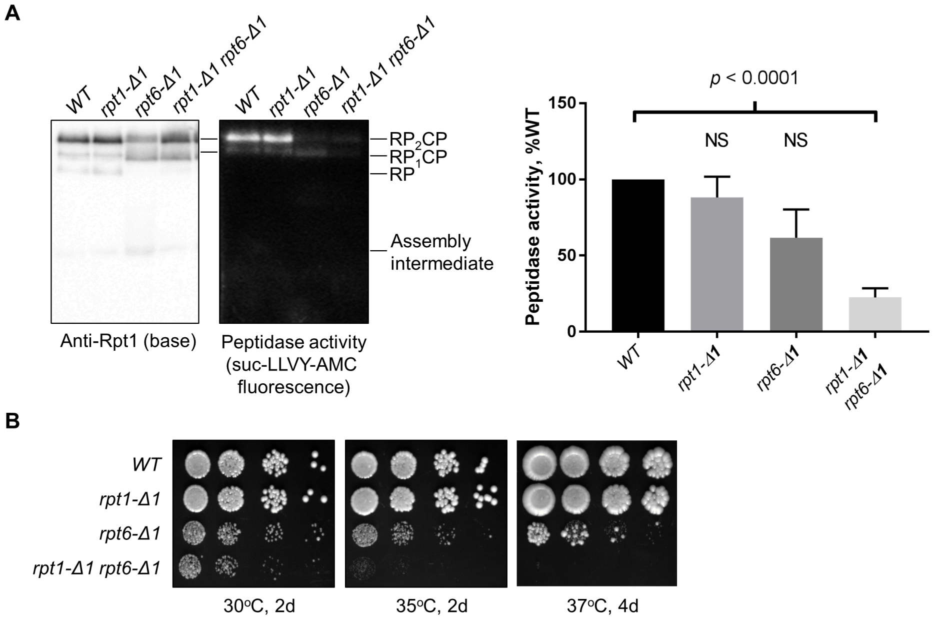

Figure 3.19: **Mutagenesis analysis of the Rpt1 and Rpt6 C-termini.** (A) Three Rpt C-termini mutants were prepared and tested for their peptidase activity based on suc-LLVY-AMC fluorescence. (B) The three mutants were tested during normal growth conditions and at elevated temperature stress conditions at 35°C and 37°C. The experiments were carried out by a collaborating lab. Figure adapted with permission from (Eisele et al., 2018).

Peptidase activity, shown by an accumulation of the fluorescence signal, can be seen for WT cells and *rpt1*-Δ*1* cells. Peptidase activity decreases slightly in *rpt6*-Δ*1* proteasomes, and peptidase activity decreases drastically by 80% in *rpt1*-Δ*1* *rpt6*-Δ*1* proteasomes. Especially the last result is highly indicative of a cooperative role of Rpt1 and Rpt6 in gate opening (Fig. 3.19A). Additionally, this finding was supported by a strong synthetic growth defect in the *rpt1*-Δ*1* *rpt6*-Δ*1* yeast (Fig. 3.19B). Together, these data support a model in which the C-termini of Rpt1 and Rpt6 cooperatively drive gate opening via interactions with the surface of the CP. Intriguingly, the N-terminus of Rpn1 is stably connected to the Rpt subunits Rpt1, Rpt2 and Rpt6 in the open gate state. Rpn1 is highly flexible, especially in the s2 state (Wehmer et al., 2017) and its local resolution is lower than the rest of the subunits. Stable docking of Rpn1 on the Rpt subunits hints towards an involvement of Rpn1 in gate opening. Further analysis is required to address the involvement of Rpn1 in gate opening.

3.5.2 The Analysis of the 20S α Ring

Based on the high-resolution structures of proteasomes with an open gate and a closed gate, we addressed how CP gate opening is influenced by the RP. This comparison is especially powerful when two states are so closely related and thus the key element to compare is the one element where they differentiate between one another. The s2 and s5 states are such an example, as they are highly similar to one another with an RMSD value of 4 Å, but the s5 state has an open gate and the s2 state a closed gate. Comparison of these states leads us to identify key elements for gate opening.

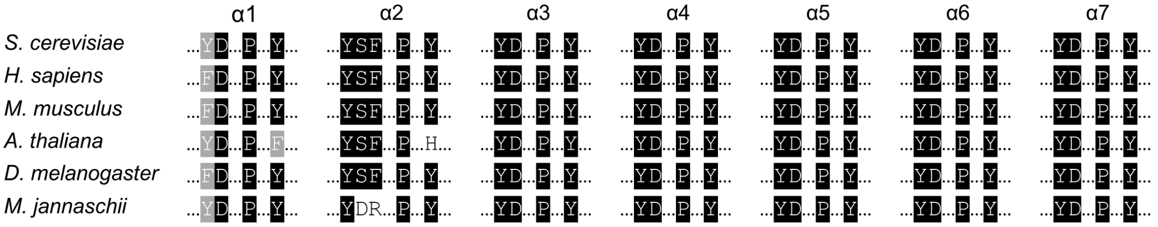

Figure 3.20: **Sequence alignments of YD-P-Y motif of α subunits.** Boxshade alignments of the N-terminal YD-P-Y motifs of all α subunits. Figure adapted with permission from (Eisele et al., 2018).

The approximately 5 Å or lower resolution of the EM structures of the s1, s2, s4 and s5 states allowed us to fit not only secondary structural elements but also side chains within the clear EM densities. For refining the gate of s1 and s2, the densities with the codes EMD: 3534 and 3535 were used, respectively. The starting models were PDB: 5mp9 and 5mpa for s1 and s2, respectively. In the closed gate the N-terminal extensions of α2, α3 and α4 lay down horizontally and hereby close the gate in the center pore of the CP. The remaining α subunit N-termini point upward towards the ATPase ring. The α4 Arg6 and Tyr4 form a cluster with the α3 Asp7 (Fig. 3.21A), as previously observed (Groll et al., 2000).

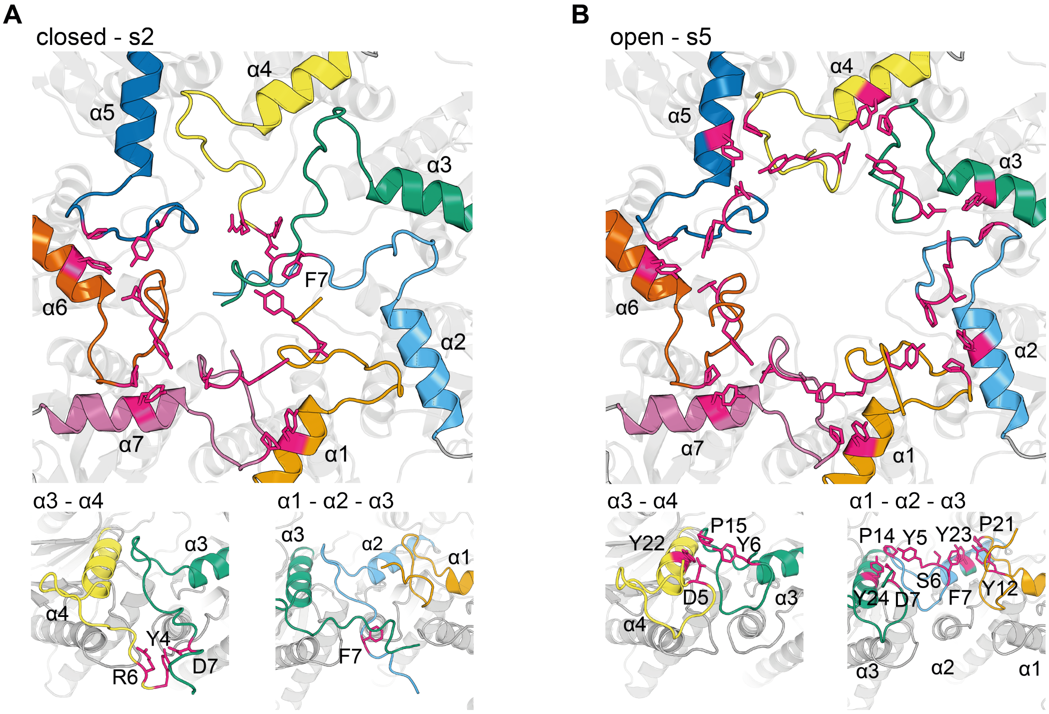

Figure 3.21: **Comparison of a closed and an open CP gate.** Model of the closed gate (A) compared to the model of the open gate (B) in the s2 state. In the smaller panels a different view of $\alpha1$, $\alpha2$, $\alpha3$ and $\alpha4$ can be seen. Figure adapted with permission from (Eisele et al., 2018).

Additionally, we observed that the Phe7 of $\alpha2$ nucleates the cluster, which most likely helps to keep the $\alpha3$ N-terminus in place and secure the gate over the CP pore (Fig. 3.21A, right panel). Interestingly in archaea the 20S α ring is formed by seven copies of the same α subunit. Yet, the N-terminal amino acid composition of the α subunits is highly conserved between all seven different α subunits in eukaryotes with some exceptions (Fig. **??**). One of these exceptions is the substitution of a normally conserved aspartate to Ser6 in the $\alpha2$ of *S. cerevisiae*. Additionally, in $\alpha2$ the conserved arginine (in three out of seven α subunits), which follows the conserved aspartate, is replaced by the already mentioned Phe7. PAN of archaea, which lacks this substitution, does not have an ordered gate (Forster et al., 2005; Groll et al., 2000), thereby implicating a role for $\alpha2$ Phe7 in stabilizing the ordered gate.

To further address the importance of $\alpha2$ Phe7 for the closed gate, the non-conservative $\alpha2$(F7A) mutation was introduced into yeast. The mutant strain was tested for resistance against the heavy metal Cd^{2+}, which induces oxidative stress, leading to protein unfolding in yeast. Open gate CP mutants were shown to be resistant to the heavy metal cadmium (Kusmierczyk et al., 2008). A resistance similar to that of such open gate mutants is found with the $\alpha2$ F7A mutant but it was not observed with the conservative $\alpha2$(F7Y) mutation alone (Fig. 3.22). These findings provide further support for the role of the $\alpha2$ N-terminus in acting as a linchpin for the closed gate.

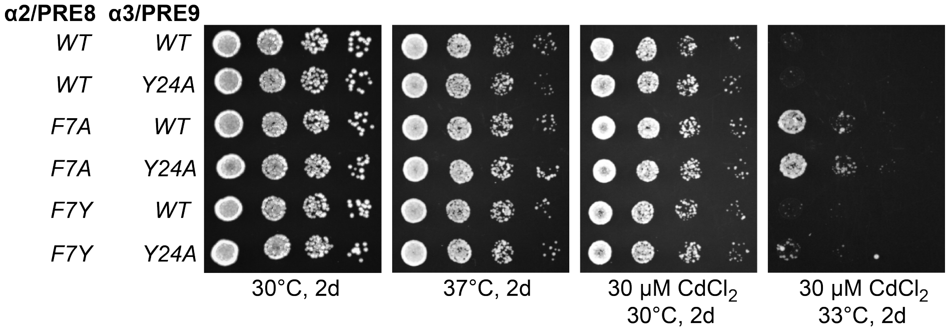

Figure 3.22: **Mutagenesis analysis of Phe7 in α2.** Phe7 of α2 and Tyr24 of α3 were mutated and cells were checked for viability under normal growth conditions and under stress conditions. One of these conditions is growth on $CdCl_2$, which causes stress in the form of increased protein unfolding. The F7A mutants grow better on $CdCl_2$ than wild type cells. The experiments were carried out by a collaborating lab. Figure adapted with permission from (Eisele et al., 2018).

The subunits α5, α6 and α7 are mostly unchanged between a closed gate and an open gate. The α5 and α6 N-terminal extensions point upwards by forming a cluster of conserved tyrosines and prolines from one subunit and tyrosine and aspartate residues of the counterclockwise-neighboring subunit (Fig. 3.23). This cluster is also found between α6–α7 and between α7-α1. In contrast, in the open gate structure, the N-terminal extensions of α3, α4 and α5 flip from the horizontal position to an upward vertical position, which is stabilized by the same clusters as found at the interface of α5-α6, α6-α7 and α7-α1.

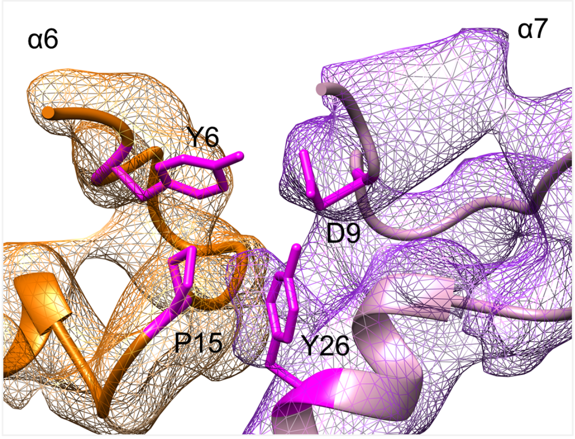

Figure 3.23: **Canoncial cluster between α6 and α7.** Canoncial YD-P-Y motif found between α6 and α7 in a closed and open gate. Figure adapted with permission from (Eisele et al., 2018).

Thereby, the N-termini form a cluster with two conserved tyrosines, a proline and one aspartate (YD-P-Y motif) at the interface between two α subunits at the periphery of the CP pore with one exception, at the interface of α1-α2 (Fig. 3.21B, right panel). As described earlier, α2 is the only α subunit in which the aspartate and the following arginine are not conserved and are substituted with a serine and phenylalanine. Although Ser6 still interacts with the other side chains, Phe7 increases the distance between Ser6 of $\alpha2$ and Tyr12 of $\alpha1$. This weakened cluster supports Phe7 as the linchpin of the closed gate which regulates gate opening.

The C-terminal tails of Rpt1 and Rpt6 insert in the pockets between $\alpha3$-$\alpha4$ and $\alpha2$-$\alpha3$, respectively (Fig. 3.24A). Interestingly in all open gate states, Pro14 in $\alpha2$ and the H0 helix of $\alpha3$ are repositioned by ~3-4 Å as compared to their positions within the closed gate states (Fig. 3.24B). These movements were not found in the s3 state where a minimal density for the Rpt6 C-terminus was observed. Thus, in eukaryotes, the N-terminal tails of the α-subunits are tightly regulated by canonical cluster formation, which is most likely regulated by insertion of the Rpt6 and Rpt1 tails. Taken together, a mechanism can be envisioned by which insertion of the Rpt6 and Rpt1 C-termini into the α ring pockets reorganizes the gate via displacement of the $\alpha2$-Phe7-centered linchpin. Only when both the Rpt1 and Rpt6 C-termini are inserted, where Rpt6 is in close proximity to $\alpha2$ and $\alpha3$ and Rpt1 is close to $\alpha4$ and $\alpha5$, can the gate open and the described cluster form. Insertion of the Rpt1 and Rpt6 C-termini may induce a movement of the proline loop in specific α subunits (Fig. 3.24B).

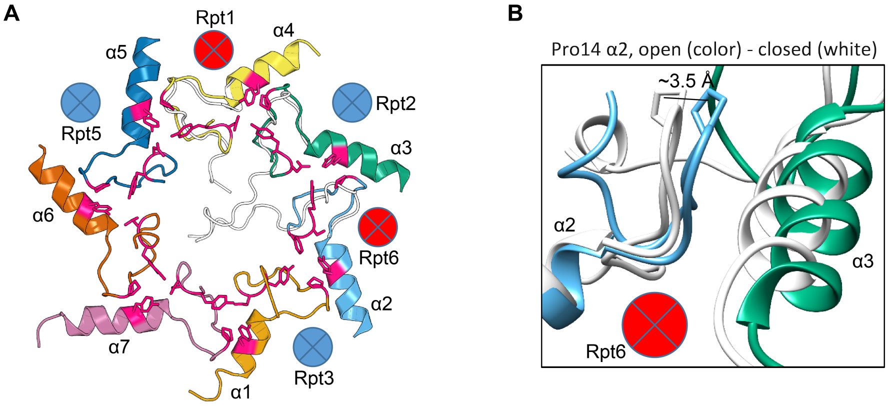

Figure 3.24: **N-terminal flipping and movement of $\alpha2$.** (A) The open gate is overlaid with the extensions of the N-termini of the α-subunits in the closed gate in white. Between the α subunits the position of the possibly bound C-termini can be found. (B) Pro14 of the $\alpha2$ subunit moves between the open and closed gate by ~3.5 Å. Additionally a movement of the H0 of a3 can be seen. This movement may be connected to binding of the Rpt6 and Rpt1 C-termini. Figure adapted with permission from (Eisele et al., 2018).

3.6 Analysis of the AAA+ ATPase

The AAA+ ATPase of the, in total, seven states was analyzed using distinct features. Nucleotides bind in the nucleotide pocket, located between two Rpt subunits and made of several motifs (described in 1.2.4). First an EM map of the ATPase was simulated without nucleotides and was then subtracted from the experimental map. The subtracted densities indicate the number of bound nucleotides. Similar to previous reports densities for nucleotides in all six nucleotide-binding pockets could be observed (Fig. 3.25) (Chen et al., 2016; Huang et al., 2016; Schweitzer et al., 2016; Wehmer et al., 2017).

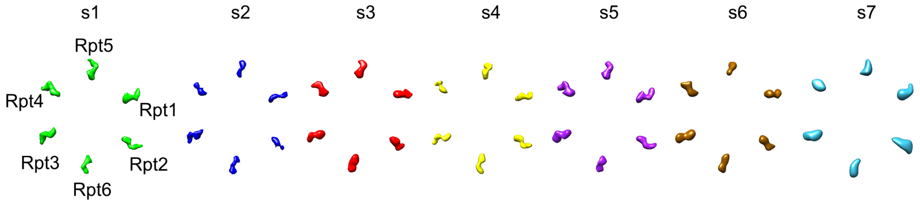

Figure 3.25: **Nucleotide pocket loading in five states.** Nucleotide densities of each state were generated by subtracting a generated nucleotide free density from the actual density. In all seven states, six densities are visible in the pockets. Figure adapted with permission from (Eisele et al., 2018).

Although six fully occupied nucleotide pockets were found in all states, the identity of the occupied nucleotide densities, either ATP, ADP+Pi or ADP cannot clearly be differentiated due to the limited resolution (Fig. 3.25). Instead I analyzed two key structural features, the distance of each pocket and the position of a well-conserved Phenylalanine cluster (Phe-cluster) to define each binding pocket. First, the pocket distance was measured between the end of the H10 helix connected to the pore-2 loop to the N-terminal tip of the Walker A motif located at the beginning of the H6 helix. Each pocket from each of the six states is distinguished into two clusters, hereby defined as engaged and open (Fig. 3.26). In the engaged pocket, the distance is 15 Å or smaller, whereas the distance in the open pocket is 18 Å or greater. In the s7 state, the configuration of the pocket distance was not clearly distinguished: overall the distance range spans from 21 Å to 15 Å, which shows lower diversity than in the other states resulting in s7 being the most planar state seen so far.

3.6.1 The Conserved Phe-Cluster

Often these pocket distances correlate well with the second key feature, the Phe-cluster, defined by the position of a well-conserved phenylalanine at the end of H10 in each Rpt subunit. In the engaged pocket, the conserved phenylalanine faces the neighboring subunit in a clockwise direction and interacts with an arginine and phenylalanine located in the $\beta2$ and $\beta3$ strands of the counter-clockwise neighbouring subunit (Fig. 3.27). In contrast, in

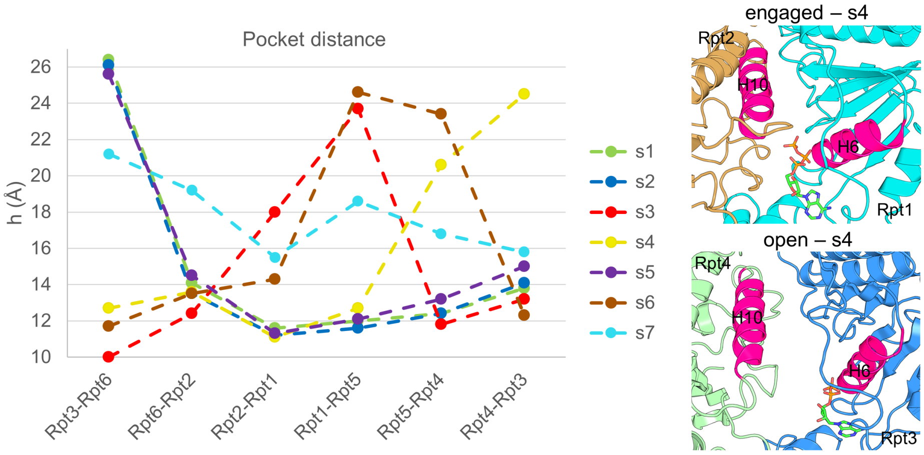

Figure 3.26: **Distance of nucleotide pockets.** The pocket distance of each pocket from all seven states is plotted. The distance was calculated between the beginning of the H6 helix and the end of the H10 helix. An engaged pocket can be found between Rpt2 and Rpt1 in the s4 state and an open pocket is found between Rpt4 and Rpt3 also in the s4 state. Figure adapted with permission from (Eisele et al., 2018).

an open pocket, the phenylalanine points to the opposite side, inwards to H9 of the same ATPase subunit. Despite a similar resolution as in s6, the ATPase is less well resolved in the s7 state. Although only one engaged Phe-cluster was found in the s7 state, the results might be different in a higher resolved EM density. Overall s7 is highly flexible, which is why a clear analysis currently proves difficult.

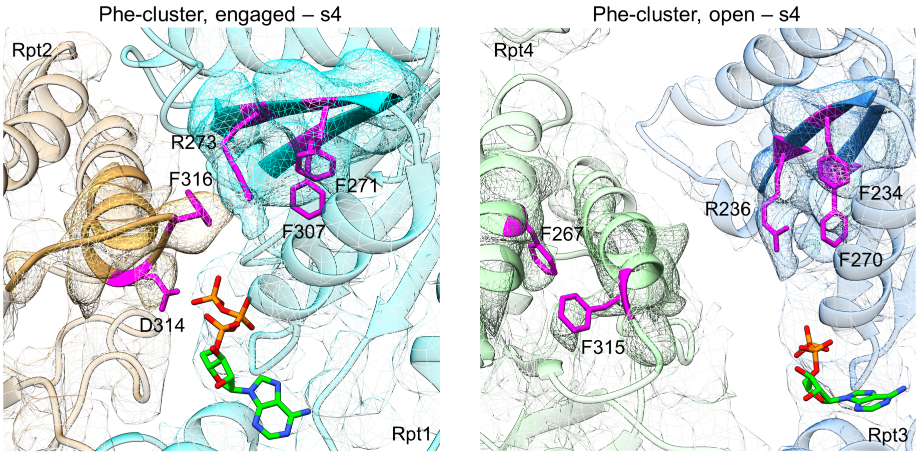

Figure 3.27: **Phe-clustering between nucleotide pockets.** An example of an engaged Phe-cluster which can be found between Rpt2 and Rpt1 and an open Phe-cluster which can be found between Rpt4 and Rpt3. Figure adapted with permission from (Eisele et al., 2018).

Nevertheless by applying these measurements to the Rpt subunits of each proteasome state, a total of three different types of nucleotide pockets for states s1-s6 can be identified. A pocket is either open both in terms of the helical distance and the Phe-cluster (open), it can have an engaged pocket as determined by the helical distance, but an open Phe-cluster (intermediate) or finally it can be completely engaged in both factors (engaged) (Fig. 3.28).

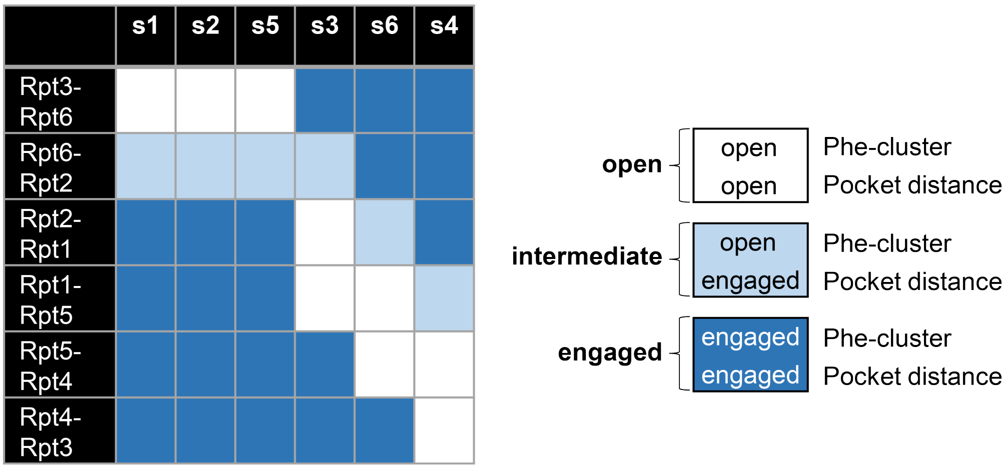

	s1	s2	s5	s3	s6	s4
Rpt3-Rpt6	□	□	□	■	■	■
Rpt6-Rpt2	▨	▨	▨	▨	■	■
Rpt2-Rpt1	■	■	■	□	▨	■
Rpt1-Rpt5	■	■	■	□	□	▨
Rpt5-Rpt4	■	■	■	■	□	□
Rpt4-Rpt3	■	■	■	■	■	□

open
open
open
Phe-cluster
Pocket distance
intermediate
open
engaged
Phe-cluster
Pocket distance
engaged
engaged
engaged
Phe-cluster
Pocket distance

Figure 3.28: **Overview of Phe-Cluster and pocket distance.** Representation of each pocket from s1-s6 with the two factors, the Phe-cluster and pocket distance, indicated. White indicates an open pocket, light blue an intermediate pocket and dark blue an engaged pocket. Figure adapted with permission from (Eisele et al., 2018).

The differentiation of open and engaged pockets was additionally supported by hierarchal clustering of masked nucleotide pocket maps (Fig. 3.29). This is especially important to confirm the configurations of the nucleotide pocket in the two lower resolved states, s6 (6.1 Å) and s7 (6.1 Å). For hierarchal clustering the models of all Rpt subunits from each state were aligned to the interface between Rpt1 and Rpt5 of the s1 state using Chimera matchmaker. The 42 corresponding EM maps were then filtered to 8 Å and aligned using the Chimera matrixcopy function. A spherical mask with a diameter of 41 Å was placed around the arginine R255 of Rpt1 to focus on the binding pocket. The preprocessed volumes were finally hierarchically clustered using MATLAB and TOM toolbox. Each density was compared, leading to a total of two identified clusters (Fig. 3.29). The average from the blue class could be assigned to the engaged conformation whereas the gray class resembles the open conformation. The panel on the right shows an overview of the results with each state and Rpt interface (Fig. 3.29, right panel).

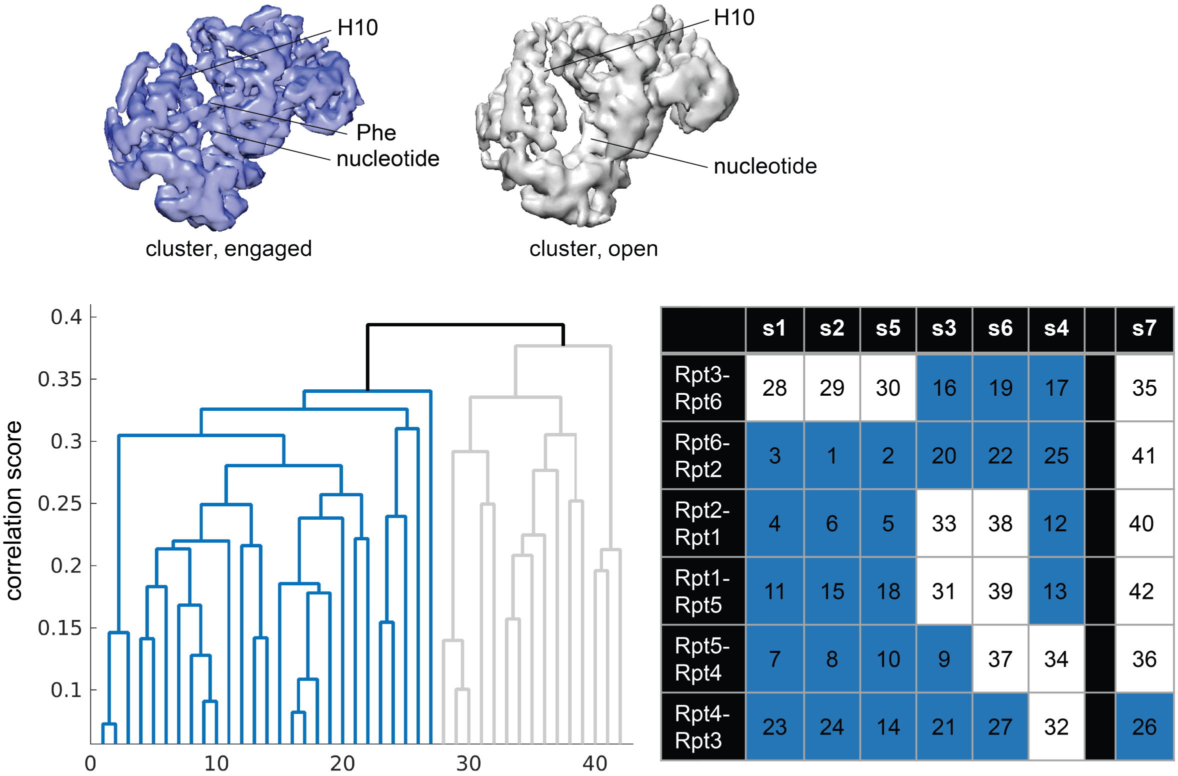

	s1	s2	s5	s3	s6	s4		s7
Rpt3-Rpt6	28	29	30	🟦 16	🟦 19	🟦 17		35
Rpt6-Rpt2	🟦 3	🟦 1	🟦 2	🟦 20	🟦 22	🟦 25		41
Rpt2-Rpt1	🟦 4	🟦 6	🟦 5	33	38	🟦 12		40
Rpt1-Rpt5	🟦 11	🟦 15	🟦 18	31	39	🟦 13		42
Rpt5-Rpt4	🟦 7	🟦 8	🟦 10	🟦 9	37	34		36
Rpt4-Rpt3	🟦 23	🟦 24	🟦 14	🟦 21	🟦 27	32		🟦 26

Figure 3.29: **Hierarchical clustering of nucleotide binding pocket.** Each interface of each Rpt density was aligned to the interface of Rpt1 and Rpt5 and afterwards hierarchically clustered. In total two clusters could be found, which show on the one hand an engaged cluster (blue) and on the other an open cluster (white). Figure adapted with permission from (Eisele et al., 2018).

All intermediate states were designated as engaged except for the intermediate pocket of Rpt2-Rpt1 from the s6 state, which was defined as open, probably due to the lower resolution of the s6 state as compared to the other states. Each state is hereby characterized by a specific arrangement of pocket states. In s1, s2, and s5, the same arrangement of engaged pockets for Rpt1, 5, 4, and 3 followed by an open Rpt6 pocket and an intermediate Rpt2 pocket is observed. The open pocket sits at Rpt6, the subunit directly at the split site. In contrast, s3, s4 and s6 show a slightly different pocket arrangement. Indeed, in the s3 state, the first open pocket is located at the split site (Rpt1), which is then followed by another open pocket (Rpt5). Three engaged pockets are then positioned counterclockwise from the open pockets (Rpt4, 3 and 6), followed by one last intermediate pocket (Rpt2). Intriguingly, this pattern is permuted one subunit counterclockwise from s3 to s6 and again from s6 to s4, hinting at a rotary catalytic mechanism.

Chapter 4

Conclusions and Discussion

In this thesis, I carried out cryo-EM experiments to explore the conformational landscape of the proteasome, leading to the identification of three additional conformational states of the 26S proteasome of *S. cerevisiae*. Based on the structures, the regulatory mechanism of CP gating by the RP was revealed and light was shed on a rotary mechanism of the ATP cycle. In detail, this work implicates a key role for Rpt6 in promoting activation of the proteasome and in transmitting the nucleotide state of the AAA+ ATPase ring to the CP. The results support a model in which gating of the CP is a multi-step process dependent upon distinct nucleotide binding events and the action of multiple ATPase tails. Such a multi-step gating mechanism is likely important to ensure tight coupling of proteolysis to the unfolding cycle of the proteasomal RP. Further, the analyses of conformational redistribution in *rpt-EQ* mutants suggests ATPase specific roles in the catalytic cycle and is in strong support of a rotary hydrolysis model for the proteasome, similar to that recently proposed for related AAA+ family ATPases Hsp104, Vps4, and Yme1 (Gates et al., 2017; Monroe et al., 2017; Puchades et al., 2017).

4.1 The Substrate Engaged Structure

First, I designed a model substrate with key features, including more than four ubiquitins and an unstructured initiation region with at least 30 amino acids (Thrower et al., 2000; Takeuchi et al., 2007; Prakash et al., 2009; Inobe et al., 2011), with the aim of understanding substrate processing by the proteasome. The degradation studies of the model substrate showed that the substrate was recognized by the 26S proteasome and was primarily deubiquitinated but not degraded. Unlike K48-linked chains, the structure of the linear ubiquitin chain is similar to K63-linked polyUb chains, which do not preferentially target the proteasome for degradation (Komander et al., 2009). It has been reported that non specifically targeted proteins, like substrate with K63-linked polyUb chains are removed more quickly than substrate translocation is initiated for the rescue of the substrate (Jacobson et al., 2009). In addition, *in vivo* proteasome function is modulated by cofactors that transiently bind to the proteasome (reviewed in (Förster et al., 2014)). But many of these cofactors are lost during the purification (Sakata et al., 2011). *In vivo* degradation of the model substrate may be assisted by those cofactors, which could lead to degradation by the proteasome *in vivo*. Lastly, an unstructured region of 30 amino acids is at the border of being a suitable length for translocation initiation (Inobe et al., 2011) and a 6xHis tag attached to the C-terminus of the substrate may hinder it from being grabbed by the aromatic pore loops. Similar to the recently described study (Jacobson et al., 2009), the timing between substrate translocation and deubquitination needs to be perfectly calibrated. If substrate translocation is too slow due to the non-optimal unstructured region or the tight fold of the protein, the substrate might be deubiquitinated too early before being able to be degraded by the proteasome. Even though the substrate was not degraded by the 26S proteasome, the substrate was stabilized through inhibition of Rpn11 by *o*PA. This shows that Rpn11 is likely the key DUB that hinders degradation of the DHFR substrate. Rpn11 changes its localization from the s1 state to the activated states and positions itself directly above the entrance to the central channel of the ATPase ring, where it removes ubiquitin chains from substrates during translocation (Worden et al., 2014, 2017). Through inhibition of Rpn11 with *o*PA and addition of substrate, activation of the 26S proteasome was observed. Instead of a mixture of the s1 and s2 states, a not-yet identified conformational state, s7, with characteristics of an activated proteasome state, was observed. In 2012, the Martin group reported a proteasome structure in which the proteasome was activated by the addition of a model substrate but no substrate density was resolved (Matyskiela et al., 2013). Similar to the previous study, no clear density for the DHFR substrate was observed in the s7 state. The substrate most likely binds to the proteasome in many different conformations though multiple ubiquitin binding sites, which is thus unable to achieve better resolved densities. A flexibly bound substrate would be one of the explanations as to why one clear s7 state could not be found and instead four highly similar classes of the *o*PA only and *o*PA plus substrate samples were combined. The differences between each class were marginal but analysis of features like the ATPase or the gate was significantly more difficult and will require more data in the future. If substrate in the combination with *o*PA results in a range of s7-like particles it is interesting to think of why *o*PA alone also leads to s7-like particles even though no substrate was added. Most likely the proteasome can be activated by unknown factors binding to the proteasome, which leads to the s7-like states when the active site of Rpn11 is inhibited. The amount of proteasome activation is still higher when substrate is added, as shown by the lack of s1 and s2 states in the *o*PA + substrate data set.

4.2 Modification of the State Landscape

Overall activation of the proteasome conformation can be achieved through several methods, all which involve manipulation of the ATPase cycle. In the past years activation of the proteasome and differentiation of the states were often defined by subunit movements bigger than 10 Å, thus making it possible to distinguish the states in the range of the resolutions reached in the beginning of proteasome structural work (Unverdorben et al., 2014). Such significant changes were observed in subunits such as Rpn1, Rpn2, Rpn5, Rpn6, together with alignment of the central channels of the ATPase and the CP rings. Upon achieving higher resolutions, more detailed structural features such as the state of the CP gate, either closed or open, and the planarity of the ATPase ring, determined by measuring the height of the pore loops, were analyzed (Wehmer et al., 2017). With increasing ATPγS concentration, the amount of s1 particles was reduced and replaced by a higher abundance of the activated states. With a concentration of 0.5 mM ATPγS the amount of s5 particles was increased but these particles gradually vanish upon increasing concentration of ATPγS, where the s3 state was more pronounced. This result can be compared to a titration assay where with increasing amounts of ATPγS the peptidase activity of the proteasome was reduced (Smith et al., 2011). If s3 is more prevalent at higher ATPγS concentrations it would actually makes sense to have less peptidase activity because if the more closed gate with higher nucleotide concentrations. In a recently published study, the structure of the human proteasome in the presence of ATPγS was reported. Although the direct impact of different ATPγS concentrations on the conformational landscape was not addressed, it showed that the human 26S proteasome can also be pushed to different states in the presence of ATPγS, called S_{D1}, S_{D2} and S_{D3} (Zhu et al., 2018). The first ATPγS studies completed with 26S proteasome were done by the Baumeister group in 2013 (Sledz et al., 2013). It was then reported that 1 mM ATPγS was used, resulting in a slightly different state landscape than reported here with 0.5 mM ATPγS or 2 mM ATPγS. In the earlier study it was actually reported that the states found with 1 mM ATPγS were s1, s2 and s3. Differences in sample preparation, for example longer incubation time during plunging, but also technical improvements leading to better resolution and particle classification can provide a few explanations for these observed differences. In comparison to the *rpt-EQ* muntant results, the conformational landscape of the *rpt2-EQ* and *rpt6-EQ* mutants is similar to the dataset of the low concentration of ATPγS. Even though *rpt2-EQ* and *rpt6-EQ* show similar state distributions, the *rpt6-EQ* cells showed a growth defect in contrast to the relatively healthy *rpt2-EQ* cells. This minimal disruption is consistent with published *in vitro* studies (Beckwith et al., 2013). The results from the *rpt2-EQ* recombinant proteasome system of the published study suggest that the *rpt2-EQ* mutation does not largely affect the ATP hydrolysis cycle and the proteasome is still able to degrade substrates, which was shown by the accumulation of polyUb substrates in *rpt6-EQ* but not in *rpt2-EQ* (Beckwith et al., 2013). The *rpt6-EQ* mutation, in contrast, might have defects in the ATP hydrolysis cycle, leading to a static conformation and impairment of substrate degradation. Because only a snapshot of the state landscape is observed an answer to the dynamics of the states cannot be given. Thus, combinations of nucleotide analogs and ATPase *rpt-EQ* mutants have proven to be a powerful tool for modifying the state equilibrium, leading to the further identification of proteasome conformational states.

4.3 The Open Gate Mechanism

Together with previous studies, in total three closed gate states (s1, s2, s3) and four open gate states (s4, s5, s6, s7) were resolved. To understand the fundamental mechanism of gate opening, I compared the better-resolved closed and open gate states (<5 Å). Similar open gate conformations and corresponding amino acid interactions are consistently found in each of the open gate states of the 26S proteasome. A consistently found cluster between the N-terminal extensions of the alpha subunits is found in all of these states. These conserved open gate clusters (YD-P-Y motif) are also preserved in the other open gate structures of the CP with different activators such as PA26 and Blm10 (Whitby et al., 2000; Forster et al., 2005; Sadre-Bazzaz et al., 2010; Yu et al., 2010). The YD-P-Y motif can be found in the homoheptameric 20S core particles of archaea as well as in the heteroheptameric 20S core particles of eukaryotes with only one exception in the conservation from archaea to eukaryotes. Only the clustering between the $\alpha1$ and $\alpha2$ subunits with the YD-P-Y motif is not conserved thereby resulting in slight differences between the archaeal gate and the eukaryotic gate. In $\alpha2$, aspartate was substituted to Ser6 and arginine to Phe7 from the archaeal to the eukaryotic system. The substitution to Phe7 in eukaryotes weakens the conserved clustering in the open gate conformation by increasing the distance between the Tyr12 of $\alpha1$ and Ser6 $\alpha2$. In the closed gate of eukaryotes, Phe7 instead plays a key role in stabilizing the closed gate through the interaction with the N-terminal extension of $\alpha3$. In eukaryotes, Phe7 of $\alpha2$ most likely plays an important role in stabilizing the closed gate and additionally works as a disruptive measure in the open gate cluster formed between $\alpha1$ and $\alpha2$ (Fig. 4.1).

Recent structural studies of the 26S proteasome showed that the three conserved HbYX motifs of Rpt2, Rpt3 and Rpt5 are constitutively inserted into the alpha pockets even though the gate in most of these structures remained closed. This therefore indicates that HbYX motif insertion is not sufficient to promote gate opening. A model of Rpt6- and Rpt1-dependent gating is supported by the three open gate states, where the Rpt6 and Rpt1 C-termini are clearly detected at the α subunit interface in addition to the three constitutive HbYX motif insertions. An Rpt6 and Rpt1-dependent gating could additionally be supported by mutagenesis studies, which show reduced peptidase activity *in vitro* and growth defects *in vivo* when the Rpt6 and Rpt1 C-termini are synergistically deleted. The C-termini of Rpt6 and Rpt1 dock into the pockets formed by $\alpha2$–$\alpha3$ and $\alpha4$–$\alpha5$, respectively. $\alpha2$, $\alpha3$ and $\alpha4$ are critical for gate formation and therefore closely related to gate switching (Fig. 4.1). Lastly, a stabilized N-terminus of Rpn1 in the open gate structures is observed. I speculate that Rpn1 may stabilize the C-terminal insertion through interaction with Rpt6 and Rpt1. Otherwise, Rpn1 might even trigger the insertion event to open the gate. Further analysis of the Rpn1 structure is required to understand the role of Rpn1 in gate opening.

As speculated in previous work, proline movement might also be directly involved in gate

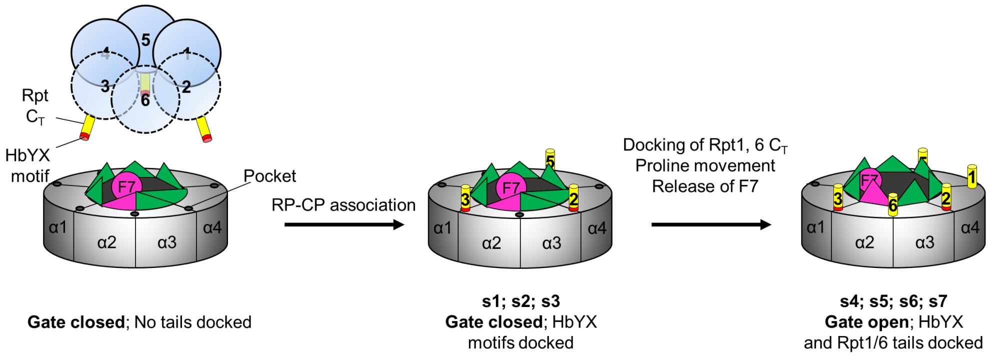

Figure 4.1: **Gate model.** The importance of the Rpt1 and Rpt6 C-termini in gate triggering shown as a cartoon representation. Phe7 of $\alpha2$ is marked in pink to pinpoint the possible importance as a linchpin for gating. Figure adapted with permission from (Eisele et al., 2018).

opening by flipping of the alpha subunit N-termini and stabilizing the clusters in the 26S proteasome. In PA26, insertion of seven loop regions of PA26 into the alpha ring pockets shift the proline loops of each α subunit, leading to CP gate opening (Whitby et al., 2000). In contrast to PA26, the RP regulates gate opening by the C-termini of the Rpt subunits of the hexameric ATPases, none of which possess activation loops. In an earlier report, it was speculated that HbYX docking leads to a rotation of the α ring and with that a shift of the proline loops causes opening of the gate (Yu et al., 2010). However, no significant rotation of the α subunits was observed. Only with both the Rpt1 and Rpt6 tails inserted, where Rpt6 is in close proximity to the $\alpha2$ and $\alpha3$ subunits and Rpt1 to the $\alpha4$ and $\alpha5$ subunits, does the gate open by forming the described open gate clusters. Interestingly instead of a rotation a clear proline loop movement of the $\alpha2$ subunit by 4 Å is observed, which is accompanied by movement of H0 of the $\alpha3$ subunit. It can be speculated that these movements could finally be the trigger for destabilizing Phe7, thereby causing flipping of the N-terminal extensions and opening of the gate. It was shown how Rpt2 has a major function in nucleotide-dependent priming for gate opening (Kohler et al., 2001; Rubin et al., 1998). Rpt2 sits between two key subunits involved in gate opening, Rpt1 and Rpt6. Considering that a majority of states found in the *rpt6-EQ* and *rpt2-EQ* mutants have an open gate, it can be speculated that loading of ATP in either Rpt6 or Rpt2 is needed for the tail insertion of Rpt6 and Rpt1. Furthermore, this also leads to the hypothesis that in the s5 state Rpt6 or Rpt2 has ATP bound more stably than in s2, leading to an open gate state. Stable nucleotide binding in these Rpt subunits might therefore be one of the initiating events of the degradation cycle.

4.4 Sequential Nucleotide Driven Translocation

In this thesis, I reported that the conformational landscape of the proteasome is influenced both by nucleotide binding and nucleotide analog concentration. Incorporation of ATPγS into a nucleotide binding pocket should lead to a slowed down ATP hydrolysis at the corresponding subunit. Similar to ATPγS, the *rpt-EQ* mutants also slow down the hydrolysis cycle at specific Rpts. In this case with the difference that it is known which Rpt subunit is experiencing not only a reduced rate of ATP hydrolysis but rather are complete reduction of hydrolysis at the mutated ATPase. Both manipulations lead to higher activated proteasome states in which the ATPase ring is in a more planar conformation and the rigid-body conformation formed between two Rpt subunits becomes highly uniform. Most likely through that the ATPase activity is enhanced.

Recently, several groups reported asymmetric architectures of related homohexameric AAA+ ATPases such as p97, Hsp104, Vps4, and Yme1 (Banerjee et al., 2016; Gates et al., 2017; Monroe et al., 2017; Puchades et al., 2017). In these studies the nucleotide binding pockets were particularly well characterized. For example, Puchades et al reported that the Phe-cluster allosterically regulates the pore loop movement upon ATP hydrolysis (Puchades et al., 2017). These Phe-clusters are also found in proteasomal ATPase subunits. Even though the relation between pore loop position and Phe-cluster conformation, as shown in (Puchades et al., 2017) was not observed, the Phe-cluster and the pocket distance were analyzed to characterize the nucleotide pockets. The detailed analysis of each nucleotide-binding pocket revealed three distinct modes that are distinguished by the state of the Phe-cluster and of the pocket distance: open, intermediate, or engaged. The nucleotide pocket configurations in the heterohexameric 26S AAA+ ATPase resembles closely the common configurations of the simpler homomeric Yme1 ATPase with ATP-bound (engaged), ADP-bound (open) and empty (open) pockets. In addition, the arrangement of the ATPase subunits, engaged – engaged – engaged – intermediate – open – open, in the activated states (s3, s4 and s6) resembles that of the simpler homomeric AAA+ ATPases Yme1; ATP-bound, ATP-bound, ATP-bound, ATP-bound, ADP-bound and empty. Because nucleotides are still seen in all binding pockets, it could not be assigned whether the open pockets are actually empty or ADP-bound pockets. Considering the relatively smeared density of the nucleotides, I assume that the nucleotide density which is observed in the open pocket is a mixture of nucleotide states, e.g. empty and ADP-bound states. In Yme1, substrate translocation is believed to follow a sequential nucleotide-driven translocation, by which the same ATPase arrangement, four engaged subunits and two open pockets, is shifted by one subunit during each ATP hydrolysis cycle by the trailing engaged subunit (Monroe et al., 2017; Puchades et al., 2017). A similar subunit shift can be envisioned from s3 to s6 to s4 for the 26S proteasome, which implies a conserved mechanism for sequential nucleotide-driven translocation.

ATP hydrolysis can occur in either the lowermost engaged and most likely ATP-bound subunit, as was suggested for Yme1 (Puchades et al., 2017), or the highest engaged subunit (Martin et al., 2008), and continues around the ring. This, for example, would mean that, in the s4 state, Rpt5 would fire to transition into the s6 state and then Rpt1 would fire for the transition into s3 in a clockwise fashion. If ATP hydrolysis proceeds counterclockwise, then ATP hydrolysis of the next engaged subunit should be the one at a lower position of the lock-washer conformation. Rpt4 hydrolysis would move the 26S proteasome from s3 into the s6 state and then firing of Rpt3 moves the proteasome into the s4 state. A counterclockwise hydrolysis was hypothesized for Yme1, which could also be true for the 26S proteasome based on the results from the *rpt-EQ* mutants. In detail, accumulation of the s6 state is observed by an *rpt3-EQ* mutation which blocks hydrolysis at Rpt3. In a counterclockwise hydrolysis cycle, Rpt3 hydrolysis is needed to move from the s6 state to the s3 state, and thereby blocking Rpt3 hydrolysis should freeze the 26S proteasome in the s6 state, which is exactly the state found in the *rpt3-EQ* data set.

In the well-studied ClpX-ClpP complex the orientation of the ATPase cycle was investigated through the use of several mutations (Martin et al., 2005). Interestingly the staircase arrangement in ClpX is different compared to the AAA+ ATPase of the 26S proteasome, in the substrate-free form two staircases can be found, which decline counterclockwise and not clockwise (Glynn et al., 2009). ATPase hydrolysis in a clockwise direction is hypothesized, which again would fit with the counterclockwise hydrolysis in the 26S proteasome because of the mirrored staircase arrangement.

The steeper stairway arrangement of the 26S proteasome seen in s1, s2 and s5 and also the inverted order of open and intermediate nucleotide pockets as compared to s3, s4 and s6 cannot be explained yet. This different arrangement might hint towards an initiation mechanism of the ATP hydrolysis cycle. The s7 state which is observed in the presence of a model substrate with Rpn11 inhibitor adopts a planar arrangement of the ATPase subunits, which may reflect a natural activated state of the ATPases because neither the nucleotide analogs nor the EQ mutants which induce the activated conformation of the proteasome are used. In regards to the complete RP rearrangement the s7 state would fit best after s2/s5 but before s3, s6 and s4.

In summary, the following model for proteasome activation, ATP hydrolysis and gate opening is hypothesized (Fig. 4.2): Without substrate the proteasome exists in the ground state (s1). In the ground state the OB ring, ATPase ring and CP are the least aligned in all found states, the HbYX motifs of Rpt2, Rpt3 and Rpt5 are inserted but the gate remains closed. Through binding of substrate it is hypothesized that the proteasome moves into one of the primed states (s2 or s5) or even directly into the s7 state. During this transition, the RP undergoes a movement, the OB ring, ATPase ring and CP co-axial alignment increases and in s5 and s7 the C-termini of Rpt6 and Rpt1 insert into the CP. This insertion leads to

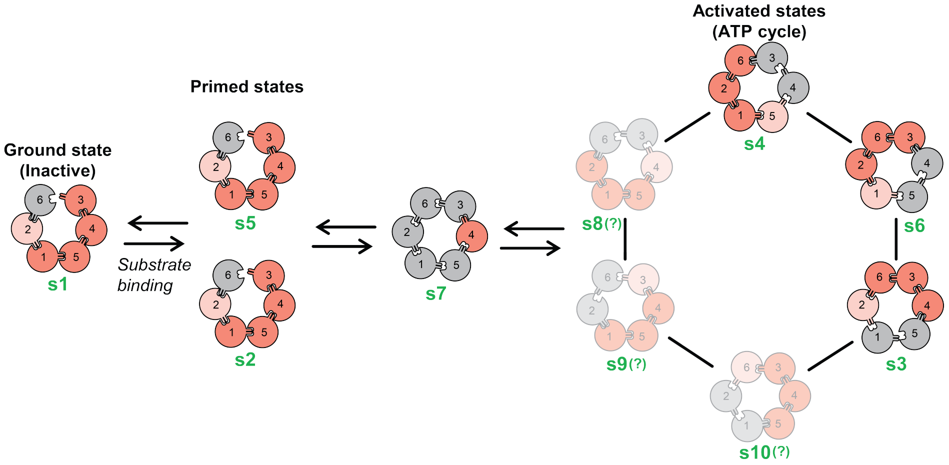

Figure 4.2: **The AAA+ ATPase degradation cycle.** A schematic overview of a proposed AAA+ ATPase degradation cycle with all identified states of the 26S proteasome. Closed pockets are red, intermediate pockets are light red and open pockets are gray. The three states s8, s9 and s10 were not identified so far and were added as hypothetical states. Figure adapted with permission from (Eisele et al., 2018).

movement of the $\alpha2$ N-terminal extension, which displaces the Phe7 linchpin of $\alpha2$, leading to flipping of the N-terminal extensions to open the gate. The translocation of substrate may be triggered by ATP hydrolysis by one of the initiating ATPases (Rpt1) coupled with ATP binding by Rpt6, leading the proteasome to an activated state (s3, s4, s6, probably several other unidentified conformations). The cycle could follow either a clockwise sequential hydrolysis driven translocation or proceed counterclockwise. ATP hydrolysis will lead to a conformational change, nucleotide exchange and with that a change in the proteasome state of the ATPase cycle. Additional states may still exist (s8, s9, s10), which adopt different nucleotide pocket arrangements. The cycle might continue until the substrate is completely translocated and includes possible reversion to s2, s5, s7 or s1. Although the specific steps in the ATPase catalytic cycle remain elusive, these results expand our knowledge of subunit-specific communication within the proteasomal ATPase ring and form a framework for in-depth mechanistic studies of ATPase function and its relationship to substrate processing.

Chapter 5

Future Perspectives

Stabilization of less abundant states and the discovery of new states has enhanced our understanding of the 26S proteasome. As if to find another piece of the puzzle, identification of each conformational state helps us draw a nearly complete picture of the proteasome conformational landscape. But the proposed model of the degradation cycle shows that there may exist more conformational states to fully explain the AAA+ ATPase cycle. The preserved placement of three distinct configurations of the nucleotide binding pockets provides evidence for a sequential nucleotide-driven translocation. However, to confirm this hypothesis, further structural analysis of the proteasome is required. For example, it is necessary to find a condition to stabilize hidden conformational states with different ATPase configurations. One way to even further expand the state landscape would be to combine the model substrate with proteasomes with different directed point mutations, thus stalling the proteasome in specific, yet-unidentified states. Overall further point mutations, in the ATPase for example, could also shed light on proteasome conformational switching.

Part of understanding the ATPase cycle is also understanding the role of s2 and s5 in substrate processing. In detail, it was not addressed yet whether the s2 and s5 states are the subsequent conformations of the s1 state or are the end points of the entire degradation cycle. The large conformational differences between s1 and s2/s5, such as the co-axial alignment of the rings and rotation of the lid subunits, are still hard to account for with the nearly exact same ATPase conformation between these three states. Interestingly, we also observe the s2 state in control samples - proteasome purified with 4 mM ATP - raising questions about the activation mechanism of the proteasome. Is substrate the only trigger for state switching? It is plausible that s2 is a product of proteasome switching into an activated state without substrate that is then directly deactivated again.

The role of Rpn1 in substrate recognition, proteasome activation and gate opening has not yet been addressed in detail. Rpn1 functions as an interaction hub which connects to many different proteasome subunits. Cryo-EM studies revealed that it undergoes large movements when switching from the s1 state to higher activated states. The high conformational flexibility of Rpn1 coupled with a low local resolution was prominent in the closed gate states, leading to suboptimal models and difficulties during structural analysis. A deeper structural and biological analysis could help in understanding the function of this large subunit and shed light on activation mechanisms of the whole complex. It is worth noting that the Rpn1 N-terminus is stably fixed through interactions with Rpt subunits in the open gate states, implying that Rpn1 is another key player in gate opening.

Lastly, 26S proteasome activation is regulated by several factors; this includes substrate binding, PIP binding, and even post-translational modification of proteasome subunits, such as phosphorylation. It has been reported that phosphorylation of Rpn6 can lead to a higher ATPase activation (Lokireddy et al., 2015). The structural basis of this activation mechanism is not yet clear. The methods used for this thesis could readily be adjusted and used to study the structure of activated 26S proteasomes. Considering the multiple roles of the proteasome in eukaryotes, a deeper structural analysis of the 26S proteasome is a crucial area of study to fully understand 26S proteasome regulation at multiple levels.

Overall, every additional proteasome state helps to answer fundamental questions of proteasome function and adds to the understanding of this complex degradation machine. Regulation through substrate engagement, cofactor binding and other post-translational modifications are still not well understood and more research is needed to gain greater insight into this field. The world of the 26S proteasome will certainly stay exciting.

Appendix A

Abbreviations

2D	two-dimensional
3D	three-dimensional
AAA+-ATPase	ATPases associated with diverse cellular activities
ADP	adenosine diphosphate
Ar-δ	aromatic-hydrophobic
ATP	adenosine triphosphate
ADP	adenosine diphosphate
ATPyS	adenosine 5'-(3-thiotriphosphate)
BeF_x	beryllium fluoride
Bpa	bacterial proteasome activator
BSA	bovine serum albumin
CCD	charge-coupled device
CET	cryo-electron tomography
CMOS	complementary metal oxide semiconductor
ClpX	ATP-dependent caseinolytic protease X
CP	core particle (20S)
CPh	creatine phosphate
CPK	creatine phosphate kinase
cryo-EM	cryo-electron microscopy
CTF	contrast transfer function
DDD	direct electron detection device
dH_2O	ultrapure Water
DHFR	dihydrofolate reductase
DNA	deoxyribonucleic acid
DQE	detective quantum efficiency
DTT	dithiothreitol
DUB	deubiquitinating enzyme

E1	ubiquitin-activating enzyme
E2	ubiquitin-conjugating enzyme
E3	ubiquitin ligase
EDTA	ethylenedinitrilotetraacetic acid disodium salt dehydrate
FEG	field emission gun
5-FOA	5-fluoroorotic acid
FSC	Fourier shell correlation
FU	fluorescence
GFP	green fluorescent protein
HbYX	hydrophobic-tyrosine-any amino acid tripeptide
HCl	hydrochloric acid
HEPES	N-2-Hydroxyethylpiperazine-N'-2-ethanesulfonic acid
Ins	insertion loop
IPTG	isopropyl-β-D-1-thiogalactopyranoside
JAMM	JAB1/MPN/Mov34 metalloenzyme
KCl	potassium chloride
LB	lysogeny broth
MDFF	molecular dynamics flexible fitting
$MgCl_2$	magnesium chloride
$MgSO_4$	magnesium sulfate
MOPS	3-(N-Morpholino)propanesulfonic acid
MPN	Mpr1/Pad1 N-terminal
NaCl	sodium chloride
NF-κB	nuclear factor 'kappa-light-chain-enhancer' of activated B-cells
Ni-NTA	nickel-nitrilotriacetic acid
NMR	nuclear magnetic resonance
Ntn	N-terminal nucleophilic (Ntn) hydrolases
OB	oligosaccharide-binding
OD	optical density
*o*PA	1,10-phenantrholine
PafE	proteasome accessory factor E
PA	proteasome activator
PAN	proteasome-activating nucleotidase
Phe-cluster	phenylalanine-cluster
PC	proteasome/cyclosome
PCA	principle component analysis
PCI	proteasome-COP9-initiation factor
PCR	polymerase chain reaction

PIP	proteasome interacting protein
polyUb	poly-ubiquitin
Pru	pleckstrin-like receptor for ubiquitin
pseudo-sc26S	pseudo singly capped 26S particles
PVDF	polyvinylidenfluoride
RMSD	root-mean-square deviation
RP	regulatory particle (19S)
Rpn	regulatory particle non-ATPase
Rpt	regulatory particle tripleA-ATPase
SDS	sodium dodecyl sulfate
SDS-PAGE	sodium dodecyl sulfate polyacrylamide gel electrophoresis
SNR	signal-to-noise ratio
SPA	single-particle analysis
TAE	Tris-acetate-EDTA
TEM	transmission electron microscope
UA	uranyl acetate
UBL	ubiquitin-like
UCSF	University of California at San Francisco
UIM	ubiquitin-interacting motif
UPS	ubiquitin proteasome system
VWA	von Willebrand A
YPD	yeast extract peptone dextrose

References

Albert, S., Schaffer, M., Beck, F., Mosalaganti, S., Asano, S., Thomas, H. F., Plitzko, J. M., Beck, M., Baumeister, W., and Engel, B. D. (2017). Proteasomes tether to two distinct sites at the nuclear pore complex. *Proc Natl Acad Sci U S A*, 114(52):13726–13731.

Asano, S. (2015). Electron CryoTomography Studies of Mammalian Neurons. PhD thesis, Technische Universität München.

Asano, S., Fukuda, Y., Beck, F., Aufderheide, A., Forster, F., Danev, R., and Baumeister, W. (2015). Proteasomes. A molecular census of 26S proteasomes in intact neurons. *Science*, 347(6220):439–442.

Aufderheide, A., Beck, F., Stengel, F., Hartwig, M., Schweitzer, A., Pfeifer, G., Goldberg, A. L., Sakata, E., Baumeister, W., and Förster, F. (2015). Structural characterization of the interaction of Ubp6 with the 26S proteasome. *Proceedings of the National Academy of Sciences of the United States of America*, 112(28):8626–31.

Bai, X.-c., McMullan, G., and Scheres, S. H. (2015). How cryo-EM is revolutionizing structural biology. *Trends in Biochemical Sciences*, 40(1):49–57.

Banerjee, S., Bartesaghi, A., Merk, A., Rao, P., Bulfer, S. L., Yan, Y., Green, N., Mroczkowski, B., Neitz, R. J., Wipf, P., Falconieri, V., Deshaies, R. J., Milne, J. L., Huryn, D., Arkin, M., and Subramaniam, S. (2016). 2.3 A resolution cryo-EM structure of human p97 and mechanism of allosteric inhibition. *Science*, 351(6275):871–875.

Bard, J. A. M., Goodall, E. A., Greene, E. R., Jonsson, E., Dong, K. C., and Martin, A. (2018). Structure and Function of the 26S Proteasome. *Annu Rev Biochem*, 87(1):null.

Baumeister, W. and Steven, A. C. (2000). Macromolecular electron microscopy in the era of structural genomics. *Trends in biochemical sciences*, 25(12):624–31.

Beck, F., Unverdorben, P., Bohn, S., Schweitzer, A., Pfeifer, G., Sakata, E., Nickell, S., Plitzko, J. M., Villa, E., Baumeister, W., and Förster, F. (2012). Near-atomic resolution structural model of the yeast 26S proteasome. *Proceedings of the National Academy of Sciences of the United States of America*, 109(37):14870–5.

Beckwith, R., Estrin, E., Worden, E. J., and Martin, A. (2013). Reconstitution of the 26S proteasome reveals functional asymmetries in its AAA+ unfoldase. *Nature Structural & Molecular Biology*, 20(10):1164–1172.

Bence, N. F., Sampat, R. M., and Kopito, R. R. (2001). Impairment of the ubiquitin-proteasome system by protein aggregation. *Science*, 292(5521):1552–1555.

Bohn, S., Beck, F., Sakata, E., Walzthoeni, T., Beck, M., Aebersold, R., Forster, F., Baumeister, W., and Nickell, S. (2010). Structure of the 26S proteasome from Schizosaccharomyces pombe at subnanometer resolution. *Proc Natl Acad Sci U S A*, 107(49):20992–20997.

Bolten, M., Delley, C. L., Leibundgut, M., Boehringer, D., Ban, N., and Weber-Ban, E. (2016). Structural Analysis of the Bacterial Proteasome Activator Bpa in Complex with the 20S Proteasome. *Structure*, 24(12):2138–2151.

Booth, C. and Mooney, P. (2013). Applications of electron-counting direct-detection cameras in high- resolution cryo-electron microscopy. *Microscopy and Analysis*, 27(6):13–21.

Borissenko, L. and Groll, M. (2007). 20S proteasome and its inhibitors: crystallographic knowledge for drug development. *Chem Rev*, 107(3):687–717.

Chen, S., Wu, J., Lu, Y., Ma, Y. B., Lee, B. H., Yu, Z., Ouyang, Q., Finley, D. J., Kirschner, M. W., and Mao, Y. (2016). Structural basis for dynamic regulation of the human 26S proteasome. *Proc. Natl Acad Sci U S A*, 113(46):12991–12996.

Chen, X., Lee, B. H., Finley, D., and Walters, K. J. (2010). Structure of proteasome ubiquitin receptor hRpn13 and its activation by the scaffolding protein hRpn2. *Mol Cell*, 38(3):404–415.

Chen, Y., Pfeffer, S., Hrabe, T., Schuller, J. M., and Forster, F. (2013). Fast and accurate reference-free alignment of subtomograms. *J Struct Biol*, 182(3):235–245.

Dahlmann, B., Kopp, F., Kuehn, L., Niedel, B., Pfeifer, G., Hegerl, R., and Baumeister, W. (1989). The multicatalytic proteinase (prosome) is ubiquitous from eukaryotes to archaebacteria. *FEBS Lett*, 251(1-2):125–131.

Dambacher, C. M., Worden, E. J., Herzik, M. A., Martin, A., and Lander, G. C. (2016). Atomic structure of the 26S proteasome lid reveals the mechanism of deubiquitinase inhibition. *Elife*, 5:e13027.

de Poot, S. A. H., Tian, G., and Finley, D. (2017). Meddling with Fate: The Proteasomal Deubiquitinating Enzymes. *J Mol Biol*, 429(22):3525–3545.

Delley, C. L., Laederach, J., Ziemski, M., Bolten, M., Boehringer, D., and Weber-Ban, E. (2014). Bacterial Proteasome Activator Bpa (Rv3780) Is a Novel Ring-Shaped Interactor of the Mycobacterial Proteasome. *PLoS ONE*, 9(12):e114348.

Deveraux, Q., Ustrell, V., Pickart, C., and Rechsteiner, M. (1994). A 26 S protease subunit that binds ubiquitin conjugates. *J Biol Chem*, 269(10):7059–7061.

Eisele, M. R., Reed, R. G., Rudack, T., Schweitzer, A., Beck, F., Nagy, I., Pfeifer, G., Plitzko, J. M., Baumeister, W., Tomko, R. J., and Sakata, E. (2018). Expanded Coverage of the 26S Proteasome Conformational Landscape Reveals Mechanisms of Peptidase Gating. *Cell Reports*, 24(5):1301–1315.e5.

Engelhardt, H. (2018). Electron Microscopy. In Lottspeich, F. and Engels, J., editors, *Bioanalytics*, pages 485–517. Wiley.

Finley, D. (2009). Recognition and processing of ubiquitin-protein conjugates by the proteasome. *Annu Rev Biochem*, 78:477–513.

Finley, D., Chen, X., and Walters, K. J. (2016). Gates, Channels, and Switches: Elements of the Proteasome Machine. *Trends Biochem Sci*, 41(1):77–93.

Finley, D., Ulrich, H. D., Sommer, T., and Kaiser, P. (2012). The ubiquitin-proteasome system of Saccharomyces cerevisiae. *Genetics*, 192(2):319–360.

Fishbain, S., Inobe, T., Israeli, E., Chavali, S., Yu, H., Kago, G., Babu, M. M., and Matouschek, A. (2015). Sequence composition of disordered regions fine-tunes protein half-life. *Nat Struct Mol Biol*, 22(3):214–221.

Fishbain, S., Prakash, S., Herrig, A., Elsasser, S., and Matouschek, A. (2011). Rad23 escapes degradation because it lacks a proteasome initiation region. *Nat Commun*, 2:192.

Forster, A., Masters, E. I., Whitby, F. G., Robinson, H., and Hill, C. P. (2005). The 1.9 A structure of a proteasome-11S activator complex and implications for proteasome-PAN/PA700 interactions. *Mol Cell*, 18(5):589–599.

Forster, A., Whitby, F. G., and Hill, C. P. (2003). The pore of activated 20S proteasomes has an ordered 7-fold symmetric conformation. *EMBO J*, 22(17):4356–4364.

Forster, F., Lasker, K., Beck, F., Nickell, S., Sali, A., and Baumeister, W. (2009). An atomic model AAA-ATPase/20S core particle sub-complex of the 26S proteasome. *Biochem Biophys Res Commun*, 388(2):228–233.

Forster, F., Lasker, K., Nickell, S., Sali, A., and Baumeister, W. (2010). Toward an integrated structural model of the 26S proteasome. *Mol Cell Proteomics*, 9(8):1666–1677.

Förster, F., Schuller, J. M., Unverdorben, P., and Aufderheide, A. (2014). Emerging mechanistic insights into AAA complexes regulating proteasomal degradation. *Biomolecules*, 4(3):774–94.

Förster, F., Villa, E., Thomas, D., Korinek, A., and Baumeister, W. (2012). Structure Determination of Macromolecular Complexes by Cryo-Electron Microscopy in vitro and in situ. In Dyson, H. J., editor, *Biophysical techniques for structural characterization of macromolecules (Comprehensive Biophysics, Vol. 1)*, volume 1, pages 245–276. Elsevier, Amsterdam.

Frank, J. (2006). *Three-dimensional electron microscopy of macromolecular assemblies : visualization of biological molecules in their native state.* Oxford University Press.

Frank, J. (2009). Single-particle reconstruction of biological macromolecules in electron microscopy–30 years. *Q Rev Biophys*, 42(3):139–158.

Fulda, S., Rajalingam, K., and Dikic, I. (2012). Ubiquitylation in immune disorders and cancer: from molecular mechanisms to therapeutic implications. *EMBO molecular medicine*, 4(7):545–56.

Gates, S. N., Yokom, A. L., Lin, J., Jackrel, M. E., Rizo, A. N., Kendsersky, N. M., Buell, C. E., Sweeny, E. A., Mack, K. L., Chuang, E., Torrente, M. P., Su, M., Shorter, J., and Southworth, D. R. (2017). Ratchet-like polypeptide translocation mechanism of the AAA+ disaggregase Hsp104. *Science.*

Gillette, T. G., Kumar, B., Thompson, D., Slaughter, C. A., and DeMartino, G. N. (2008). Differential roles of the COOH termini of AAA subunits of PA700 (19 S regulator) in asymmetric assembly and activation of the 26 S proteasome. *J Biol Chem*, 283(46):31813–31822.

Glickman, M. H. and Ciechanover, A. (2002). The ubiquitin-proteasome proteolytic pathway: destruction for the sake of construction. *Physiol Rev*, 82(2):373–428.

Glickman, M. H., Rubin, D. M., Coux, O., Wefes, I., Pfeifer, G., Cjeka, Z., Baumeister, W., Fried, V. A., and Finley, D. (1998a). A subcomplex of the proteasome regulatory particle required for ubiquitin-conjugate degradation and related to the COP9-signalosome and eIF3. *Cell*, 94(5):615–623.

Glickman, M. H., Rubin, D. M., Fried, V. A., and Finley, D. (1998b). The regulatory particle of the Saccharomyces cerevisiae proteasome. *Mol Cell Biol*, 18(6):3149–3162.

Glynn, S. E., Martin, A., Nager, A. R., Baker, T. A., and Sauer, R. T. (2009). Structures of asymmetric ClpX hexamers reveal nucleotide-dependent motions in a AAA+ protein-unfolding machine. *Cell*, 139(4):744–756.

Glynn, S. E., Nager, A. R., Baker, T. A., and Sauer, R. T. (2012). Dynamic and static components power unfolding in topologically closed rings of a AAA+ proteolytic machine. *Nat Struct Mol Biol*, 19(6):616–622.

Goh, B. C., Hadden, J. A., Bernardi, R. C., Singharoy, A., McGreevy, R., Rudack, T., Cassidy, C. K., and Schulten, K. (2016). Computational Methodologies for Real-Space Structural Refinement of Large Macromolecular Complexes. *Annu Rev Biophys.*, 45:253–278.

Gomez, T. A., Kolawa, N., Gee, M., Sweredoski, M. J., and Deshaies, R. J. (2011). Identification of a functional docking site in the Rpn1 LRR domain for the UBA-UBL domain protein Ddi1. *BMC Biol*, 9:33.

Groll, M., Bajorek, M., Kohler, A., Moroder, L., Rubin, D. M., Huber, R., Glickman, M. H., and Finley, D. (2000). A gated channel into the proteasome core particle. *Nat Struct Biol*, 7(11):1062–1067.

Groll, M., Ditzel, L., Lowe, J., Stock, D., Bochtler, M., Bartunik, H. D., and Huber, R. (1997). Structure of 20S proteasome from yeast at 2.4 A resolution. *Nature*, 386(6624):463–471.

Groll, M. and Huber, R. (2004). Inhibitors of the eukaryotic 20S proteasome core particle: a structural approach. *Biochimica et Biophysica Acta (BBA) - Molecular Cell Research*, 1695(1-3):33–44.

Guo, Q., Lehmer, C., Martinez-Sanchez, A., Rudack, T., Beck, F., Hartmann, H., Perez-Berlanga, M., Frottin, F., Hipp, M. S., Hartl, F. U., Edbauer, D., Baumeister, W., and Fernandez-Busnadiego, R. (2018). In Situ Structure of Neuronal C9orf72 Poly-GA Aggregates Reveals Proteasome Recruitment. *Cell*.

Haglund, K. and Dikic, I. (2005). Ubiquitylation and cell signaling. *EMBO J*, 24(19):3353–3359.

He, J., Kulkarni, K., da Fonseca, P. C., Krutauz, D., Glickman, M. H., Barford, D., and Morris, E. P. (2012). The structure of the 26S proteasome subunit Rpn2 reveals its PC repeat domain as a closed toroid of two concentric alpha-helical rings. *Structure*, 20(3):513–521.

Hershko, A. and Ciechanover, A. (1998). The ubiquitin system. *Annu Rev Biochem*, 67:425–479.

Huang, X., Luan, B., Wu, J., and Shi, Y. (2016). An atomic structure of the human 26S proteasome. *Nature Structural & Molecular Biology*, 23(9):778–785.

Humphrey, W., Dalke, A., and Schulten, K. (1996). VMD: visual molecular dynamics. *J Mol Graph.*, 14(1):27–28,33–38.

Husnjak, K., Elsasser, S., Zhang, N., Chen, X., Randles, L., Shi, Y., Hofmann, K., Walters, K. J., Finley, D., and Dikic, I. (2008). Proteasome subunit Rpn13 is a novel ubiquitin receptor. *Nature*, 453(7194):481–8.

Ikeda, F. and Dikic, I. (2008). Atypical ubiquitin chains: new molecular signals. 'Protein Modifications: Beyond the Usual Suspects' review series. *EMBO Rep*, 9(6):536–542.

Inobe, T., Fishbain, S., Prakash, S., and Matouschek, A. (2011). Defining the geometry of the two-component proteasome degron. *Nature chemical biology*, 7(3):161–167.

Iosefson, O., Nager, A. R., Baker, T. A., and Sauer, R. T. (2015). Coordinated gripping of substrate by subunits of an AAA+ proteolytic machine. *Nat Chem Biol*.

Jacobson, A. D., Zhang, N.-Y., Xu, P., Han, K.-J., Noone, S., Peng, J., and Liu, C.-W. (2009). The lysine 48 and lysine 63 ubiquitin conjugates are processed differently by the 26 s proteasome. *The Journal of biological chemistry*, 284(51):35485–94.

Janse, D. M., Crosas, B., Finley, D., and Church, G. M. (2004). Localization to the proteasome is sufficient for degradation. *J Biol Chem*, 279(20):21415–21420.

Jung, T., Catalgol, B., and Grune, T. (2009). The proteasomal system. *Mol Aspects Med*, 30(4):191–296.

Kisselev, A. F. and Goldberg, A. L. (2001). Proteasome inhibitors: from research tools to drug candidates. *Chemistry & biology*, 8(8):739–58.

Kohler, A., Cascio, P., Leggett, D. S., Woo, K. M., Goldberg, A. L., and Finley, D. (2001). The axial channel of the proteasome core particle is gated by the Rpt2 ATPase and controls both substrate entry and product release. *Mol Cell*, 7(6):1143–1152.

Komander, D. and Rape, M. (2012). The ubiquitin code. *Annu Rev Biochem*, 81:203–229.

Komander, D., Reyes-Turcu, F., Licchesi, J. D., Odenwaelder, P., Wilkinson, K. D., and Barford, D. (2009). Molecular discrimination of structurally equivalent Lys 63-linked and linear polyubiquitin chains. *EMBO Rep*, 10(5):466–473.

Kraut, D. A., Israeli, E., Schrader, E. K., Patil, A., Nakai, K., Nanavati, D., Inobe, T., and Matouschek, A. (2012). Sequence- and species-dependence of proteasomal processivity. *ACS Chem Biol*, 7(8):1444–1453.

Kravtsova-Ivantsiv, Y. and Ciechanover, A. (2012). Non-canonical ubiquitin-based signals for proteasomal degradation. *J Cell Sci*, 125(Pt 3):539–548.

Kusmierczyk, A. R., Kunjappu, M. J., Funakoshi, M., and Hochstrasser, M. (2008). A multimeric assembly factor controls the formation of alternative 20S proteasomes. *Nat Struct Mol Biol*, 15(3):237–244.

Labbadia, J. and Morimoto, R. I. (2015). The biology of proteostasis in aging and disease. *Annu Rev Biochem*, 84:435–464.

Lander, G. C., Estrin, E., Matyskiela, M. E., Bashore, C., Nogales, E., and Martin, A. (2012). Complete subunit architecture of the proteasome regulatory particle. *Nature*, 482(7384):186–191.

Lander, G. C., Martin, A., and Nogales, E. (2013). The proteasome under the microscope: the regulatory particle in focus. *Curr Opin Struct Biol*, 23(2):243–251.

Lasker, K., Forster, F., Bohn, S., Walzthoeni, T., Villa, E., Unverdorben, P., Beck, F., Aebersold, R., Sali, a., and Baumeister, W. (2012). Inaugural Article: Molecular architecture of the 26S proteasome holocomplex determined by an integrative approach. *Proceedings of the National Academy of Sciences*, 109(5):1380–1387.

Lindert, S. and McCammon, J. A. (2015). Improved cryoEM-Guided Iterative Molecular Dynamics–Rosetta Protein Structure Refinement Protocol for High Precision Protein Structure Prediction. *Journal of Chemical Theory and Computation*, 11(3):1337–1346.

Lokireddy, S., Kukushkin, N. V., and Goldberg, A. L. (2015). cAMP-induced phosphorylation of 26S proteasomes on Rpn6/PSMD11 enhances their activity and the degradation of misfolded proteins. *Proceedings of the National Academy of Sciences of the United States of America*, 112(52):E7176–85.

Lowe, J., Stock, D., Jap, B., Zwickl, P., Baumeister, W., and Huber, R. (1995). Crystal structure of the 20S proteasome from the archaeon T. acidophilum at 3.4 A resolution. *Science*, 268(5210):533–539.

Lu, Y., Lee, B. H., King, R. W., Finley, D., and Kirschner, M. W. (2015). Substrate degradation by the proteasome: a single-molecule kinetic analysis. *Science*, 348(6231):1250834.

Lučić, V., Leis, A., and Baumeister, W. (2008). Cryo-electron tomography of cells: connecting structure and function. *Histochemistry and Cell Biology*, 130(2):185–196.

Lupas, A. N. and Gruber, M. (2005). The structure of alpha-helical coiled coils. *Adv Protein Chem*, 70:37–78.

Martin, A., Baker, T. A., and Sauer, R. T. (2005). Rebuilt AAA + motors reveal operating principles for ATP-fuelled machines. *Nature*, 437(7062):1115–1120.

Martin, A., Baker, T. A., and Sauer, R. T. (2008). Diverse pore loops of the AAA+ ClpX machine mediate unassisted and adaptor-dependent recognition of ssrA-tagged substrates. *Mol Cell*, 29(4):441–450.

Mastronarde, D. N. (2005). Automated electron microscope tomography using robust prediction of specimen movements. *J Struct Biol*, 152(1):36–51.

Matyskiela, M. E., Lander, G. C., and Martin, A. (2013). Conformational switching of the 26S proteasome enables substrate degradation. *Nat Struct Mol Biol*, 20(7):781–788.

Maupin-Furlow, J. (2012). Proteasomes and protein conjugation across domains of life. *Nature Reviews Microbiology*, 10(2):100–111.

McDowell, G. S. and Philpott, A. (2013). Non-canonical ubiquitylation: mechanisms and consequences. *Int J Biochem Cell Biol*, 45(8):1833–1842.

McGrath, J. P., Jentsch, S., and Varshavsky, A. (1991). UBA 1: an essential yeast gene encoding ubiquitin-activating enzyme. *EMBO J*, 10(1):227–236.

McMullan, G., Faruqi, A. R., Clare, D., and Henderson, R. (2014). Comparison of optimal performance at 300keV of three direct electron detectors for use in low dose electron microscopy. *Ultramicroscopy*, 147:156–163.

Monroe, N., Han, H., Shen, P. S., Sundquist, W. I., and Hill, C. P. (2017). Structural basis of protein translocation by the Vps4-Vta1 AAA ATPase. *Elife*, 6.

Nagy, I., Tamura, T., Vanderleyden, J., Baumeister, W., and De Mot, R. (1998). The 20S proteasome of Streptomyces coelicolor. *J Bacteriol*, 180(20):5448–5453.

Nickell, S., Forster, F., Linaroudis, A., Net, W. D., Beck, F., Hegerl, R., Baumeister, W., and Plitzko, J. M. (2005). TOM software toolbox: acquisition and analysis for electron tomography. *J Struct Biol*, 149(3):227–234.

Nogales, E. and Scheres, S. H. (2015). Cryo-EM: A Unique Tool for the Visualization of Macromolecular Complexity. *Mol Cell*, 58(4):677–689.

Orlova, E. V. and Saibil, H. R. (2011). Structural Analysis of Macromolecular Assemblies by Electron Microscopy. *Chemical Reviews*, 111(12):7710–7748.

Park, S., Kim, W., Tian, G., Gygi, S. P., and Finley, D. (2011). Structural defects in the regulatory particle-core particle interface of the proteasome induce a novel proteasome stress response. *J Biol Chem*, 286(42):36652–36666.

Park, S., Roelofs, J., Kim, W., Robert, J., Schmidt, M., Gygi, S. P., and Finley, D. (2009). Hexameric assembly of the proteasomal ATPases is templated through their C termini. *Nature*, 459(7248):866–870.

Pathare, G. R., Nagy, I., Sledz, P., Anderson, D. J., Zhou, H. J., Pardon, E., Steyaert, J., Forster, F., Bracher, A., and Baumeister, W. (2014). Crystal structure of the proteasomal deubiquitylation module Rpn8-Rpn11. *Proc Natl Acad Sci U S A*.

Peters, J. M., Cejka, Z., Harris, J. R., Kleinschmidt, J. A., and Baumeister, W. (1993). Structural features of the 26 S proteasome complex. *J Mol Biol*, 234(4):932–937.

Pettersen, E. F., Goddard, T. D., Huang, C. C., Couch, G. S., Greenblatt, D. M., Meng, E. C., and Ferrin, T. E. (2004). UCSF Chimera–a visualization system for exploratory research and analysis. *J Comput Chem.*, 25(13):1605–1612.

Phillips, J. C., Braun, R., Wang, W., Gumbart, J., Tajkhorshid, E., Villa, E., Chipot, C., Skeel, R. D., Kale, L., and Schulten, K. (2005). Scalable molecular dynamics with NAMD. *J Comput Chem.*, 26(16):1781–1802.

Prakash, S., Inobe, T., Hatch, A. J., and Matouschek, A. (2009). Substrate selection by the proteasome during degradation of protein complexes. *Nat Chem Biol*, 5(1):29–36.

Puchades, C., Rampello, A. J., Shin, M., Giuliano, C. J., Wiseman, R. L., Glynn, S. E., and Lander, G. C. (2017). Structure of the mitochondrial inner membrane AAA+ protease YME1 gives insight into substrate processing. *Science*, 358(6363).

Rabl, J., Smith, D. M., Yu, Y., Chang, S. C., Goldberg, A. L., and Cheng, Y. (2008). Mechanism of Gate Opening in the 20S Proteasome by the Proteasomal ATPases. *Molecular Cell*, 30(3):360–368.

Reimer, L. and Kohl, H. H. (2008). *Transmission electron microscopy : physics of image formation*. Springer.

Ribeiro, J. V., Bernardi, R. C., Rudack, T., Stone, J. E., Phillips, J. C., Freddolino, P. L., and Schulten, K. (2016). QwikMD - Integrative Molecular Dynamics Toolkit for Novices and Experts. *Sci Rep.*, 6:26536.

Riedinger, C., Boehringer, J., Trempe, J. F., Lowe, E. D., Brown, N. R., Gehring, K., Noble, M. E., Gordon, C., and Endicott, J. A. (2010). Structure of Rpn10 and its interactions with polyubiquitin chains and the proteasome subunit Rpn12. *J Biol Chem*, 285(44):33992–34003.

Rohou, A. and Grigorieff, N. (2015). CTFFIND4: Fast and accurate defocus estimation from electron micrographs. *J Struct Biol*, 192(2):216–221.

Rubin, D. M., Glickman, M. H., Larsen, C. N., Dhruvakumar, S., and Finley, D. (1998). Active site mutants in the six regulatory particle ATPases reveal multiple roles for ATP in the proteasome. *EMBO J*, 17(17):4909–4919.

Ruskin, R. S., Yu, Z., and Grigorieff, N. (2013). Quantitative characterization of electron detectors for transmission electron microscopy. *J Struct Biol*, 184(3):385–393.

Sadre-Bazzaz, K., Whitby, F. G., Robinson, H., Formosa, T., and Hill, C. P. (2010). Structure of a Blm10 complex reveals common mechanisms for proteasome binding and gate opening. *Mol Cell*, 37(5):728–735.

Saeki, Y. and Tanaka, K. (2012). Assembly and function of the proteasome. *Methods Mol Biol*, 832:315–337.

Sakata, E., Bohn, S., Mihalache, O., Kiss, P., Beck, F., Nagy, I., Nickell, S., Tanaka, K., Saeki, Y., Forster, F., and Baumeister, W. (2012). Localization of the proteasomal ubiquitin receptors Rpn10 and Rpn13 by electron cryomicroscopy. *Proc Natl Acad Sci U S A*, 109(5):1479–1484.

Sakata, E., Stengel, F., Fukunaga, K., Zhou, M., Saeki, Y., Forster, F., Baumeister, W., Tanaka, K., and Robinson, C. V. (2011). The catalytic activity of Ubp6 enhances maturation of the proteasomal regulatory particle. *Mol Cell*, 42(5):637–649.

Scheres, S. H. (2012). RELION: implementation of a Bayesian approach to cryo-EM structure determination. *J Struct Biol*, 180(3):519–530.

Scheres, S. H. (2016). Processing of Structurally Heterogeneous Cryo-EM Data in RELION. *Methods Enzymol*, 579:125–157.

Schreiner, P., Chen, X., Husnjak, K., Randles, L., Zhang, N., Elsasser, S., Finley, D., Dikic, I., Walters, K. J., and Groll, M. (2008). Ubiquitin docking at the proteasome through a novel pleckstrin-homology domain interaction. *Nature*, 453(7194):548–552.

Schulman, B. a. and Harper, J. W. (2009). Ubiquitin-like protein activation by E1 enzymes: the apex for downstream signalling pathways. *Nature reviews. Molecular cell biology*, 10(5):319–31.

Schweitzer, A., Aufderheide, A., Rudack, T., Beck, F., Pfeifer, G., Plitzko, J. M., Sakata, E., Schulten, K., Forster, F., and Baumeister, W. (2016). Structure of the human 26S proteasome at a resolution of 3.9 A. *Proc Natl Acad Sci U S A*, 113(28):7816–7821.

Shi, Y., Chen, X., Elsasser, S., Stocks, B. B., Tian, G., Lee, B.-H., Shi, Y., Zhang, N., de Poot, S. A. H., Tuebing, F., Sun, S., Vannoy, J., Tarasov, S. G., Engen, J. R., Finley, D., and Walters, K. J. (2016). Rpn1 provides adjacent receptor sites for substrate binding and deubiquitination by the proteasome. *Science*, 351(6275):aad9421–aad9421.

Sledz, P., Unverdorben, P., Beck, F., Pfeifer, G., Schweitzer, A., Forster, F., and Baumeister, W. (2013). Structure of the 26S proteasome with ATP-gammaS bound provides insights into the mechanism of nucleotide-dependent substrate translocation. *Proc Natl Acad Sci U S A*, 110(18):7264–7269.

Smith, D. M., Chang, S. C., Park, S., Finley, D., Cheng, Y., and Goldberg, A. L. (2007). Docking of the proteasomal ATPases' carboxyl termini in the 20S proteasome's alpha ring opens the gate for substrate entry. *Mol Cell*, 27(5):731–744.

Smith, D. M., Fraga, H., Reis, C., Kafri, G., and Goldberg, A. L. (2011). ATP binds to proteasomal ATPases in pairs with distinct functional effects, implying an ordered reaction cycle. *Cell*, 144(4):526–538.

Spahn, C. M. and Penczek, P. A. (2009). Exploring conformational modes of macromolecular assemblies by multiparticle cryo-EM. *Curr Opin Struct Biol*, 19(5):623–631.

Stadtmueller, B. M. and Hill, C. P. (2011). Proteasome Activators. *Molecular Cell*, 41(1):8–19.

Takeuchi, J., Chen, H., and Coffino, P. (2007). Proteasome substrate degradation requires association plus extended peptide. *EMBO J*, 26(1):123–131.

Thrower, J. S., Hoffman, L., Rechsteiner, M., and Pickart, C. M. (2000). Recognition of the polyubiquitin proteolytic signal. *EMBO J*, 19(1):94–102.

Tian, G., Park, S., Lee, M. J., Huck, B., McAllister, F., Hill, C. P., Gygi, S. P., and Finley, D. (2011). An asymmetric interface between the regulatory and core particles of the proteasome. *Nat Struct Mol Biol*, 18(11):1259–1267.

Tian, L., Holmgren, R. A., and Matouschek, A. (2005). A conserved processing mechanism regulates the activity of transcription factors Cubitus interruptus and NF-kappaB. *Nat Struct Mol Biol*, 12(12):1045–1053.

Tomko Jr., R. J., Funakoshi, M., Schneider, K., Wang, J., and Hochstrasser, M. (2010). Heterohexameric ring arrangement of the eukaryotic proteasomal ATPases: implications for proteasome structure and assembly. *Mol Cell*, 38(3):393–403.

Tomko Jr., R. J. and Hochstrasser, M. (2011). Order of the proteasomal ATPases and eukaryotic proteasome assembly. *Cell Biochem Biophys*, 60(1-2):13–20.

Tomko Jr., R. J. and Hochstrasser, M. (2013). Molecular architecture and assembly of the eukaryotic proteasome. *Annu Rev Biochem*, 82:415–445.

Trabuco, L. G., Villa, E., Schreiner, E., Harrison, C. B., and Schulten, K. (2009). Molecular dynamics flexible fitting: a practical guide to combine cryo-electron microscopy and X-ray crystallography. *Methods*, 49(2):174–180.

Unverdorben, P. (2014). Pseudo-atomare Interpretation von Konformationsänderungen des 26S Proteasoms nach Klassifizierung von Kryo-Elektronenmikroskopie-Daten. PhD thesis, Technische Universität München.

Unverdorben, P., Beck, F., Sledz, P., Schweitzer, A., Pfeifer, G., Plitzko, J. M., Baumeister, W., and Forster, F. (2014). Deep classification of a large cryo-EM dataset defines the conformational landscape of the 26S proteasome. *Proc Natl Acad Sci U S A*, 111(15):5544–5549.

van Heel, M., Gowen, B., Matadeen, R., Orlova, E. V., Finn, R., Pape, T., Cohen, D., Stark, H., Schmidt, R., Schatz, M., and Patwardhan, A. (2000). Single-particle electron cryo-microscopy: towards atomic resolution. *Quarterly reviews of biophysics*, 33(4):307–69.

van Nocker, S., Sadis, S., Rubin, D. M., Glickman, M., Fu, H., Coux, O., Wefes, I., Finley, D., and Vierstra, R. D. (1996). The multiubiquitin-chain-binding protein Mcb1 is a component of the 26S proteasome in Saccharomyces cerevisiae and plays a nonessential, substrate-specific role in protein turnover. *Mol Cell Biol*, 16(11):6020–6028.

Verma, R., Aravind, L., Oania, R., McDonald, W. H., Yates 3rd, J. R., Koonin, E. V., and Deshaies, R. J. (2002). Role of Rpn11 metalloprotease in deubiquitination and degradation by the 26S proteasome. *Science*, 298(5593):611–615.

Voges, D., Zwickl, P., and Baumeister, W. (1999). The 26S proteasome: a molecular machine designed for controlled proteolysis. *Annu Rev Biochem*, 68:1015–1068.

Wehmer, M. (2017). The conformational landscape of the AAA+-ATPase of the 26S proteasome studied by cryo-electron microscopy. PhD thesis, Technische Universität München.

Wehmer, M., Rudack, T., Beck, F., Aufderheide, A., Pfeifer, G., Plitzko, J. M., Forster, F., Schulten, K., Baumeister, W., and Sakata, E. (2017). Structural insights into the functional cycle of the ATPase module of the 26S proteasome. *Proc. Natl Acad Sci U S A*, 114(6):1305–1310.

Wendler, P., Shorter, J., Snead, D., Plisson, C., Clare, D. K., Lindquist, S., and Saibil, H. R. (2009). Motor mechanism for protein threading through Hsp104. *Mol Cell*, 34(1):81–92.

Wenzel, T. and Baumeister, W. (1995). Conformational constraints in protein degradation by the 20S proteasome. *Nature structural biology*, 2(3):199–204.

Whitby, F. G., Masters, E. I., Kramer, L., Knowlton, J. R., Yao, Y., Wang, C. C., and Hill, C. P. (2000). Structural basis for the activation of 20S proteasomes by 11S regulators. *Nature*, 408(6808):115–120.

Williams, D. B. and Carter, C. B. (2009). The Transmission Electron Microscope. In *Transmission Electron Microscopy*, pages 3–22. Springer US, Boston, MA.

Wilmington, S. R. and Matouschek, A. (2016). An Inducible System for Rapid Degradation of Specific Cellular Proteins Using Proteasome Adaptors. *PLoS One*, 11(4):e0152679.

Worden, E. J., Dong, K. C., and Martin, A. (2017). An AAA Motor-Driven Mechanical Switch in Rpn11 Controls Deubiquitination at the 26S Proteasome. *Mol Cell*, 67(5):799–811.e8.

Worden, E. J., Padovani, C., and Martin, A. (2014). Structure of the Rpn11-Rpn8 dimer reveals mechanisms of substrate deubiquitination during proteasomal degradation. *Nat Struct Mol Biol*, advance on.

Yang, Z. and Klionsky, D. J. (2010). Mammalian autophagy: core molecular machinery and signaling regulation. *Curr Opin Cell Biol*, 22(2):124–131.

Yao, T. and Cohen, R. E. (2002). A cryptic protease couples deubiquitination and degradation by the proteasome. *Nature*, 419(6905):403–407.

Yu, H., Kago, G., Yellman, C. M., and Matouschek, A. (2016a). Ubiquitin-like domains can target to the proteasome but proteolysis requires a disordered region. *EMBO J*, 35(14):1522–1536.

Yu, H., Singh Gautam, A. K., Wilmington, S. R., Wylie, D., Martinez-Fonts, K., Kago, G., Warburton, M., Chavali, S., Inobe, T., Finkelstein, I. J., Babu, M. M., and Matouschek, A. (2016b). Conserved Sequence Preferences Contribute to Substrate Recognition by the Proteasome. *J Biol Chem*, 291(28):14526–14539.

Yu, Y., Smith, D. M., Kim, H. M., Rodriguez, V., Goldberg, A. L., and Cheng, Y. (2010). Interactions of PAN's C-termini with archaeal 20S proteasome and implications for the eukaryotic proteasome-ATPase interactions. *EMBO J*, 29(3):692–702.

Zhang, F., Hu, M., Tian, G., Zhang, P., Finley, D., Jeffrey, P. D., and Shi, Y. (2009). Structural insights into the regulatory particle of the proteasome from Methanocaldococcus jannaschii. *Mol Cell*, 34(4):473–484.

Zheng, S. Q., Palovcak, E., Armache, J. P., Verba, K. A., Cheng, Y., and Agard, D. A. (2017). MotionCor2: anisotropic correction of beam-induced motion for improved cryo-electron microscopy. *Nat Methods*, 14(4):331–332.

Zhu, Y., Wang, W. L., Yu, D., Ouyang, Q., Lu, Y., and Mao, Y. (2018). Structural mechanism for nucleotide-driven remodeling of the AAA-ATPase unfoldase in the activated human 26S proteasome. *Nat Commun*, 9(1):1360.

Acknowledgments

My time as PhD student shaped me personally and helped me gain valuable experiences for my future. This was only possible because of the many people supporting me in many aspects of my PhD studies and life. I want to use the next sentences to thank all of them. Without them it would clearly not have been the same experience.

Foremost I would like to thank Professor Wolfgang Baumeister for giving me the opportunity to do my PhD and to dive very deep into the structural world of cryo-EM. Over the last years he created a fantastic environment for doing cryo-EM. I definitely was very fortunate due to the scientific opportunities his department offers. I am very thankful to get to know his visions and ideas.

I also would like to thank Eri Sakata, who was my direct supervisor. I am deeply grateful for discussing weekly scientific ideas, problems, the paper, thesis drafts and many more ideas. I will always remember the weeks we worked together on the paper, shaping it to the final draft and finally successfully publishing it. Thank you so much for your supervision.

I learned many new techniques, methods and gained a lot more scientific knowledge through conversations, discussion and hands-on teaching: Jürgen Plitzko, Oana Michalache, and Günter Pfeifer showed me the world of cryo-EM. If there was any problem with the microscopes Jürgen could fix it. Thank you so much for teaching me and also thank you for your wise words regarding life and career. Oana taught me all of the basics like plunging, negative stain and the first cryo steps in the first months of my PhD. Thank you so much for your time. And last but not definitely least a big big thank you to Günter. Thank you for helping me with the Titan1, for the time spent looking at 26S proteasome and for reminding me that VfB Stuttgart lost another Bundesliga game.

I am also thankful to scientific and biochemical discussions with István Nagy, Florian Beck, our collaborator Robert J. Tomko, Rubén Fernández-Busnadiego. Till Rudack, Marc Wehmer, Parijat Majumber and Andreas Schweitzer. Especially in my first year Istvan and I had many fruitful discussions. Thank you! Florian was a wonderful mentor in all questions regarding computer analysis. Thank you so much for that. Robb was a very important part of the published article. I am thankful for everything I learned from him.

A big thank you to Birgit Book, Nathalie Leclercq and Eva Sartorius, who managed all the departments bureaucracy and who were always there if there was help needed with any

organizational question. I also want to thank Inga Wolf who organized everything around computer accounts and computer problems.

Many friends and colleagues I met over the years were a significant and important part of my time in the Baumeister department and made it such a valuable experience. I am thankful for all of the stories and laughs we had. You were the very important life balance. I am thankful for our daily lunches, playing kicker and winning ice cream, hiking trips, board game and movie nights, barbecues, playing volleyball and many more events and activities. If I forgot anyone in this list of names it does not mean I am not thankful to you: Andreas, Antje, Ben, Christos, Fabian, Hugo, Javier, Jan, Jonathan, Laura, Marc, Maria, Marion, Martin, Matthias, Parijat, Sagar, Sahradha, Saikat, Stefan, Tilak, Till, Tillman, Tim, Uli, Vicky and William.

The basis of all this was my wife, Nikki and my whole family. The PhD is a time of ups and downs. Nikki was there whenever I needed to celebrate or needed some encouraging words. I cannot express it in words how thankful I am to have you by my side.

I will always carry the experience I gained in the last years with me and I know who I have to thank for. Thank you so much to everyone.